MAGNETOHYDRODYNAMIC TURBULENCE AND COSMIC RAY TRANSPORT

Snehanshu Maiti

Universitätsdissertation
zur Erlangung des akademischen Grades

doctor rerum naturalium
(Dr. rer. nat.)

in der Wissenschaftsdisziplin
Theoretische Plasma AstroPhysik

eingereicht an der
Institute für Physik und Astronomie-Fakultät
der Universität Potsdam

Datum der Disputation: 17.04.2023

Betreuer

Prof. Dr. Huirong Yan
Institute für Physik und Astronomie, Universität Potsdam

Gutachter

Prof. Dr. Martin Pohl
Deutsches Elektronen-Synchrotron, Zeuthen

Prof. Dr. Yuri Shprits
Deutsches GeoForschungsZentrum, Potsdam

Published online on the
Publication Server of the University of Potsdam:
https://doi.org/10.25932/publishup-58903
https://nbn-resolving.org/urn:nbn:de:kobv:517-opus4-589030

Abstract

The first part of the thesis studies the properties of fast mode in magneto hydrodynamic (MHD) turbulence. 1D and 3D numerical simulations are carried out to generate decaying fast mode MHD turbulence. The injection of waves are carried out in a collinear and isotropic fashion to generate fast mode turbulence. The properties of fast mode turbulence are analyzed by studying their energy spectral density, 2D structure functions and energy decay/cascade time. The injection wave vector is varied to study the dependence of the above properties on the injection wave vectors. The 1D energy spectrum obtained for the velocity and magnetic fields has $E(k) \propto k^{-2}$. The 2D energy spectrum and 2D structure functions in parallel and perpendicular directions shows that fast mode turbulence generated is isotropic in nature. The cascade/decay rate of fast mode MHD turbulence is proportional to $k^{-0.5}$ for different kinds of wave vector injection. Simulations are also carried out in 1D and 3D to compare balanced and imbalanced turbulence. The results obtained shows that while 1D imbalanced turbulence decays faster than 1D balanced turbulence, there is no difference in the decay of 3D balanced and imbalanced turbulence for the current resolution of 512 grid points.

"The second part of the thesis studies cosmic ray (CR) transport in driven MHD turbulence and is strongly dependent on it's properties. Test particle simulations are carried out to study CR interaction with both total MHD turbulence and decomposed MHD modes. The spatial diffusion coefficients and the pitch angle scattering diffusion coefficients are calculated from the test particle trajectories in turbulence. The results confirms that the fast modes dominate the CR propagation, whereas Alfvén, slow modes are much less efficient with similar pitch angle scattering rates. The cross field transport on large and small scales are investigated next. On large/global scales, normal diffusion is observed and the diffusion coefficient is suppressed by M_A^{ζ} compared to the parallel diffusion coefficients, with ζ closer to 4 in Alfvén modes than that in total turbulence as theoretically expected. For the CR transport on scales smaller than the turbulence injection scale L, both the local and global magnetic reference frames are adopted. Super diffusion is observed on such small scales in all the cases. Particularly, CR transport in Alfvén modes show clear Richardson diffusion in the *local* reference frame. The diffusion transition smoothly from the Richardson's one with index 1.5 to normal diffusion as particle's mean free path decreases from $\lambda_{\parallel} \gg L$ to $\lambda_{\parallel} \ll L$. These results have broad applications to CRs in various astrophysical environments".

Zusammenfassung

MAGNETOHYDRODYNAMISCHE TURBULENZ UND TRANSPORT KOSMISCHER STRAHLUNG

Der erste Teil der Arbeit untersucht die Eigenschaften des schnellen Modus in magnetohydrodynamischen (MHD) Turbulenzen. Es werden numerische 1D- und 3D-Simulationen durchgeführt, um eine abklingende Fast-Mode-MHD-Turbulenz zu erzeugen. Die Injektion von Wellenvektoren wird kollinear und isotrop durchgeführt, um Fast-Mode-Turbulenzen zu erzeugen. Die Eigenschaften der Fast-Mode-Turbulenz werden durch die Untersuchung ihrer Energie-Spektraldichte, 2D-Strukturfunktionen und Energieabfall-/Kaskadenzeit analysiert. Die Injektionswellenvektoren werden in verschiedenen Simulationen für unterschiedliche Arten der Injektion variiert, um die Abhängigkeit der oben genannten Eigenschaften von den Injektionswellenvektoren zu untersuchen. Das für die Geschwindigkeits- und Magnetfelder erhaltene 1D-Energiespektrum hat $E(k) \propto k^{-2}$. Das 2D-Energiespektrum und die 2D-Strukturfunktionen in parallelen und senkrechten Richtungen zeigen, dass die erzeugte Fast-Mode-Turbulenz von Natur aus isotrop ist. Die Kaskaden-/Zerfallsrate der Fast-Mode-MHD-Turbulenz ist proportional zu $k^{-0.5}$ für verschiedene Arten der Wellenvektorinjektion. Es werden auch Simulationen in 1D und 3D durchgeführt, um ausgeglichene und unausgeglichene Turbulenzen zu vergleichen. Die Ergebnisse zeigen, dass eine unausgewogene 1D-Turbulenz schneller abklingt als eine ausgeglichene 1D-Turbulenz, während es bei der derzeitigen Auflösung von 512 Gitterpunkten keinen Unterschied im Abklingen von ausgeglichener und unausgewogener 3D-Turbulenz gibt.

Der zweite Teil der Arbeit untersucht den Transport kosmischer Strahlung (CR) in angetriebenen MHD-Turbulenzen und ist stark von deren Eigenschaften abhängig. Es werden Testpartikelsimulationen durchgeführt, um die Wechselwirkung von kosmischer Strahlung sowohl mit der gesamten MHD-Turbulenz als auch mit zerlegten MHD-Moden zu untersuchen. Aus den Flugbahnen der Testteilchen in der Turbulenz werden die räumlichen Diffusionskoeffizienten und die Diffusionskoeffizienten für die Streuung im Neigungswinkel berechnet. Die Ergebnisse bestätigen, dass die schnellen Moden die CR-Ausbreitung dominieren, während Alfvén langsame Moden bei ähnlichen Neigungswinkelstreuungsraten viel weniger effizient sind.

Der Querfeldtransport auf großen und kleinen Skalen wird als nächstes untersucht. Auf großen/globalen Skalen wird normale Diffusion beobachtet und der Diffusionskoeffizient wird durch M_A^{ζ} im Vergleich zu den parallelen Diffusionskoeffizienten unterdrückt, wobei ζ in Alfvén-Moden näher bei 4 liegt als in der Gesamtturbulenz, wie theoretisch erwartet. Für den CR-Transport auf Skalen, die kleiner sind als die Turbulenzinjektionsskala L, werden sowohl der lokale als auch der globale magnetische Bezugsrahmen verwendet. Auf solch kleinen Skalen wird in allen Fällen Superdiffusion beobachtet. Insbesondere der CR-Transport in Alfv'en-Moden zeigt eine deutliche Richardson-Diffusion im *lokalen* Bezugssystem. Die Diffusion geht fließend von der Richardson-Diffusion mit dem Index 1,5 zur normalen Diffusion über, wenn die mittlere freie Weglänge der Teilchen, $\lambda_{\parallel}$, von $\lambda_{\parallel} \gg L$ auf $\lambda_{\parallel} \ll L$ abnimmt. Diese Ergebnisse haben eine breite Anwendung auf CRs in verschiedenen astrophysikalischen Umgebungen.

Acknowledgments

I would like to acknowledge the opportunity I got to do a Phd research in the Theoretical Astrophysics group at DESY, Zeuthen and the Institute für Physics and Astronomie at Universität Potsdam which gave me a new exposure to the areas of modern physics, astrophysics and high performance computing. I would like to acknowledge the availability of computing resources at these institutes without which the research outcomes of the current thesis would have not been possible.

I deeply appreciate this research opportunity given to me by my supervisor Professor Huirong Yan in the field of plasma astrophysics and introducing me to the areas of cosmic ray research and astrophysical turbulence. I would like to thank her for guiding me throughout the Phd and helping me gain insights in these fields. Her suggestions were highly valuable for the successful research outcomes and the results obtained for this thesis.

I would like to thank my other supervisor Prof Kirit Makwana who helped me out immensely for this thesis. Dr Kirit helped me with understanding the numerical simulations and gaining greater knowledge in high performance computing. Dr Kirit also provided me with turbulent data cubes which I have used to do research in cosmic ray transport. I would like to thank him for validating my codes and the results obtained and having long discussions with me for this research.

I would also like to thank my colleague Dr Heshou Zhang for providing me turbulence data cubes in the initial stages of my research which I have used to do some of my research in cosmic ray transport and for having discussions with me on the research topics in this thesis.

I would also like to thank Dr Rolf Buehler and Prof Christian Stegmann for being part of my Phd commitee and helping me finish this thesis on time.

Thesis Declaration

I hereby declare that the thesis entitled "**MAGNETOHYDRODYNAMIC TURBULENCE AND COSMIC RAY TRANSPORT**" submitted by me, for the award of the degree of **Doctor of Philosophy**, at Institut für Physik & Astronomie, Universität Potsdam, is a record of bonafide work carried out by me under the supervision of **Prof Huirong Yan**. I further declare that the work reported in this thesis has not been submitted and will not be submitted, either in part or in full, for the award of any other degree or diploma in this institute or any other institute or university.

Snehanshu Maiti
Phd Research Scholar,
Institut für Physik & Astronomie,
Universität Potsdam

Place: Potsdam, Germany

Date: 26/09/2022

Thesis Certificate

This is to certify that the thesis entitled "**MAGNETOHYDRODYNAMIC TURBULENCE AND COSMIC RAY TRANSPORT**" submitted by **Snehanshu Maiti**, Institut für Physik & Astronomie, Universität Potsdam, for the award of the degree of **Doctor of Philosophy**, is a record of bonafide work carried out by him under my supervision. The contents of this report have not been submitted and will not be submitted either in part or in full, for the award of any other degree or diploma in this institute or any other institute or university. The thesis fulfills the requirements and regulations of the University and in my opinion meets the necessary standards for submission.

Prof Huirong Yan
Research Guide and Professor,
Institut für Physik & Astronomie,
Universität Potsdam

Place: Potsdam, Germany

Date: 26/09/2022

Contents

1 Fast mode MHD Turbulence

1.1 Introduction

"Turbulence is an ubiquitous phenomena in our lives and our natural surroundings. Most of the fluids in the universe are turbulent naturally and therefore the understanding of such natural phenomena of fluid turbulence is a very intriguing and necessary problem in the study of fluid dynamics and classical physics. Fluid turbulence is observed over a wide range of scales in the known universe. On human scales, fluid turbulence is present in the interior of biological cells and in the circulatory and respiratory systems of living creatures for example. Fluid turbulence is present in countless technological devices and household appliances of modern society. On geological scales, fluid turbulence is a part of the planetary interiors, oceans and atmospheres. On astrophysical scales they are present on stellar scales influencing star formation and other stellar activities and finally extending to galactic and even supergalactic scales. Inspite of the widespread existence of fluid turbulence, the problem of turbulence remains to this day the last unsolved problem of classical mathematical physics".

Laminar flow to turbulence

"Laminar fluids move in an very orderly fashion where fluid elements move in layers sliding past one another. In laminar flow, the fluid particles follow smooth trajectories with no mixing with each other. On the contrary fluid turbulence refers to random disordered motion of fluid elements during a high velocity flow. Turbulence is characterized by the formation of eddies of a wide range of scales which are lumps of massive rotating fluid elements formed due to mixing of fluid elements. The physics of turbulence is governed by the energy transfer across these different scales of eddy motion. Energy is cascaded from large scale eddies where energy is injected into the system, called the injection scale L, to small scale eddies where there is viscous dissipation. The smallest scale reached by the energy cascade is called Kolmogorov length η, after which dissipation starts. The length scales between the driving scales and the dissipation scales of turbulence in which viscous effects are negligible are called the inertial range of turbulence. This cascade is primarily because of the nonlinear advective term of the Navier Stokes equations

where the nonlinearity is driven by the mode-mode coupling in momentum space. Turbulence is characterised by a high Reynolds number which indicates the relative strength of advection of fluid elements over the dissipation of fluid elements in a hydrodynamic flow governed by the Navier Stokes equations and is given as,

$$Re \sim u.\nabla \mathbf{u}/(\nu \nabla^2 \mathbf{u}) \tag{1.1}$$

where $\mathbf{u}$ is the flow velocity and ν is the kinematic viscosity of the fluid. The advective term $(u.\nabla \mathbf{u})$ is a nonlinear inertial flow term and is much larger compared to the viscous damping or dissipation term $(\nu \nabla^2 \mathbf{u})$ for turbulence. If L is the driving scale of turbulence, then the Reynold's number is given as,

$$Re = L\mathbf{u}/\nu \tag{1.2}$$

The turbulent interstellar medium (ISM) is turbulent with $Re > 10^8$. The transition from laminar to turbulent flow occurs at a $Re \sim 3000$. Turbulence is characterized by chaotic changes of transport variables like pressure and flow velocity in space and time when compared to laminar flows".

Hydrodynamic turbulence

"The first major advance in the understanding of turbulence was due to Andrey Kolmogorov who in 1941 provided a hydrodynamic theory for incompressible turbulence (Kolmogorov 1991). This classic theory did not consider magnetic fields in turbulence. As mentioned earlier, when energy is injected at large scales L, large eddies are formed that transfers energy to smaller and smaller eddies. The large eddies correspond to large Re and therefore do not dissipate energy through viscosity but the energy cascade process continues until the cascade reaches eddies that are small enough to dissipate energy over eddy turnover time. The Reynolds number can also be seen as a ratio between the convective time scale and the diffusive or dissipative time scale. The hydrodynamic cascade of energy is a constant across all scales of motion,

$$v_l{}^2/\tau_{cas,l} = const \tag{1.3}$$

where v_l is the velocity at the scale l for the eddies of size l. The cascade time $\tau_{cas,l}$ at the scale l is given as,

$$\tau_{cas,l} \simeq l/v_l \tag{1.4}$$

This leads to the following expression,

$$v_l \sim l^{1/3} \tag{1.5}$$

Kolmogorov's hydrodynamic theory results in an isotropic power-law energy spectrum in wave vector space k with the following relation,

$$E(k) \propto k^{(-5/3)} \tag{1.6}$$

Magnetic turbulence and astrophysical implications

Magnetic fields and plasma turbulence are at the heart of all astrophysical fluids. Plasma turbulence have been observed in the local interstellar medium (Armstrong et al. 1995) and the Milky Way (Chepurnov, Lazarian, et al. 2010) for example. Plasma turbulence is characterised by the presence of electromagnetic fields in addition to hydrodynamic turbulence. Plasma turbulence ranges from km to kpc scales and plays an important role in various astrophysical processes. The Magnetohydrodynamic (MHD) theory is used to describe such highly conducting astrophysical turbulent fluids. The fluid approximation considers the macro length and time scales only and ignores the scales comparable to collisional length and time scales. MHD turbulence is important in explaining several astrophysical phenomena such as solar wind heating and acceleration (Bruno and Carbone 2013); regulation of star formation processes (Federrath 2018; Mac Low and Klessen 2004); propagation, scattering and acceleration of cosmic rays (Jokipii 1966; Lazarian and Yan 2014; Schlickeiser 2002; Yan and Lazarian 2004; Yan, Lazarian, and V. Petrosian 2008; H. Yan and Lazarian 2008); removal of angular momentum from accretion disks (Krasnopolsky et al. 2012); the regulation of heat and mass transfer between different ISM phases; fragmentation of molecular clouds; magnetic reconnection, etc. The properties of MHD turbulence depend on the underlying modes it is composed of. The MHD system of equations of a 3D, homogeneous, uniform, isothermal plasma with a uniform background magnetic field can be separated into the linear eigenmodes — the Alfvén mode (Alfvén 1942), the slow magnetosonic mode, and the fast magnetosonic mode (Swanson 1989)".

Magnetic turbulence and IK theory

"The first major step were taken by Iroshnikov and Kraichnan (Iroshnikov 1963; Kraichnan 1965) in making attempts to describe magnetic incompressible turbu-

lence in the early 1960s. This model is isotropic in spite of the presence of the magnetic fields and predicts $k^{-3/2}$ power-law energy spectrum for both velocity and magnetic fields. However, the assumption of isotropic energy distribution in wave-vector space was gradually been criticized by many researchers. The understanding of MHD turbulence as anisotropic was developing through the theoretical and numerical works of these researchers (Higdon 1984; William H. Matthaeus et al. 1983; Montgomery and Turner 1981; Shebalin et al. 1983).

Incompressible MHD, GS95 turbulence

The MHD theory of incompressible turbulence was brought to a new light by Goldreich and Sridhar in 1995 (P. Goldreich and Sridhar 1995) by reintroducing the concept of critical balance which is the key concept. The critical balance refers to a condition where the eddy turnover time, is equal to the period of the corresponding Alfvén wave. If $l_{\parallel}$ is the parallel eddy scale and $l_{\perp}$ denotes eddy scales measured perpendicular to the magnetic field and v_A is the Alfvén velocity then the critical balance is given as,

$$l_{\perp}/v_l = l_{\parallel}/v_A \tag{1.7}$$

For strong Alfvénic turbulence, a critical balance is reached between the linear interaction time of wave packets and their nonlinear cascade time. From Eqn 1.7 the following expression can be obtained,

$$l_{\parallel} \propto l_{\perp}^{2/3} \tag{1.8}$$

This result shows scale-dependent anisotropy and reflects the tendency of eddies to become increasingly more elongated as energy cascades to smaller scales. Therefore incompressible MHD turbulence becomes anisotropic in nature. One can imagine eddies mixing magnetic field lines perpendicular to the direction of the local magnetic field. For such eddies, the original Kolmogorov treatment is applicable, resulting in perpendicular motions scaling as,

$$v_l \propto l_{\perp}^{1/3} \tag{1.9}$$

These mixing motions induce Alfvénic perturbations that determine the parallel size of the magnetized eddy. This results in a Kolmogorov like energy spectra in terms of wave vector component $k_{\perp}$ which is perpendicular to the local direction of the magnetic field.

$$E(k_\perp) \propto k_\perp^{(-5/3)} \tag{1.10}$$

Incompressible MHD turbulence is composed of the Alfvén modes and the pseudo Alfvén modes both of which follows the same scaling. Alfvénic turbulence (turbulence consisting of mostly Alfvén modes interacting with each other) is thought to be quite important in solar turbulence as Alfvén waves have been observed in solar wind (Belcher and Davis 1971). In the limit of weak turbulence, the zero frequency modes are essential for the energy transfer, resulting in a cascade in the wave vectors perpendicular to the local mean magnetic field direction only (Shebalin et al. 1983). Numerical simulations support the GS95 model (J. Cho, Lazarian, and E. T. Vishniac 2002; Jungyeon Cho and Ethan T. Vishniac 2000; Maron and Peter Goldreich 2001).

Compressible MHD, CL02 turbulence

"But real astrophysical environments with plasma turbulence is expected to be compressible with the additional presence of slow and fast modes which are compressible in nature. Turbulence in the interstellar medium is identified by the measurement of the density fluctuations in it indicating the presence of compressible turbulence (Armstrong et al. 1995). Studies of compressible MHD turbulence were performed by Cho and Lazarian (J. Cho and Lazarian 2003; Jungyeon Cho and Lazarian 2002) which are further decomposed into MHD modes (Alfvén, fast and slow). Their results confirms that the Alfvén modes and slow modes follows, $E(k_\perp) \propto k_\perp^{(-5/3)}$ and fast modes follows, $E(k) \propto k^{(-3/2)}$. The energy spectrum and anisotropy of slow modes are quite similar to Alfvén modes. The slow modes are cascaded by the shear Alfvén modes and are expected to behave like the Alfvén modes. The mode coupling studies showed that there is not much interaction between the Alfvénic and magnetosonic waves. Unlike Alfvén mode which preferentially cascades in the field perpendicular direction, fast modes seem to show an isotropic cascade. Based on this it has been shown that fast modes play a major role in cosmic ray scattering (Yan and Lazarian 2002; Yan and Lazarian 2004; H. Yan and Lazarian 2008). Because of the importance of fast mode MHD turbulence in several astrophysical phenomenas and particularly in CR scattering, the current aim of the thesis is to study the properties of fast mode MHD turbulence further".

Strength of MHD turbulence observed in astrophysical medium

"MHD turbulence regime depends on the Mach number of turbulence . The Alfvénic Mach number, M_A is defined as the ratio between field fluctuations and the Alfvén velocity whereas the sonic Mach number, M_s is defined as the ratio between field fluctuations and the sound speed. For sub-Alfvénic turbulence, $M_A < 1$ the turbulence is in MHD regime whereas for super-Alfvénic turbulence, $M_A > 1$, the turbulence becomes hydrodynamic. Subsonic turbulence has been observed in the hot gaseous environment of a nearby elliptical galaxy (Ogorzalek et al. 2017), in the HII ionized gas in Orion nebula (Sokolov et al. 2018) and in the cold and dense gases of infrared dark clouds (IRDC) (Arthur et al. 2016)".

Fast mode MHD turbulence

"These earlier studies on generation of compressible MHD turbulence were carried out by driving the turbulence with solenoidal forcing (J. Cho and Lazarian 2003; Kowal et al. 2007; Vestuto et al. 2003; Yang et al. 2018) where the proportion of magnetosonic modes generated were small. A recent study was carried out by driving the turbulence more compressively to generate compressible MHD turbulence (Makwana and Huirong Yan 2020). The authors studied how the nature of forcing changes the mode composition of MHD turbulence. It was found out that more magnetosonic modes were present in the MHD turbulence upon driving it more compressively. These high resolution simulations showed the isotropic nature of fast modes in general throughout the inertial range suggesting no scale dependant anisotropy again. However in some cases of solenoidal driving and low M_A turbulence there was a small anisotropic cascade as inferred from the 2D energy spectrum and the 2D structure function. This was probably because the fast mode fraction generated was smaller and if the proportion of fast mode is weak then it is influenced by the other dominant mode properties. They also reported that the 1D energy spectrum of the fast modes are steeper than $k^{-3/2}$ and closer to k^{-2} when the fast mode dominates. It was also found out that fast modes do not show a M_A dependence like Alfvén modes or a dependence in terms of weak and strong turbulence. In this thesis, the goal is to generate MHD fast mode turbulence independently or in the absence of other MHD modes such that their properties can be studied irrespective of other MHD modes."

Balanced vs imbalanced fast mode MHD turbulence

"Another important aspect of fast MHD turbulence is the study of balanced and imbalanced fast modes. Imbalanced turbulence has astrophysical implications, for example in the magnetospheres of stars like our sun and compact objects like white

dwarfs and neutron stars. Turbulence tends to be imbalanced here because it is mainly generated from central stars and dominated by the outward component. It is assumed that fast mode is likely to be the culprit in the heating and acceleration of winds because it dissipates effectively even without the inward component. The advantage of the fast mode compared to Alfvénic turbulence in the stellar wind acceleration is that the latter requires the production of counterwaves via reflection or by some other mechanism. The cascading of the fast mode limits the instability even in the absence of both damping (Suzuki et al. 2007; Yan and Lazarian 2002; Yan and Lazarian 2004)".

Cascade rate of fast mode MHD turbulence

Assuming that the fast modes follow the weak acoustic cascade, the cascading time is given as (Yan and Lazarian 2004):

$$\tau_k = \frac{\omega}{k^2 v_k^2} = \frac{v_{ph}}{V^2}\left(\frac{k}{L}\right)^{-1/2} \tag{1.11}$$

where V is the turbulence velocity at the injection scale and V_{ph} is the phase speed of fast modes and is equal to the Alfvén and sound velocity for high and low β plasma, respectively (Jungyeon Cho and Lazarian 2002).

The cascading rate, ν_k normalised by the wave frequency ω is given as,

$$\frac{\nu_k}{\omega} = \frac{V^2}{{v_{ph}}^2}\left(\frac{k}{L}\right)^{-1/2} \tag{1.12}$$

Aim of current study

In this current study, numerical simulations are carried out to study the properties of fast mode MHD turbulence exclusively by generating them independently of other MHD modes. The turbulence is not continuously driven so that it decays with time. The aim is to study the cascading properties of fast mode MHD turbulence through its energy spectral density and structure functions. The 1D energy spectrum is used to study if fast mode MHD turbulence follows a spectral dependence of $k^{-3/2}$ which is that of a weak acoustic cascade. The 2D energy spectrum and structure functions are used to test the isotropic nature of fast mode MHD turbulence generated through numerical simulations. The energy decay/cascade rate of turbulence is and its dependence on the wavevectors, k is studied where the value of injected wavevectors are varied over a range in different simulations.

1.2 Numerical Simulations

The aim is to study the nature of fast mode MHD turbulence generated through numerical simulations. Only MHD fast mode turbulence is generated in the current study and it is generated independent of other MHD modes. The fast MHD turbulence generated decays with time because they are not injected by a continuous driving force. Numerical simulations are carried out to generate fast mode MHD turbulence by two different methods. One of them is by injecting the wavevectors in a collinear manner and the other is by injecting the wavevectors in an isotropic manner. The values of wavevectors are varied in different simulations for each kind of injection mechanism. Another important part of the study is to distinguish between balanced and imbalanced fast mode MHD turbulence (Suzuki et al. 2007). The fast mode turbulence simulation for such comparison is carried out in both 1D and 3D in this study. 1D simulations are carried out at various resolutions of 128, 256 and 512 for the purpose of comparison. After generating turbulent data cubes, these data cubes are studied by calculating their energy spectral density, structure functions and decay rates. These studies are essential to understand the nature of fast mode turbulent cascade in different scenarios.

"The numerical simulations of fast mode MHD turbulence have been carried out using state of the art, open source software called PLUTO (Mignone et al. 2007). The code is used to obtain numerical solutions for fluid dynamics problems and is particularly targeted towards solving problems in astrophysical fluid dynamics with high Mach number. PLUTO numerically solves mixed hyperbolic/parabolic systems of partial differential equations. It solves the conservative laws of MHD using a variety of finite difference and finite volume approaches based on Godunov type schemes. These schemes have been developed to handle sharp discontinuities and high Mach number flows. For the current purpose, the ideal MHD equations are solved for a fluid with no resistivity, viscosity or magnetic diffusivity. However, the numerical dissipation from these simulations can not be ignored. The built-in HLLD Riemann solver (Mignone 2007) is utilized in conjunction with a WENO3 reconstruction scheme (Yamaleev and Carpenter 2009). The time stepping is done by Runge-Kutta method and it's third-order method".

"For the current MHD turbulence simulations, the ideal MHD equations are solved in a box with periodic boundary conditions. A compressible, nonviscous, perfectly conducting fluid immersed in a magnetic field is considered." The ideal MHD equations include the continuity equation, the induction equation, the magnetic divergence free equation and the momentum equation as follows respectively,

$$\frac{\partial \rho}{\partial t} + \nabla \cdot (\rho \mathbf{v}) = 0 \tag{1.13}$$

$$\frac{\partial \mathbf{B}}{\partial t} - \nabla \times (\mathbf{v} \times \mathbf{B}) = 0 \tag{1.14}$$

$$\nabla \cdot \mathbf{B} = 0 \tag{1.15}$$

$$\frac{\partial \rho \mathbf{v}}{\partial t} + \nabla \cdot \left[\rho \mathbf{v}\mathbf{v} + (p + B^2/2)\bar{\bar{I}} - \frac{\mathbf{B}\mathbf{B}}{2} \right] = 0 \tag{1.16}$$

"The above equations are written in a conservative form where $\rho, \mathbf{v}, \mathbf{B}, p$ denotes the mass density, velocity, magnetic field, and thermal pressure of the fluid respectively." There is no forcing term in turbulence or in other words the source term is absent in the momentum equation. The isothermal equation of state is used, ie an isothermal plasma is studied here.

When small amplitude perturbations or waves are introduced in the MHD eqns it cause deviation from the equilibrium state. Upon adding wave vector fluctuations to the equilibrium state and only considering small first order terms (neglecting the higher order terms) linearized MHD eqns are obtained. Upon varying the perturbations like $\exp[i\,(\mathbf{k}\cdot\mathbf{r} - \omega t)]$, the MHD eqns leads to the dispersion relations the roots of which has three independent roots corresponding to the three different types of wave that can propagate through an MHD plasma.

Without loss of generality, if the equilibrium magnetic field $\mathbf{B}_0$ is directed along the z-axis and the wave-vector $\mathbf{k}$ lies in the x-z plane where θ is the angle subtended between $\mathbf{B}_0$ and $\mathbf{k}$. The MHD equations reduces to the eigenvalue equation,

$$\begin{bmatrix} \omega^2 - {v_A}^2 k^2 - {c_s}^2 {k_\perp}^2 & 0 & -{c_s}^2 k_\parallel k_\perp \\ 0 & \omega^2 - {v_A}^2 {k_\parallel}^2 & 0 \\ -{c_s}^2 k_\parallel k_\perp & 0 & \omega^2 - {c_s}^2 {k_\parallel}^2 \end{bmatrix} \begin{bmatrix} v_x \\ v_y \\ v_z \end{bmatrix} = \begin{bmatrix} 0 \\ 0 \\ 0 \end{bmatrix} \tag{1.17}$$

This yields the dispersion relation,

$$(\omega^2 - k^2\, V_A^2\, \cos^2\theta)[\omega^4 - \omega^2 k^2 (V_A^2 + V_S^2) + k^4\, V_A^2\, V_S^2\, \cos^2\theta)] = 0 \tag{1.18}$$

One of the root of the dispersion relation is associated with the middle row of Eqn 1.17 and represents the shear Alfvën wave which involves plasma motion perpendicular to the magnetic field only. The other roots leads to the magnetosonic waves namely the fast wave and the slow wave and are associated with the top and bottom rows of Eqn 1.17.

The dispersion relation for fast modes follows from the second term of Eqn1.18.

$$\omega^2 = \frac{k^2}{2}(v_A^2 + c_s^2)(1 + \sqrt{1 - \frac{4v_A^2 c_s^2 k_\parallel^2}{k^2(v_A^2 + c_s^2)^2}}) \tag{1.19}$$

For the magnetosonic modes, the relation between $v_\perp$ and $v_\parallel$ can be obtained from the bottom row of Eqn 1.17.

$$v_\parallel = \frac{v_\perp k_\perp k_\parallel c_s^2}{\omega^2 - k_\parallel^2 c_s^2} \tag{1.20}$$

The simulation setup is explained here next. The simulation box is a cube of length $BLx = BLy = BLz = 1$. For such a cube, the resolution is defined by the number of grid points considered in each direction, eg 512. The turbulence is set up such that the mean magnetic field B_0 is in the z direction, which is the global parallel direction. "The normalization is such that the Alfvén velocity v_A and the mean magnetic field B_0 are numerically the same and is 0.1". The initial velocity v_0 is setup as zero and the initial density ρ_0 is taken as unity. The sound speed c_s is 0.1, same as the Alfvén speed. If a wave propagation vector is denoted by (k_x, k_y, k_z), then $k_\parallel$ is along the z direction and $k_\perp$ is along the x and y direction. The descriptions of the density, velocity and magnetic field fluctuations are described next which are added to the mean fields. These fluctuations leads to the formation of turbulence.

The density fluctuation, $\delta\rho$ obtained from the linearized MHD continuity equation is,

$$\delta\rho = \frac{\rho_0}{\omega}(\mathbf{k} \cdot \delta\mathbf{v}) \tag{1.21}$$

Density fluctuations are then added to the initial constant density, ρ_0 as follows,

$$\rho = \rho_0 + \delta\rho \tag{1.22}$$

The velocity fluctuation, $\delta\mathbf{v}$ obtained from the linearized MHD continuity equation is,

$$\delta v_x = v_\perp \frac{k_x}{k_\perp} \tag{1.23}$$

$$\delta v_y = v_\perp \frac{k_y}{k_\perp} \tag{1.24}$$

$$\delta v_z = v_\parallel \tag{1.25}$$

Velocity fluctuations are then added to the initial mean velocity field as follows,

$$\mathbf{v} = \mathbf{v_0} + \delta\mathbf{v} \tag{1.26}$$

The magnetic fluctuation, $\delta\mathbf{b}$ is obtained by linearizing the MHD induction equations and is given as:

$$\delta b_x = -k_z \delta v_x \frac{B_0}{\omega} \tag{1.27}$$

$$\delta b_y = -k_z \delta v_y \frac{B_0}{\omega} \tag{1.28}$$

$$\delta b_z = (k_x \delta v_x + k_y \delta v_y) \frac{B_0}{\omega} \tag{1.29}$$

Fluctuations are then added to the initial mean magnetic field as follows,

$$\mathbf{B} = \mathbf{B_0} + \delta\mathbf{b} \tag{1.30}$$

With the above simulation setup, the fast mode MHD turbulence generated has the following properties.

The plasma beta which is the ratio of the plasma pressure to the magnetic pressure is defined as,

$$\beta \equiv 2\left(\frac{c_s}{v_A}\right)^2 \tag{1.31}$$

The value of β obtained from the current simulations is 2.

The Alfvénic Mach number and the sonic Mach number obtained from the current simulations is defined and calculated as:

$$M_A \equiv < \frac{\delta V}{V_A} > ; M_s \equiv < \frac{\delta V}{c_s} > \tag{1.32}$$

The symbol "< ... >" indicates the spatial average, δV is the rms value of the turbulent fluctuations. Figure 1.1 shows the evolution of Mach numbers with time from our numerical simulation".

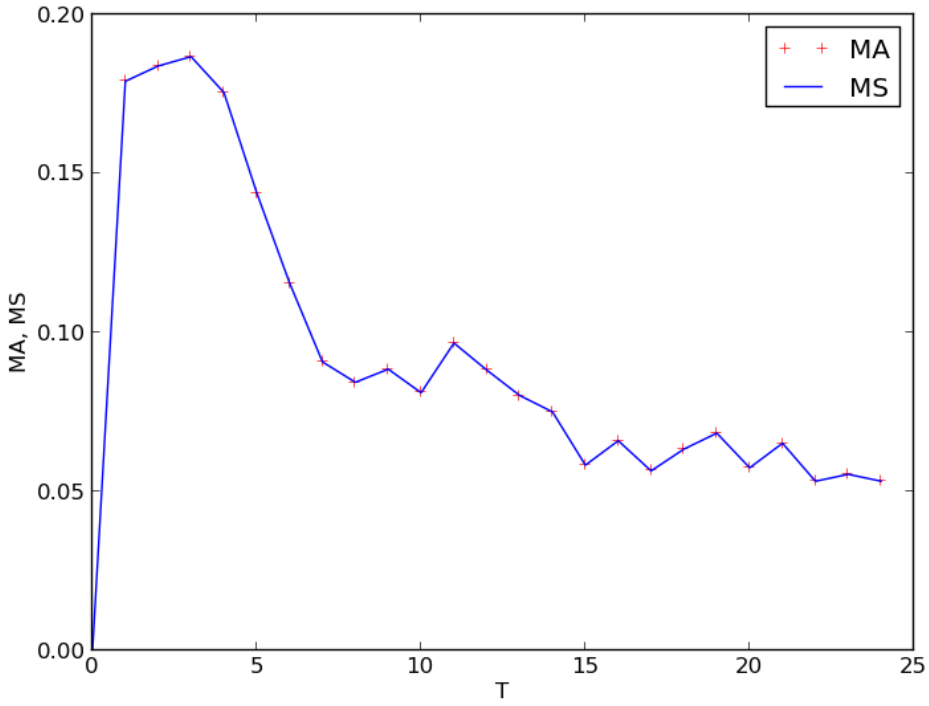

Figure 1.1: Time evolution of the Alfvénic Mach number, M_A and sonic Mach number, M_S for decaying fast mode turbulence calculated from the current numerical simulations.

In order to study the effect of collinear injection of wave vectors on the generation of fast mode turbulence the following setup mentioned in Table 1.1 is used. In each of the simulations counter interacting wave vectors in the opposing directions are injected in a collinear fashion. In different simulations (Simulation 1 to Simulation 6) the values of the injected wave vectors are increased progressively.

Wave vectors for collinear injection					
Simulation 1					
(2,2,2)	(3,3,3)	(2,2,2)	(3,3,3)	(2,2,2)	(3,3,3)
(-2,-2,-2)	(-3,-3,-3)	(-2,-2,-2)	(-3,-3,-3)	(-2,-2,-2)	(-3,-3,-3)
Simulation 2					
(3,3,3)	(4,4,4)	(3,3,3)	(4,4,4)	(3,3,3)	(4,4,4)
(-3,-3,-3)	(-4,-4,-4)	(-3,-3,-3)	(-4,-4,-4)	(-3,-3,-3)	(-4,-4,-4)
Simulation 3					
(4,4,4)	(5,5,5)	(4,4,4)	(5,5,5)	(4,4,4)	(5,5,5)
(-4,-4,-4)	(-5,-5,-5)	(-4,-4,-4)	(-5,-5,-5)	(-4,-4,-4)	(-5,-5,-5)
Simulation 4					
(5,5,5)	(6,6,6)	(5,5,5)	(6,6,6)	5,5,5)	(6,6,6))
(-5,-5,-5)	(-6,-6,-6)	(-5,-5,-5)	(-6,-6,-6)	-5,-5,-5)	(-6,-6,-6)
Simulation 5					
(6,6,6)	(7,7,7)	(6,6,6)	(7,7,7)	(6,6,6)	(7,7,7)
(-6,-6,-6)	(-7,-7,-7)	(-6,-6,-6)	(-7,-7,-7)	(-6,-6,-6)	(-7,-7,-7)
Simulation 6					
(7,7,7)	(8,8,8)	(7,7,7)	(8,8,8))	(7,7,7)	(8,8,8)
(-7,-7,-7)	(-8,-8,-8)	(-7,-7,-7)	(-8,-8,-8)	(-7,-7,-7)	(-8,-8,-8)

Table 1.1: This table lists the injected wave vectors to generate fast mode turbulence in each simulation. In each of the simulations the wavevectors in the opposing directions are injected in a collinear fashion. In different simulations the value of the injected wave vectors are increased progressively.

In order to study the effect of isotropic injection of wave vectors on the generation of fast mode turbulence the following setup mentioned in Table 1.2 is used. In each of the simulations the directions of wave vectors are changed in all possible ways to isotropize the injection. In different simulations (Simulation 1 to Simulation 6) the value of the injected wave vectors are increased progressively.

Wave vectors for isotropic injection							
Simulation 1							
(2,2,2)	(-2,2,2)	(2,-2,2)	(2,2,-2)	(-2,-2,2)	(-2,2,-2)	(2,-2,-2)	(-2,-2,-2)
(3,3,3)	(-3,3,3)	(3,-3,3)	(3,3,-3)	(-3,-3,3)	(-3,3,-3)	(3,-3,-3)	(-3,-3,-3)
Simulation 2							
(3,3,3)	(-3,3,3)	(3,-3,3)	(3,3,-3)	(-3,-3,3)	(-3,3,-3)	(3,-3,-3)	(-3,-3,-3)
(4,4,4)	(-4,4,4)	(4,-4,4)	(4,4,-4)	(-4,-4,4)	(-4,4,-4)	(4,-4,-4)	(-4,-4,-4)
Simulation 3							
(4,4,4)	(-4,4,4)	(4,-4,4)	(4,4,-4)	(-4,-4,4)	(-4,4,-4)	(4,-4,-4)	(-4,-4,-4)
(5,5,5)	(-5,5,5)	(5,-5,5)	(5,5,-5)	(-5,-5,5)	(-5,5,-5)	(5,-5,-5)	(-5,-5,-5)
Simulation 4							
(5,5,5)	(-5,5,5)	(5,-5,5)	(5,5,-5)	(-5,-5,5)	(-5,5,-5)	(5,-5,-5)	(-5,-5,-5)
(6,6,6)	(-6,6,6)	(6,-6,6)	(6,6,-6)	(-6,-6,6)	(-6,6,-6)	(6,-6,-6)	(-6,-6,-6)
Simulation 5							
(6,6,6)	(-6,6,6)	(6,-6,6)	(6,6,-6)	(-6,-6,6)	(-6,6,-6)	(6,-6,-6)	(-6,-6,-6)
(7,7,7)	(-7,7,7)	(7,-7,7)	(7,7,-7)	(-7,-7,7)	(-7,7,-7)	(7,-7,-7)	(-7,-7,-7)
Simulation 6							
(7,7,7)	(-7,7,7)	(7,-7,7)	(7,7,-7)	(-7,-7,7)	(-7,7,-7)	(7,-7,-7)	(-7,-7,-7)
(8,8,8)	(-8,8,8)	(8,-8,8)	(8,8,-8)	(-8,-8,8)	(-8,8,-8)	(8,-8,-8)	(-8,-8,-8)

Table 1.2: Same as Table1.1. In each of the simulations the directions of wave vectors are changed in all possible ways to isotropize the injection.

For balanced turbulence, the injected wave vectors are in the opposite direction and are counter interacting whereas for the imbalanced case all the injected wavevectors are in the same direction. For balanced turbulence the energy is equally distributed among the counter interacting waves whereas for the imbalanced case the wavepackets travelling in one direction has more power than wave packets travelling in other direction. For this study both 1D and 3D simulations are performed to distinguish the nature of turbulence generated in these situations.

In order to distinguish between the nature of balanced and imbalanced turbulence the following setup is used for a 1D turbulence simulation as presented in Table 1.3.

Wave vectors for collinear injection in 1D					
Balanced					
(6,0,0)	(7,0,0)	(6,0,0)	(7,0,0)	(6,0,0)	(7,0,0)
(-6,0,0)	(-7,0,0)	(-6,0,0)	(-7,0,0))	(-6,0,0)	(-7,0,0)
Imbalanced					
(6,0,0)	(7,0,0)	(6,0,0)	(7,0,0)	(6,0,0)	(7,0,0)
(6,0,0)	(7,0,0)	(6,0,0)	(7,0,0))	(6,0,0)	(7,0,0)

Table 1.3: This table lists the injected wave vectors to generate fast mode turbulence for the balanced and imbalanced case in 1D. The wave vectors are injected in a collinear fashion such that for the balanced case the wave vectors are in opposing direction and for the imbalanced case they are in the same direction.

In order to distinguish between the nature of behaviour of balanced and imbalanced turbulence the following setup is used for a 3D turbulence simulation as presented in Table 1.4.

Wave vectors for collinear injection in 3D					
Balanced					
(6,6,6)	(7,7,7)	(6,6,6)	(7,7,7)	(6,6,6)	(7,7,7)
(-6,-6,-6)	(-7,-7,-7)	(-6,-6,-6)	(-7,-7,-7))	(-6,-6,-6)	(-7,-7,-7)
Imbalanced					
(6,6,6)	(7,7,7)	(6,6,6)	(7,7,7)	(6,6,6)	(7,7,7)
(6,6,6)	(7,7,7)	(6,6,6)	(7,7,7))	(6,6,6)	(7,7,7)

Table 1.4: This table lists the injected wave vectors to generate fast mode turbulence for the balanced and imbalanced case in 3D. The wave vectors are injected in a collinear fashion such that for the balanced case the wave vectors are in opposing direction and for the imbalanced case they are in the same direction.

To analyze the MHD turbulent data cubes generated, the time evolution of the magnetic and velocity fields are analysed from different simulations. This allows one to study the decay rates and the cascade rates of turbulence. Also the turbulent fields are studied in the wave number space where Fourier transforms of the data cubes at any time instant are carried out. The 1D and 2D energy spectrum calculation for magnetic and velocity fields are carried out to look at the energy spectral density and anisotropy of the energy cascade. The structure functions of the turbulence is also calculated and studied to look at the isotropy/anisotropy of the energy cascade.

The steps for calculation of the 1D and 2D energy spectrum with respect to the wave number of turbulence is discussed here. After the 3D MHD data cubes are obtained, the magnetic field fluctuations (b_x, b_y, b_z) and the velocity field fluctuations (v_x, v_y, v_z) are calculated from the data cubes by subtracting the mean values of the fields from the original values of the fields in the data cubes. Next a discrete Fourier transform of the fluctuations in the data cubes is carried out using the Fast Fourier transform (FFT) to obtain (b_{xk}, b_{yk}, b_{zk}) and (v_{xk}, v_{yk}, v_{zk}) respectively. Next the energy in the Fourier space in the data cube is calculated by multiplying the Fourier transformed field from the data cube with the conjugate of itself. The calculation for energy $(Eb_{xk}, Eb_{yk}, Eb_{zk})$, $(Ev_{xk}, Ev_{yk}, Ev_{zk})$ is shown in Eqn 1.33 and 1.34 for the magnetic and velocity fields respectively.

$$\begin{aligned} Eb_{xk} &= real(b_{xk} * b^*_{xk}) \\ Eb_{yk} &= real(b_{yk} * b^*_{yk}) \\ Eb_{zk} &= real(b_{zk} * b^*_{zk}) \end{aligned} \tag{1.33}$$

$$\begin{aligned} Ev_{xk} &= real(v_{xk} * v^*_{xk}) \\ Ev_{yk} &= real(v_{yk} * v^*_{yk}) \\ Ev_{zk} &= real(v_{zk} * v^*_{zk}) \end{aligned} \tag{1.34}$$

The Nyquist component is an unphysical quantity arising after performing FFT on the data cubes and is removed. The vector components $Eb_{xk}, Eb_{yk}, Eb_{zk}$ are summed up to have Eb_k for the magnetic fields and the vector components $Ev_{xk}, Ev_{yk}, Ev_{zk}$ are summed up to have Ev_k for the velocity fields. The corresponding k_x, k_y, k_z is also defined such that $k_x = k_y = -(L/2) * 2\pi$ to $(L/2) * 2\pi$ and $k_z = 0$ to $(L/2) * 2\pi$ has a mapping with Eb_k and Ev_k and L is the number of grid points in the box.

Now the calculation of 1D spectrum $E_{mag}(k)$ and $E_{kin}(k)$is described here. Lets consider a list of k values are taken from 0 to $(L/2)$ * (2π) . For each k, the θ is

varied from 0 to 2π and for each θ, ϕ is varied from 0 to π which are angles in k space and the following relationship holds.

$$k_x = ksin(\phi)cos(\theta); \tag{1.35}$$

$$k_y = ksin(\phi)sin(\theta); \tag{1.36}$$

$$k_z = kcos(\phi) \tag{1.37}$$

For each θ and ϕ the corresponding (k_x, k_y, k_z) is obtained from the above equations and the energy $Eb_k(k_x, k_y, k_z)$ and $Ev_k(k_x, k_y, k_z)$ is obtained by interpolation. Then for each k the contributions of energy from all (k_x, k_y, k_z) are added as θ and ϕ are varied and the energy is averaged to obtain (Ebk_{avg}, Evk_{avg}). This value is multiplied by the shell area as follows to get 1D energy spectrum with respect to the wavenumber.

$$E_{mag}(k) = Ebk_{avg} * 4.0\pi * k * k \tag{1.38}$$

$$E_{kin}(k) = Evk_{avg} * 4.0\pi * k * k \tag{1.39}$$

Therefore, the 1D energy spectrum is calculated as,

$$E(k) = \int \int E(k, \theta, \phi)k^2 sin\theta d\theta d\phi \tag{1.40}$$

Now the calculation of the 2D spectrum $E_{mag}(k_{\|}, k_{\perp})$ and $E_{kin}(k_{\|}, k_{\perp})$ is described here. Lets consider a list of $k_{\|}$ taken from (0 to $(L/4)$) * (2π). For each $k_{\|}$, the $k_{\perp}$ is varied from (0 to $(L/4)$) * (2π). For each $k_{\perp}$, the θ is varied from 0 to 2π and the following relation holds.

$$k_x = k_{\perp}cos(\theta); \tag{1.41}$$

$$k_y = k_{\perp}sin(\theta); \tag{1.42}$$

$$k_z = k_{\|} \tag{1.43}$$

For each θ the corresponding (k_x, k_y, k_z) is obtained from the above equations and the energy $Eb_k(k_x, k_y, k_z)$ and $Ev_k(k_x, k_y, k_z)$ is obtained by interpolation. Then for each $k_{\perp}$, the average of Eb_k and Ev_k is obtained by adding Eb_k and Ev_k for all

possible values of θ ie integrating over θ to obtain Ebk_{avg} and Evk_{avg}. For any time instant, the energy spectral density $E_{mag}(k_{\|}, k_{\perp})$ and $E_{kin}(k_{\|}, k_{\perp})$ are obtained as follows,

$$E_{mag}(k_{\|}, k_{\perp}) = Ebk_{avg} * 2.0\pi * k_{\perp} \tag{1.44}$$

$$E_{kin}(k_{\|}, k_{\perp}) = Evk_{avg} * 2.0\pi * k_{\perp} \tag{1.45}$$

Therefore, the 2D energy spectrum is calculated as,

$$E(k_{\|}, k_{\perp}) = \int k_{\perp} E(k_{\perp}, \theta, k_z) d\theta \tag{1.46}$$

where $k_{\|} = k_z$, $k_{\perp} = \sqrt{(k_x^2 + k_y^2)}$ and θ is the angle between $k_{\perp}$ and x axis.

"The isotropy of the fast modes could be studied by using the structure functions. The anisotropic structure function is defined as,

$$SF_2(l_{\|}, l_{\perp}) =< |\mathbf{b}(\mathbf{r} - (l_{\|}/2)\hat{\mathbf{b}} - (l_{\perp}/2)\hat{\mathbf{b}_{\perp}}) - b(\mathbf{r} + (l_{\|}/2)\hat{\mathbf{b}} + (l_{\perp}/2)\hat{\mathbf{b}_{\perp}})|^2 >_{\mathbf{r}} \tag{1.47}$$

This function involves an ensemble average over a number of pairs of points, which are separated by distance $l_{\|}$ in the magnetic field parallel direction $\hat{\mathbf{b}}$ and distance $l_{\perp}$ in the field-perpendicular direction $\hat{\mathbf{b}_{\perp}}$. The magnetic field direction $\hat{\mathbf{b}}$ is the local mean magnetic field. To obtain the local mean magnetic field, for each parallel and perpendicular distance pair $(l_{\|}, l_{\perp})$, a distance $l = \sqrt{({l_{\|}}^2 + {l_{\perp}}^2)}$ is first calculated. Then, a random point is selected in the data cube, and a sphere is taken around this point with a diameter l. The local mean magnetic field direction is calculated by taking an average of a few (greater than 5) random points located in this sphere. We have verified that the results do not change when taking more points, which gives us the local mean field direction $\hat{\mathbf{b}}$, and a random unit vector perpendicular to $\hat{\mathbf{b}}$ is also constructed, $\hat{\mathbf{b}_{\perp}}$. Now we select two points on this sphere that are separated by $l_{\|}\hat{\mathbf{b}}+l_{\perp}\hat{\mathbf{b}_{\perp}}$. An ensemble average over thousands of such pairs gives us $SF_2(l_{\|}, l_{\perp})$".

1.3 Collinear Injection

Collinear injection of wave vectors has been described in the numerical simulations section where wave vectors in the opposing direction are injected in a collinear fashion. The 1D energy spectra of the fast mode MHD turbulence for such kind of injection is presented in Figure 1.2. The figure shows the kinetic and magnetic energy spectra for different cases where the values of the injection wavevectors are varied.

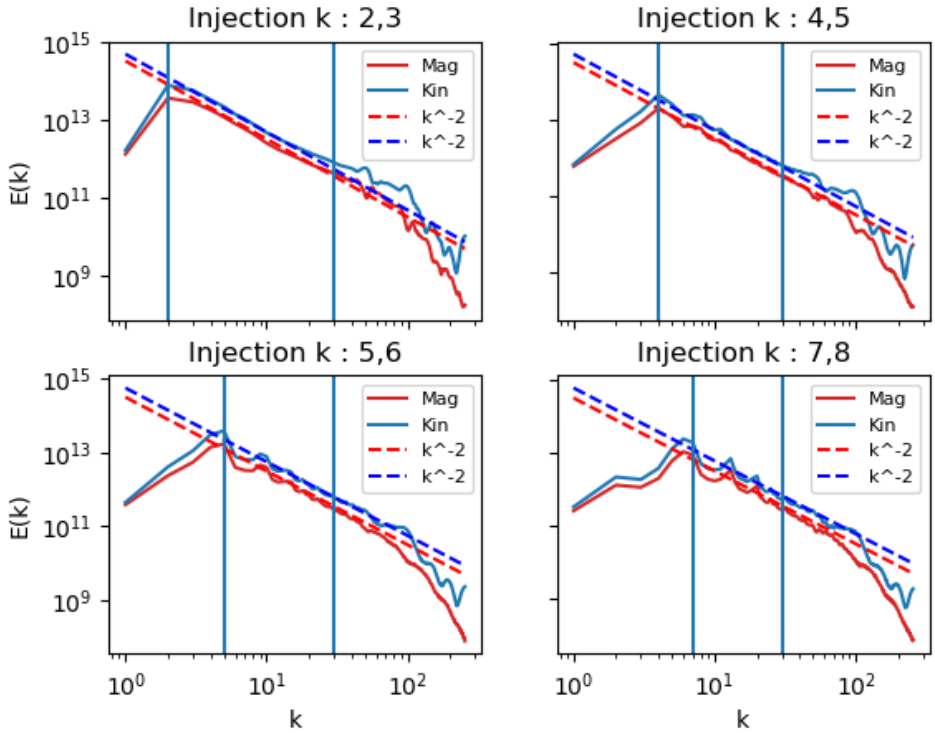

Figure 1.2: Energy spectrum of MHD fast mode turbulence for collinear injection. The red bold lines denotes the spectrum for magnetic energy and the blue bold lines denotes the spectrum for kinetic energy. The dashed lines are the reference slopes for comparison with numerical values and has a value of -2. The value of the initial wavevectors are changed in different turbulent simulations and the corresponding 1D energy spectral density are presented here. The inertial range of turbulence is denoted by blue vertical lines. The title of the figures represents the injected values of wavevectors in each simulation.

For all the numerical simulations with collinear injection, it is seen that the spectral index of the velocity and magnetic field, has a value of -2.

The 2D energy spectrum for magnetic and velocity fields from the simulations of decaying fast mode MHD turbulence when wavevectors are injected in a collinear fashion are presented in Figure 1.3. The distribution of energy in both the parallel and perpendicular direction could be observed in this figure.

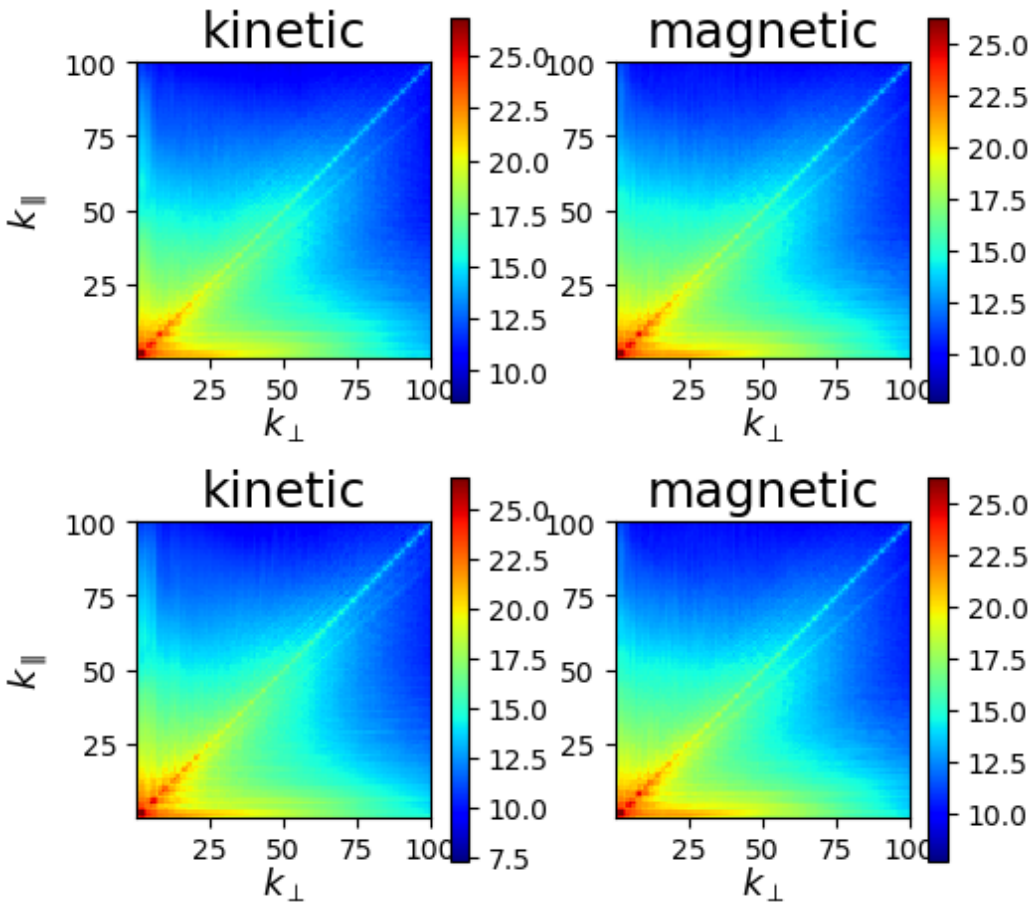

Figure 1.3: The $k_{||} - k_{\perp}$ wave-number spectrum for the velocity and the magnetic field for fast mode MHD turbulence when wave vectors are collinearly injected. Results of two different cases from Table 1.1 are presented here for Simulations 5 and 6. From the figure, it is seen that energy cascade is mainly along the direction of injection, with little diffusion in the transverse direction.

For all the numerical simulations with collinear injection of wave vectors as presented in Figure 1.3, it is seen that energy cascade is mainly along the direction of injection, with little diffusion in the transverse direction. This is observed for various simulations where the injection wave vector values are varied. Figure 1.3 presents energy spectrum from Simulation 5 and Simulation 6 in Table 1.1.

The kinetic energy decay of fast mode MHD turbulence in the case of collinear injection is presented in Figure 1.4. The decay plots are obtained from Simulations 1 to Simulation 6 in Table 1.1.

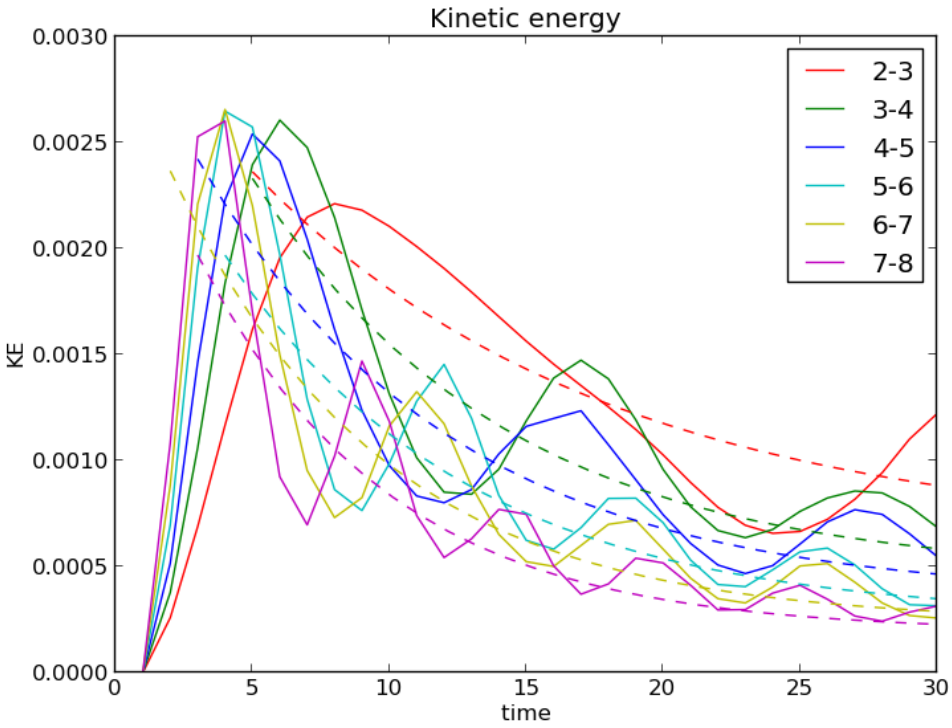

Figure 1.4: Kinetic energy decay of fast mode turbulence when injected collinearly and its dependence on the value of the injected wavevector (see Simulations 1-6 in Table 1.1). The bold lines represents the numerical values of different decay plots and the broken lines represents the fitted curves which are used to find the decay/cascade rates further.

It is seen from Figure 1.4 that the kinetic energy of fast mode turbulence when injected collinearly decays faster for higher injected wavevector. The energy cascade/decay rate is calculated by fitting an exponential decay function in the corre-

sponding decay plots as shown by dotted lines in Fig 1.4.

The dependence of kinetic energy decay/cascade rate of fast mode turbulence on different injection wavevectors is presented in Figure 1.5 for collinear injection of wave vectors.

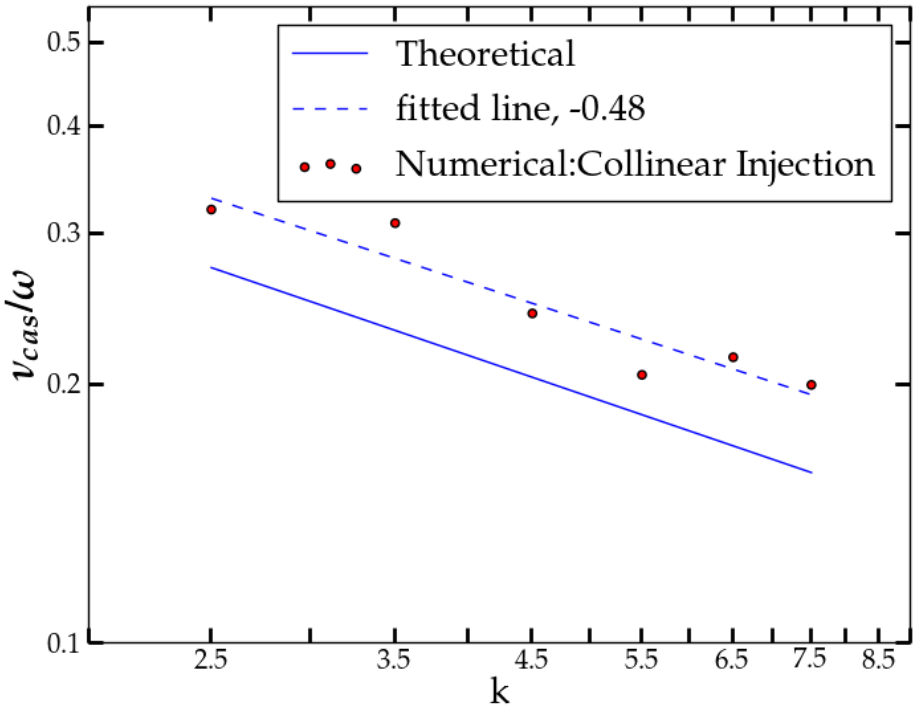

Figure 1.5: Cascading rate of fast mode turbulence and its dependance on the wavevector, k. The waves are injected collinearly initially. The red dots represents the numerical values, the blue dashed line represents the fitted line through the numerical values and the resultant slope through the fitted values is closely proportional to $k^{-0.5}$ as theoretically predicted. The blue bold line represents the reference slope of -0.5 which is theoretically predicted and compared with the numerical values. This result is compared later with the case where the wavevectors are injected isotropically in Figure 1.10.

It is seen from Figure 1.5 that the kinetic energy decay rate of fast mode turbulence when injected collinearly is proportional to $k^{-0.5}$ as theoretically predicted in Eqn 1.12.

1.4 Isotropic Injection

Isotropic injection of wave vectors has been described in the numerical simulations section. Different directions of the injected wavevectors are considered to isotropize the injection as much as possible. The 1D energy spectra of the fast mode MHD turbulence for such kind of injection is presented in Figure 1.6. The figure shows the kinetic and magnetic energy spectra for different cases where the values of the injection wavevectors are varied.

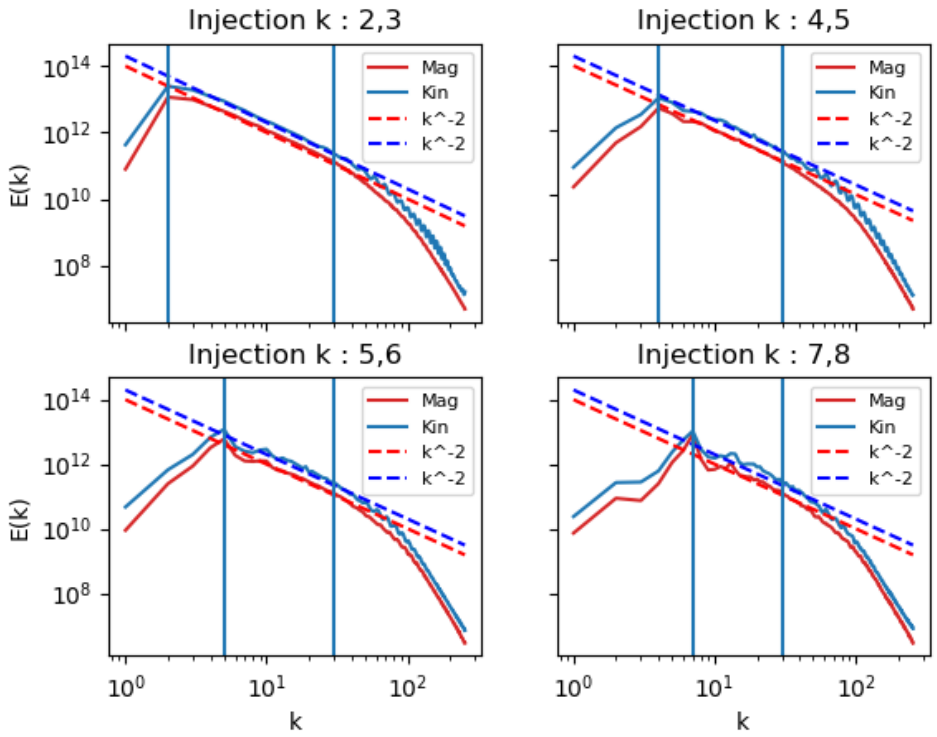

Figure 1.6: Energy spectrum of MHD fast mode turbulence for isotropic injection. The bold red line denotes the spectrum for magnetic energy and the bold blue line denotes the spectrum for kinetic energy. The dashed lines are the reference slopes for comparison with numerical values and has a value of -2. The value of the initial wavevectors are changed in different simulations and are presented here. The spectral index observed in this figure has a value of -2 for all simulations and both kinetic and magnetic fields. The inertial range is denoted by blue vertical lines. The title of the figures represents the injected values of wavevectors in each simulation.

For all the numerical simulations with isotropic injection, it is seen that the spectral index of the velocity and magnetic field, has a value of -2.

The 2D energy spectrum for magnetic and velocity fields from the simulations of decaying fast mode MHD turbulence when wavevectors are injected in a isotropic fashion are presented in Figure 1.7. The distribution of energy in both the parallel and perpendicular direction could be observed in this figure.

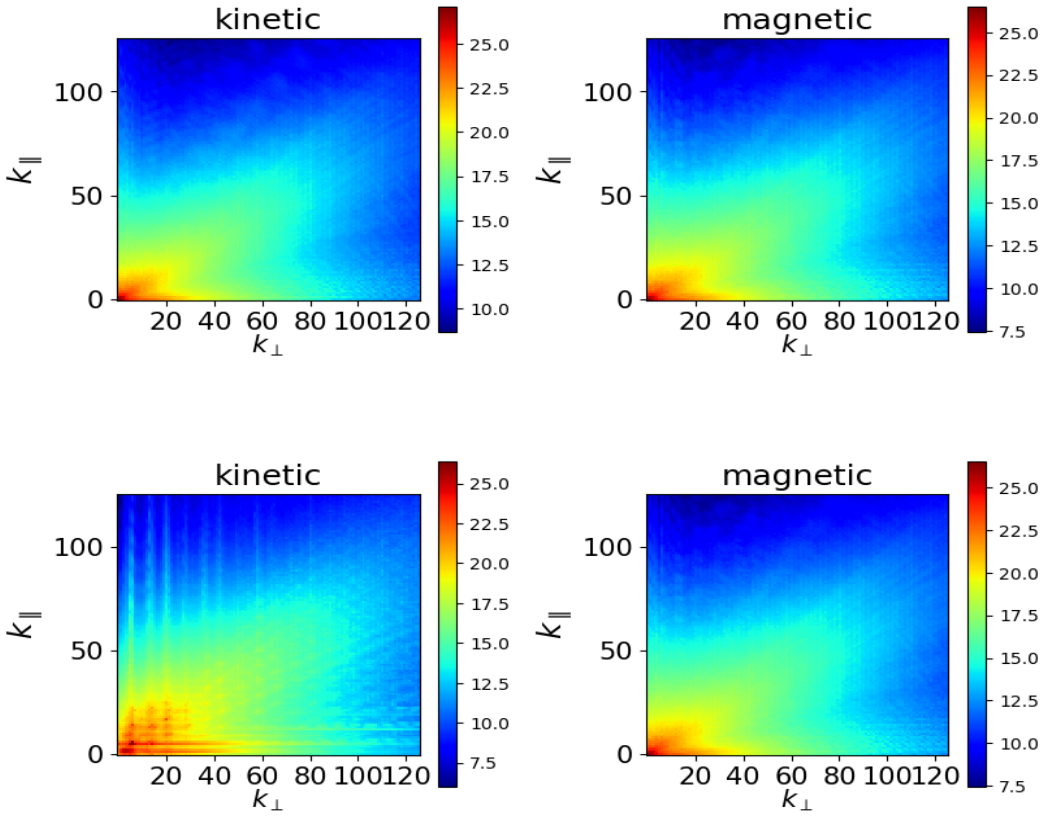

Figure 1.7: The $k_{||} - k_{\perp}$ wave-number spectrum for the velocity and the magnetic field for fast mode MHD turbulence when wave vectors are isotropically injected. Results of two different cases from Table 1.2 are presented here from Simulation 1 and 6. The figure shows that energy is equally distributed along the parallel and perpendicular direction.

For all numerical simulations with isotropic injection of wave vectors as presented in Figure 1.7, it is seen that energy is equally distributed along the parallel and perpendicular direction for both magnetic and velocity field where the injection wave vector values are varied in Simulation 1 to 6 in Table 1.2. This shows that fast

modes generated by this method is isotropic in nature.

The 2D structure function for magnetic and velocity fields from the above simulations of decaying fast mode MHD turbulence when wavevectors are injected in a isotropic fashion are presented in Figure 1.8.

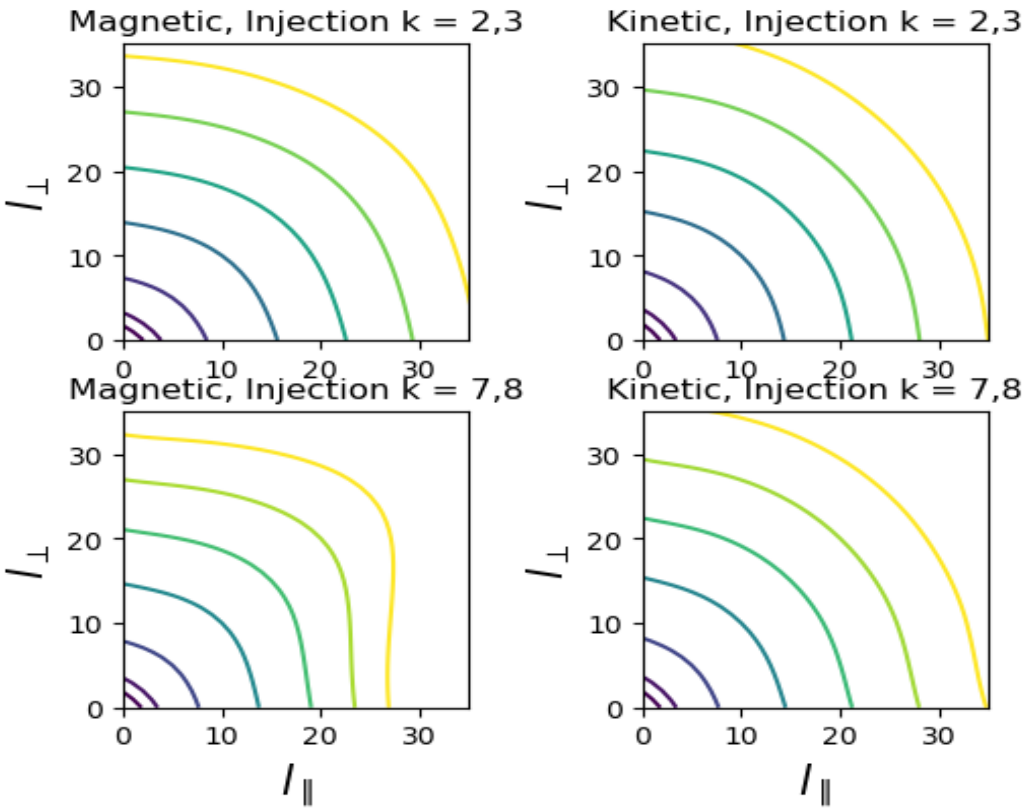

Figure 1.8: The 2D structure functions for the velocity field and the magnetic field for decaying fast mode MHD turbulence when wave vectors are isotropically injected. Results of two different cases from Table 1.2 are presented here when the initial wave vectors has values 2,3 (Simulation 1) and 7,8 (Simulation 6). The figure shows extremely isotropic contours in the parallel and perpendicular directions and therefore fast modes are isotropic in nature when wave vectors are injected isotropically.

From all the numerical simulations with isotropic injection of wave vectors and as presented in Figure 1.8, it is seen that the contour lines for both the magnetic and the kinetic fields extend equally along the parallel and perpendicular directions throughout the inertial range. This is observed for various simulations where

the injection wave vector values are varied from Simulation 1 to Simulation 6 in Table 1.2. This shows the isotropic nature of fast mode MHD turbulence generated when isotropically injected.

The kinetic energy decay of fast mode turbulence for isotropic injection is presented in Figure 1.9 for different injection wavevectors (see Simulations 1-6 in Table 1.2).

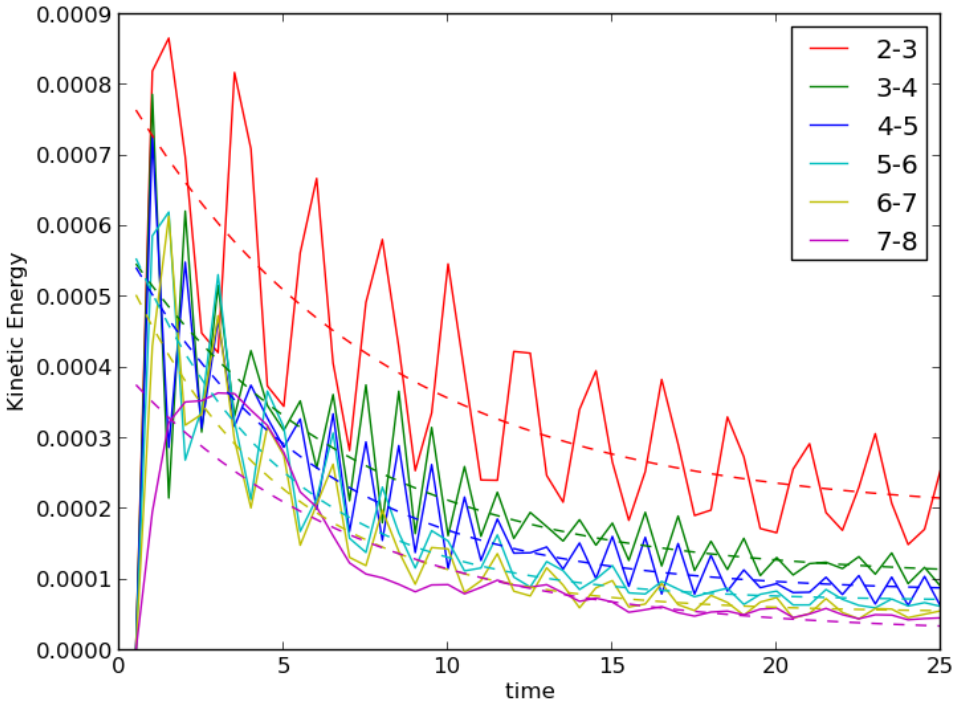

Figure 1.9: Kinetic energy decay of fast mode MHD turbulence when injected isotropically. Different coloured line is for different turbulence when the injected wave vectors are varied (see Simulations 1-6 in Table 1.2). The bold lines represents the numerical values of different decay plots and the broken lines represents the fitted curves which are used to find the decay/cascade rates further.

It is seen from Figure 1.9 that the kinetic energy of fast mode turbulence when injected isotropically decays faster for higher values of injected wavevector.

The dependence of kinetic energy decay/cascade rate of fast mode turbulence on different injection wavevectors is presented in Figure 1.10 for isotropic injection of

wave vectors. The energy cacade/decay rate is calculated by fitting an exponential decay function in the corresponding decay plots as shown by dashed lines in Fig 1.9.

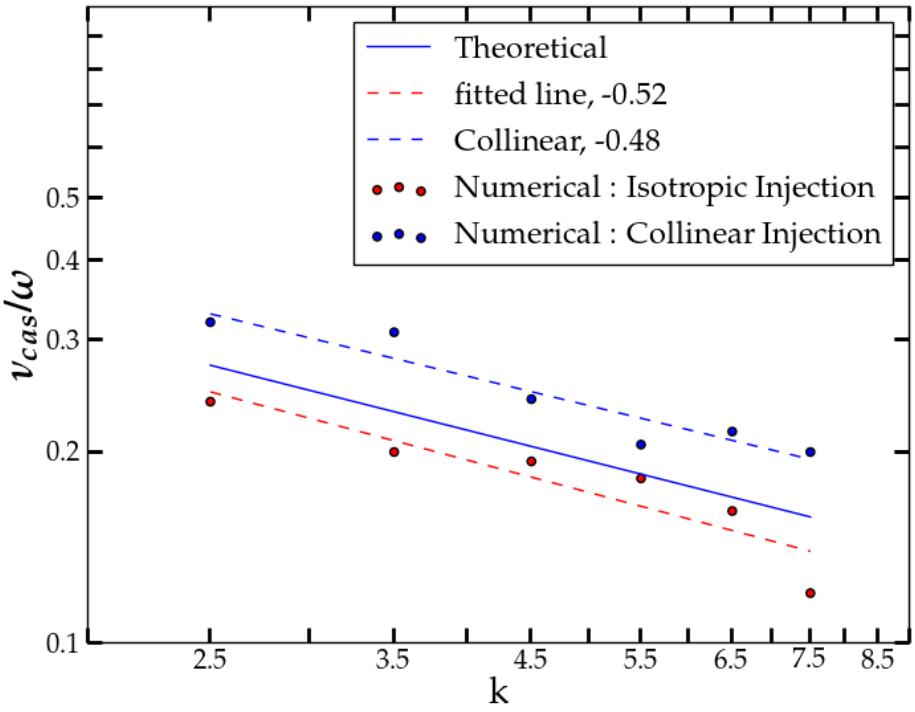

Figure 1.10: Cascading rate of fast mode turbulence and its dependence on the wavevector. For the isotropic injection case, the red dots represents the numerical values and the red dashed line represents the fitted line through the numerical values. For the collinear injection case, the blue dots represents the numerical values and the blue dotted line represents the fitted line through the numerical values. The blue bold line represents the reference slope of -0.5 which is theoretically predicted and compared with the numerical values. In both kind of injections, the cascade rate is found to be closely proportional to $k^{-}0.5$ as theoretically predicted in Eqn. 1.12.

It is seen from Figure 1.10 that the kinetic energy decay rate of fast mode turbulence when injected isotropically is proportional to $k^{-0.5}$ as theoretically predicted in Eqn 1.12. This is valid for both the different cases of injection as found in Fig 1.10.

1.5 Balanced vs Imbalanced Turbulence

In this section the comparison of cascade of fast mode MHD turbulence is carried out between balanced and imbalanced MHD turbulence for a particular case where the injection is collinear. While for the balanced turbulence, the injected wavevectors propagating in one direction has the same power as that injected in the other direction, for imbalanced turbulence the wavevectors injected in one direction has more power than that injected from the other direction. The results of the study are presented for both 1D and 3D turbulence.

Figure 1.11 presents the comparison of energy decay for a 1D simulation between balanced and imbalanced fast mode MHD turbulence.

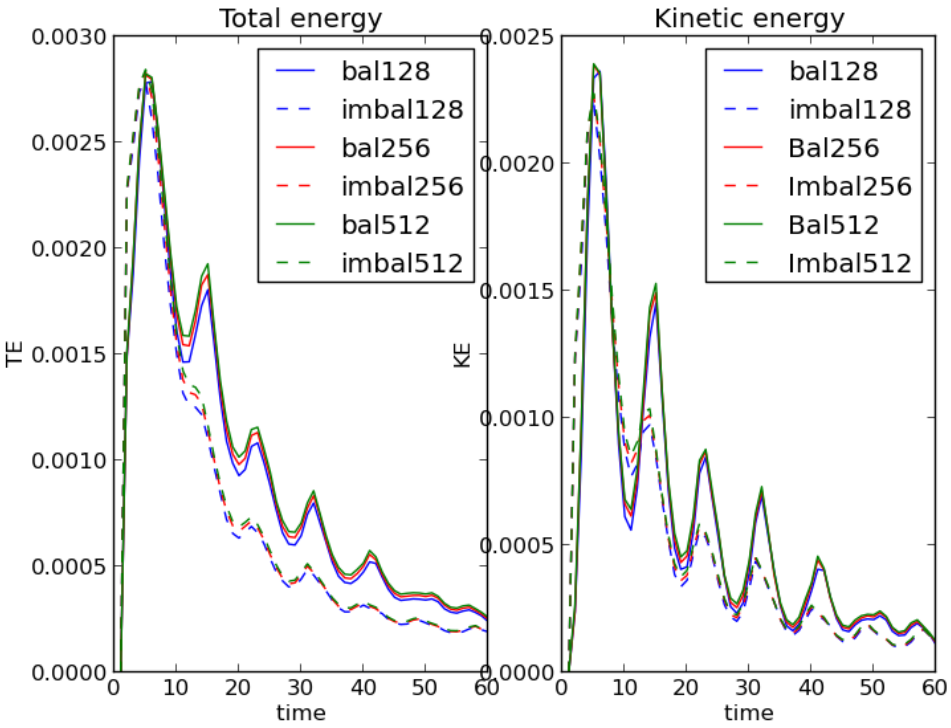

Figure 1.11: Energy decay of balanced and imbalanced turbulence in 1D in different resolutions 128, 256 and 512. The total energy is presented in the left plot and the kinetic energy in the right plot. The balanced turbulence is denoted by bold lines whereas the imbalanced turbulence by dashed lines. Different colors represent different resolutions. It is seen that the imbalanced turbulence decays faster than the balanced one.

From Figure 1.11 it is seen that the kinetic and total energy decay/cascade in the imbalanced case is faster than balanced turbulence in 1D. This is similar to the result obtained by (Suzuki et al. 2007).

Figure 1.12 presents the comparison of energy decay for a 3D simulation between balanced and imbalanced turbulence.

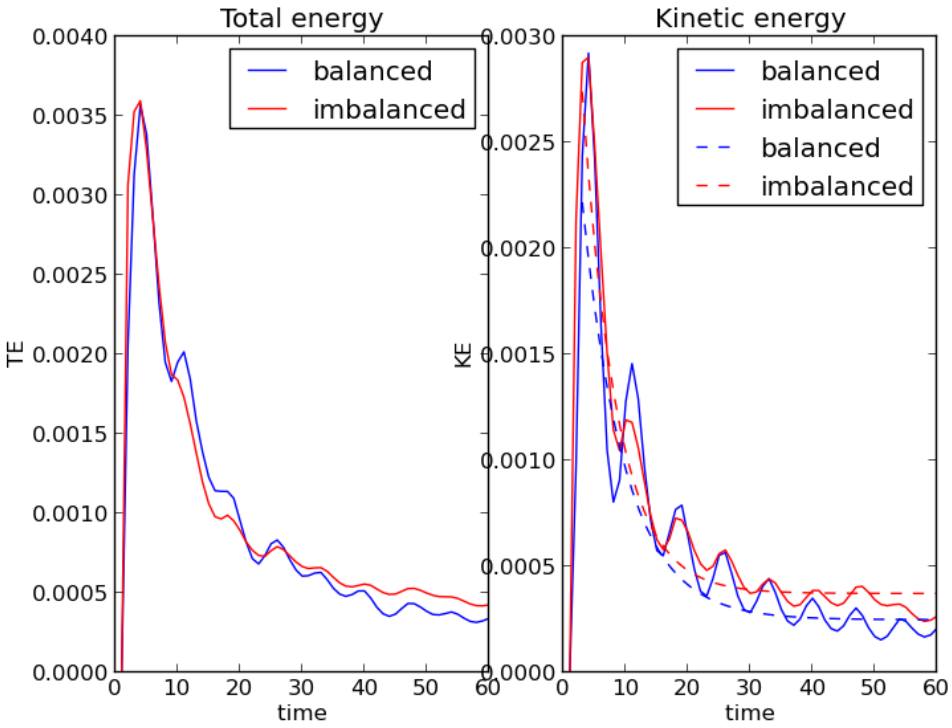

Figure 1.12: Energy decay of balanced and imbalanced turbulence in 3D. The total energy is presented in the left plot and the kinetic energy in the right plot. The balanced turbulence is denoted by blue bold lines whereas the imbalanced turbulence by red bold line. In the kinetic energy plot, the dashed lines represents the fitted lines corresponding to the bold lines in case of balanced and imbalanced turbulence. It is seen that there is not much difference in the decay/cascade between balanced and imbalanced fast mode turbulence in 3D turbulence.

The kinetic and total energy decay as seen from Figure 1.12 reveals that there is no big difference between the decay/cascade process of balanced and imbalanced turbulence in 3D when the number of grid points are 512 in unit box length.

1.6 Conclusion

In this chapter, numerical simulations are carried out to generate fast mode MHD turbulence and study their properties. The turbulence is generated without any continuous driving force. The turbulence therefore decays with time. The injection of wavevectors to generate turbulence is carried out in two different ways. In one scenario wavevectors are injected collinearly and in the other scenario wavevectors are injected isotropically. The injected wavevectors are varied in these simulations to study the dependence of turbulence properties with the injection wavevector. The fast mode MHD turbulence generated are studied from their 1D and 2D energy spectrum, 2D structure functions and cascade/decay rates. Also simulations are carried out to study the difference between balanced and imbalanced fast mode MHD turbulence in 1D and 3D and in different resolutions. The main results from the current study are summarized below.

1. 3D fast mode MHD turbulence in the current simulations have a 1D energy spectrum proportional to k^{-2} in contrast to spectral density of weak acoustic turbulence with a spectral index of -1.5. This is a signature that shocks are developed in the current fast mode simulations.

2. 3D MHD fast mode turbulence generated from the current simulations is isotropic in nature as determined from their 2D energy spectrum and 2D structure functions.

3. The cascade/decay rate of fast mode MHD turbulence is proportional to $k^{-0.5}$ in different kinds of wave vector injection.

4. 1D imbalanced turbulence decays/cascades faster that balanced turbulence but this is not observed in 3D MHD fast mode turbulence from the current simulations of resolution 512.

2 Cosmic Ray Transport in MHD Turbulence

2.1 Introduction

Discovery

The discovery of cosmic rays was first due to Victor Hess in 1912 when he measured atmospheric ionization using electrometers in his hot air balloon flight experiments which travelled up to an altitude of 5 km above ground level and noted rising radiation levels with rising altitude. He concluded that the radiation is of extra-terrestrial origin and is of very high penetrating power which enters from above into our atmosphere. Speculations were surmounting over the nature of this radiation. Robert Millikan, who was investigating this radiation, proposed that they were gamma rays coming from outer space and therefore he called them "cosmic rays." But in the next decades evidence was mounting that cosmic rays were, in fact, mostly energetic particles. In the early 1930s, Walter Baade and Fritz Zwicky proposed that the origin of cosmic rays were due to supernovas. In 1938 Auger had discovered extensive air showers, which are showers of secondary subatomic particles formed when primary high-energy particles collide with air molecules in the upper atmosphere. On the basis of his measurements, Auger concluded that he had observed showers with energies of $10^{15} eV$ which was ten million times higher than any known at that time. From the 1930s to the 1950s, cosmic rays served as a source of particles for high energy physics investigations in cloud chambers, and led to the discovery of subatomic particles like the antimatter positron and the heavier lepton muon. A theory of the acceleration mechanism of cosmic rays through interstellar space was proposed by Enrico Fermi in 1949. According to him, protons accelerate by bouncing off moving magnetic clouds in shocks which are generated from supernovae. The highest energy cosmic ray that has ever been observed is called the "Oh-My-God" particle. This was an ultra-high-energy cosmic ray (UHECR) detected by the Fly's Eye camera (HiRes) in Dugway Proving Ground, Utah, U.S in 1991, with energies around $3 \times 10^{20} eV$. Tracing back high-energy cosmic rays to their unknown source will advance the understanding of the origin and evolution of the universe.

Composition, energy spectrum and origin

Cosmic rays are non-thermal, high energy, subatomic charged particles coming from outer space, travelling close to the speed of light, to reach earth. Cosmic ray particles that come from beyond our solar system are extremely energetic (GeV to EeV) and highly relativistic. They are very stable and travel for millions of years through our galaxy or from far away galaxies before reaching earth. The cosmic rays that originate from outside the earth's solar system are called primary cosmic rays. Energetic particles from the sun, at a lower energy range (MeV and GeV) also contribute to the cosmic ray flux on earth. Upon encountering the earth's surface, the cosmic rays interact with the nuclei of the air molecules and form a cascade of secondary lighter particles in the form of an air shower. These are called secondary cosmic rays and include photons, leptons, and other hadronic components. About 99 % of primary cosmic rays are the bare nuclei of well known atoms and the rest 1 % are solitary electrons. Of the nuclei, about 90 % are observed to be simple protons, 9 % are alpha particles, identical to helium nuclei and the remaining 1 % are the nuclei of heavier elements called HZE ions, eg carbon, oxygen, nitrogen, iron. A very small fraction of stable particles of antimatter, such as positrons and antiprotons has also been observed in the cosmic ray flux. The primary cosmic ray flux energy spectrum spans for more than 11 decades in the range of GeV ($10^9 eV$) to EeV ($10^{18} eV$). The energy and flux of the cosmic rays are related to their sources or the highly energetic astrophysical events that create them. The origin and source of the cosmic rays (where they come from) and how they gain so much high energies are a source of active research in high energy astrophysics. At low energies, the majority of primary cosmic rays originate from supernova remnants (SNR) within our galaxy Milky Way and are known as galactic cosmic rays (GCR), or are solar energetic particles. For the galactic cosmic rays, upon acceleration by supernova shocks, they follow a diffusive propagation through the galactic magnetic fields, until they leave the Galaxy or reach earth. At high energies, the extra-galactic cosmic rays that enter the solar system from beyond our Milky Way galaxy dominates the highest energy cosmic ray spectrum. The exact transition energy from galactic to extra-galactic cosmic rays occurs is not very clear, but it is roughly in the range 10^{17} to 10^{18} eV, which is also referred to as the ankle of the cosmic ray energy spectrum. Compared to the high flux of GCR which is around 1 particle $m^{-2}s^{-1}$, the flux of these extra-galactic UHECR are extremely low and is around 1 particle $km^{-2}s^{-1}$. Their possible sources are of extra-galactic origin, such as in the active galactic nuclei, cluster of galaxies, gamma-ray bursts, and neutron stars.

Importance of MHD turbulence in CR transport

The transport of primary cosmic rays and dust grains through interstellar, intergalactic and intracluster space, their acceleration mechanisms and sources are still an ongoing subject of research in cosmic ray astrophysics. All of the interstellar, intergalactic and intracluster medium are filled with astrophysical fluids and are in the state of plasma. These fluids are mediated by electric and magnetic fields. These fluids are highly conducting and usually have very high Reynolds number therefore being highly turbulent in nature. Magnetic turbulence is ubiquitous in astrophysical systems and ranges in scale from kms to kpc. The study of transport of cosmic rays through magnetic turbulence which is ubiquitous in astrophysical plasmas could reveal understanding of fundamental physical processes responsible for particle scattering, confinement and acceleration. Also it helps to understand the nature of magnetohydrodynamic (MHD) turbulence itself which is still in progress and simultaneously linked with the advancement of cosmic ray studies.

Interaction of MHD turbulence with CR

"The propagation, scattering and acceleration of cosmic rays (CRs) and dust grains in any astrophysical medium is affected by their interaction with turbulent magnetic fields (MHD turbulence) in the medium. The scattering of CR is efficient when their interaction with turbulent magnetic field in the medium satisfies resonance conditions.

Gyroresonance

Gyroresonance or cyclotron resonance occurs when the interactions between a charged particle and a plasma wave is such that the wave frequency is a multiple of the particle's Larmor frequency:

$$\omega - k_{\|} v\mu = n\Omega \tag{2.1}$$

where ω is the wave frequency, $\Omega = \Omega_0/\gamma$ is the particle's relativistic gyration frequency, $\mu = cos\theta$, θ is the pitch angle of particles and $(n = 0, \pm 1, \pm 2...)$.

TTD

The scattering of CR is also highly efficient when their interaction with the turbulent fields satisfies a nonresonant condition called transient time damping [TTD].

TTD results from compressible perturbations only in MHD turbulence and corresponds to $n = 0$ in the gyroresonance condition. TTD occurs when the phase speed of the magnetic field compression ($v_{\parallel} \approx \omega/k_{\parallel}$) is similar to the particle speed. The particles undergo several reflections or collisions within the magnetic mirrors and therefore are able to escape them for scattering and acceleration.

Streaming instability

The third mechanism is called streaming instability which is also an efficient alternative for scattering of cosmic rays. When CRs stream at a velocity much larger than the Alfvén velocity, they can excite slab Alfvénic MHD modes as a feedback. These, in turn, scatter CRs back. This runaway process is known as streaming instability. Turbulence could also partially suppress streaming instability due to the nonlinear interaction with turbulence. The resonant streaming instability is important for confining cosmic rays with energies up to 100 GeV in the galaxy (Cesarsky 1980; Longair 1997).

Astrophysical implications

These resonant interactions are responsible for scattering of cosmic rays and isotropizing them thereby confining the cosmic rays in our galaxy for a longer time. Efficient scattering is also required for the acceleration of cosmic rays in turbulent medium. For example in diffusive shock acceleration the scattering back of cosmic rays into the shock is necessary for the mechanism of first order Fermi acceleration to happen efficiently (Longair 1997). Also, stochastic acceleration or second order Fermi acceleration of cosmic rays in a turbulent medium would require efficient scattering.

Therefore the diffusion of particles both in the parallel and perpendicular directions to the mean magnetic field controls the penetrations and modulation of solar energetic particles in the heliosphere, the confinement and escape of galactic cosmic rays and the efficiency of acceleration mechanisms like diffusive shock acceleration."

CR transport studies in slab, composite mode turbulence

As already stated before, the advancement of study of CR transport goes hand in hand with the advance of MHD turbulence theory. "There was a surge of research trying to develop models of CR transport in astrophysical turbulence and study CR pitch angle diffusion and scattering in the 1960s and 1970s. Both quasilinear theory

(QLT) (Jokipii 1966) and non linear theory (NLT) (Dupree 1966; Goldstein 1976; Jones et al. 1973; Voelk 1975; Völk 1973) were employed to study CR scattering. While QLT assumes that the particle orbits are unperturbed, NLT considers perturbations of particle orbits. The nonlinear theories tried to address the problem of scattering of particles with 90 degree pitch angle correctly which was not possible with QLT. Numerical simulation also confirmed that there was finite scattering at 90 degree pitch angle (Kaiser et al. 1978).

The transport of cosmic ray perpendicular to the background magnetic field has been a source of debate for many decades. The first theoretical approach was the application of QLT to particle transport in a magnetostatic slab model of turbulence which leads to a field line random walk (FLRW) or normal diffusive behaviour (Jokipii 1966). Several numerical simulations were carried out in the past decades to study perpendicular transport. By using test particle simulations Qin et al. 2002 demonstrated that the FLRW-limit is incorrect and perpendicular transport in a magnetostatic slab model is sub-diffusive. This conclusion was supported theoretically be invoking a compound diffusion model (Kóta and Jokipii 2000). However, some other numerical simulations using test particle approach demonstrated that diffusion is recovered if the slab model is replaced by a slab/2D composite model (Giacalone and Jokipii 1999; Qin et al. 2002). However the researchers were using synthetic data for magnetic turbulence. The problem with such kind of data is that it is difficult to include scale dependant anisotropy with respect to the local magnetic field in these turbulence and hence is not a correct model of MHD turbulence like the GS95 model (P. Goldreich and Sridhar 1995).

In the past two decades, more attempts were made to develop the nonlinear theory of CR scattering include the nonlinear guiding center theory (W. H. Matthaeus et al. 2003), weakly nonlinear theory (Shalchi et al. 2004), and second-order QLT (Le Roux and Webb 2007; Qin 2007; Shalchi 2005; Shalchi 2006; Webb et al. 2006). These analysis were however using the traditional 2D MHD and slab models of MHD turbulence (Bieber et al. 1988; Pryadko and Vahe Petrosian 1999). In the slab model of Alfvénic turbulence, only Alfvén waves propagating along an external magnetic field are considered. The slab model is incompatible for explaining perpendicular transport, since the particles are tied forever to the same magnetic field lines. These models were simple and were able to account for the propagation of CR in the solar wind and the magnetosphere for example."

CR transport studies in GS95 turbulence

"The most important development in the understanding of MHD turbulence was due to the GS95 model. The analytical theory of GS95 predicted that Alfvén modes in incompressible MHD turbulence would have a scale dependant anisotropy. Several numerical simulations carried out in the next years (J. Cho and Lazarian 2003; J. Cho, Lazarian, and E. T. Vishniac 2002; Jungyeon Cho and Lazarian 2002; Jungyeon Cho and Ethan T. Vishniac 2000; Maron and Peter Goldreich 2001; Müller and Biskamp 2000) confirmed that Alfvén modes in MHD turbulence has scale dependant anisotropy consistent with the analytical theory of GS95. Around the same time, analytical studies of CR scattering in incompressible MHD turbulence with GS95 spectrum were carried out using QLT. Due to the anisotropy of such turbulence the pitch angle scattering of CR was found to be extremely low (Chandran 2000). Another attempt was made by (Lerche and Schlickeiser 2001) to study CR scattering in anisotropic MHD turbulence". Numerical simulations were carried out to test the nonlinear theory in incompressible GS95 type turbulence (Beresnyak et al. 2011).

CR transport studies in CL02 turbulence

"The above studies however did not consider compressible turbulence into account. A more accurate description of MHD turbulence was obtained by Cho and Lazarian (J. Cho and Lazarian 2003; Jungyeon Cho and Lazarian 2002) by considering compressibility in turbulence. The MHD turbulence in these studies were also decomposed into Alfvén, fast and slow modes. While the Alfvén and slow modes are anisotropic, fast modes are relatively isotropic in nature. The fast modes were suggested to follow an acoustic type of cascade (J. Cho and Lazarian 2003; Jungyeon Cho and Lazarian 2002). Using the quasilinear theory (QLT) in such tested model of turbulence (J. Cho and Lazarian 2003), Yan and Lazarian for the first time showed that compressible fast modes are responsible for most of the scattering of particles (Yan and Lazarian 2002; Yan and Lazarian 2004). However QLT has some shortcomings. It cannot treat the scattering of particles with 90 degree pitch angle. It can also not account for the perpendicular transport of particles. A further development of CR transport was made using the nonlinear theory (NLT) by Yan and Lazarian (H. Yan and Lazarian 2008) which also showed that fast modes are responsible for much particle scattering compared to the other MHD modes. The contribution of TTD by compressible modes obtained were more prominent from NLT. The NLT also addresses the issue of perpendicular transport of cosmic rays and super-diffusion of CR upon interaction with small scale eddies of turbulence (Lazarian and Yan 2014; H. Yan and Lazarian 2008). Numerical simulations were carried out to test

the nonlinear theory in compressible CL02 type turbulence (Xu and Huirong Yan 2013).

Aim of current study and possible future extensions

In this thesis, CR test particle scattering is studied in numerically tested models of MHD turbulence. "The test particle approach is a conventional numerical method for studying CR of negligibly small density in which case the collective effects are not considered as important. However, in real astrophysical environments, CR density is not actually small and the CR pressure could be dynamically important. Nevertheless, the test particle limit provides a firm ground for future research into the more general and difficult problem of mutual interaction of CR and MHD fluid".

The focus of study in this thesis is to build up on the previous numerical simulations of CR transport in MHD turbulence (Beresnyak et al. 2011; Xu and Huirong Yan 2013) and carry out further detailed analysis of CR transport in decomposed compressible MHD turbulence that directly confronts the nonlinear theory (Lazarian and Yan 2014; H. Yan and Lazarian 2008)" with regard to CR scattering and perpendicular transport. The scattering of cosmic rays under the influence of different MHD modes are studied, along with the dependence of CR scattering on to the initial pitch angle of CR. The perpendicular transport of CR is studied in both large scale and small scale eddies. The analysis is done with respect to both global and local magnetic fields. CR transport in both sub-Alfvénic and superAlfvénic turbulence is studied. Importantly, CR of various mean free paths and their transport is also the basis of this study.

In the current thesis the back reaction of cosmic rays to the MHD turbulent fluid is not considered. This kind of mechanism leads to a process called streaming instability which could be a very important mechanism for CR scattering (R. Kulsrud and Pearce 1969) with energy below 100 GeV. The feedback of CRs on turbulence, in the form of gyroresonance instability (Huirong Yan and Lazarian 2011), could also be additionally studied and all these problems opens up scoped for future research in CR transport.

2.2 Review of theory on particle transport in test model of turbulence

In this review section a brief overview of the conclusions from Quasilinear Theory (QLT) and the Nonlinear Theory (NLT) is provided. An important aspect of perpendicular transport addressed by the NLT is also discussed. Most of the content presented in this section is from (Lazarian and Yan 2014; Yan and Lazarian 2002; Yan and Lazarian 2004; H. Yan and Lazarian 2008).

CR SCATTERING FROM QUASILINEAR THEORY:

The results from applying QLT to CR transport in compressible MHD turbulence is summarised below:

1) "CR scattering due to Alfvén and slow mode turbulence is inefficient and marginal. Due to the anisotropic nature of such modes, resonant interaction of CR with Alfvén and slow mode turbulence through gyroresonance is suppressed very much and therefore CR scattering due to such MHD modes becomes negligible (Chandran 2000; Yan and Lazarian 2002; Yan and Lazarian 2004). CR scattering due to Alfvén and slow modes are similar because they have similar anisotropic structure and scaling relations. For very high energy CRs($> 10^8 GeV$) Alfvén mode scattering can not be neglected."

2) "CR scattering due to fast modes is very efficient and is the dominant scattering mechanism when energy is injected at large scales. Gyroresonance with fast modes is the principal mechanism that scatters CR (Yan and Lazarian 2002). Unlike Alfvén modes, fast modes suffer viscous and collisionless damping, but still it dominantly contributes to CR scattering".

Limitations of QLT:

"The QLT describes CR dynamics in a local magnetic field system of reference and the key assumption of QLT is that the particle's orbit is unperturbed. While QLT provides simple physical insights into scattering, it is known to have problems".

1) "QLT has problems in treating scattering of cosmic rays when their momentum is nearly perpendicular to the magnetic field (Felice and R. M. Kulsrud 2001; Goldstein 1976; Jones et al. 1973; Owens 1974; Voelk 1975; Völk 1973). It fails in treating 90

degree scattering which could be addressed with the NLT. The contribution of TTD is improperly treated in QLT".

2) "QLT does not take into account the diffusion of CR that follow wandering magnetic lines. This problem of addressing the perpendicular transport of cosmic rays at small scales (Kóta and Jokipii 2000; W. H. Matthaeus et al. 2003) is addressed with the NLT".

CR SCATTERING FROM NON LINEAR THEORY:

The NLT is an improvement over the QLT and takes into account the perturbations in particle's orbit. Thus it is able to account for both the problems of perpendicular transport and 90 degree scattering along with considering the important process of TTD scattering.

"The results from applying nonlinear theory to CR transport in incompressible and compressible MHD turbulence is summarised below. It is seen that the nonlinear effects are very important for the scattering of cosmic rays".

1) "The overall CR scattering is dominated by the TTD interaction with compressible fast modes, especially at large pitch angles and up to 90 degrees. CR scattering due to TTD interaction is negligible at small pitch angles. Nevertheless the overall CR scattering is still largely due to TTD mechanism in comparison to gyroresonance mechanism. The contribution of TTD interactions in CR scattering is a important consequence of the NLT. There is a difference between the results obtained from QLT and NLT at large pitch angles".

2) "The contribution of gyroresonance in CR scattering occurs at small pitch angles. CR scattering due to gyroresonance of incompressible Alfvén MHD turbulence is marginal. The fast modes dominates the gyroradius interaction in comparison to Alfvén modes. Even though the overall contribution of GR to CR scattering is less, it should be important for confining the CRs at small pitch angles. The results for gyroresonance scattering are the same as obtained from QLT and NLT".

4) "The fast modes contributes majorly to the overall CR scattering in our galaxy for example in the warm interstellar medium(WIM) and the galactic halo".

PERPENDICULAR TRANSPORT AND RICHARDSON DIFFUSION OF CR

"The perpendicular transport of cosmic rays with respect to mean magnetic field is explored here. The relevance of such studies is related to many astrophysical environments for example our heliosphere and our galaxy where a mean magnetic field is present. Cross field transport is still debatable and yet to be confirmed even though it is fundamentally important. Many studies have proposed that CR cross-field transport is subdiffusive in nature. (Getmantsev 1963; Kóta and Jokipii 2000; Mace et al. 2000; Qin et al. 2002; Webb et al. 2006). The observations of solar energetic particles in the heliosphere contradict the above theory (Perri and Zimbardo 2009). Their analysis reveals that the propagation of energetic ions accelerated at the solar wind termination shock corresponds to superdiffusive transport. This is the first direct experimental evidence of ion superdiffusion in space plasmas. The solar energetic particle fluxes measured at different heliocentric distances indicate a faster diffusion process perpendicular to the solar magnetic field than subdiffusion (Maclennan et al. 2001)".

"The QLT faces serious difficulties in explaining CR propagation perpendicular to the mean magnetic field. Recent calculations of CR perpendicular transport have been based on the NLT of CR transport in tested GS95 model of turbulence (H. Yan and Lazarian 2008). This study has shown that subdiffusion does not apply ,and instead, CR cross-field transport undergo normal diffusion on large scales and superdiffusive on smaller scales less than the injection scale of turbulence. It follows from the GS95 theory that the displacement squared in the perpendicular direction to the mean magnetic field is proportional to the third power of the distance along the magnetic field for superdiffusion (Lazarian 2006; Lazarian and Ethan T. Vishniac 1999; Lazarian and Yan 2014; Narayan and Medvedev 2001; H. Yan and Lazarian 2008)".

In the following paragraphs, "the perpendicular diffusion of CR upon interaction with small scales eddies, less than the energy injection scale, L of turbulence is discussed in particular. The turbulent magnetic fields diverge over scales less than L (smaller scales) and undergo the phenomena of Richardson super-diffusion. The magnetic fields lines undergo random walk and normal diffusion above the energy injection scale L (larger scales). CR transport in small scale Alfvénic turbulence is described for both sub-Alfvénic and super-Alfvénic conditions. CR with both $\lambda_{\parallel} > L$ and $\lambda_{\parallel} < L$ are considered. This explains CR propagation and acceleration in a variety of astrophysical environments".

Perpendicular Diffusion of CR with $\lambda_{\parallel} > L$ along wandering magnetic field lines :

"When the mean free path, $\lambda_{\parallel}$ of CR is greater than the energy injection scale, L of MHD turbulence, the CRs undergo a streaming motion along magnetic fields and their diffusion perpendicular to mean magnetic field is determined by the divergence of magnetic field lines. The cosmic ray trajectories trace magnetic field lines and therefore the divergence of CR trajectories is identical to that of magnetic field".

"Let us consider first strong turbulence with $M_A < 1$ (subAlfvénic). The divergence of the field lines starts at points displaced by vector l. This displacement increases as one moves a distance 's' in arc length along the field line passing through the two points. The change in separation is given by the following equation,

$$\frac{d\mathbf{l}(s)}{ds} = \hat{\mathbf{b}}(\zeta'(s)) - \hat{\mathbf{b}}(\zeta(s)) \tag{2.2}$$

where $\mathbf{l}(s) = \zeta'(s) - \zeta(s)$ and $\hat{b} = B/|B|$ is the unit tangent vector along the magnetic field line. From this equation, one derives the following equation(Lazarian and Yan 2014),

$$\frac{dl_{\perp}{}^2}{ds} \sim D_{\perp}(l) \sim L(\frac{l_{\perp}}{L})^{4/3} M_A^{4/3} \tag{2.3}$$

The solution of the above equation is given as,

$$l_{\perp}^2 \sim \frac{s^3}{27L} M_A{}^4 \tag{2.4}$$

From the above equation it is seen that the perpendicular diffusion has a dependence of M_A^4 instead of M_A^2 in the classical studies(Jokipii and Parker 1969). This signifies a stronger suppression of perpendicular diffusion by magnetic field. As is seen for Richardson diffusion it is required that scales s are less than the turbulent injection scale L. Numerical simulations by (Xu and Huirong Yan 2013) validate this result for incompressibly driven turbulence. The Richardson law in terms of magnetic field separation in time was confirmed with numerical simulations involving many time frames of the driven MHD turbulence (Eyink et al. 2013)".

"Now lets look at turbulence with superAlfvenic Mach no i.e. MA > 1. At scales larger than the Alfvénic scale l_A the dynamics of magnetic field is dominated by

hydrodynamic turbulence. For scales smaller than l_A the turbulence is of GS95-type with the injection scale of L = lA and the injection velocity VL = VA. The separation of magnetic field lines is given as,

$$l_\perp^2 \sim \frac{s^3}{27L_A} \sim \frac{s^3}{27L}{M_A}^3 \tag{2.5}$$

where the M_A^3 dependence reflects the fact that the GS95 cascade starts at l_A rather than at the injection scale of turbulence L. The reason for this is that the magnetic fields at scale less than l_A are stiffer and are not bent by hydrodynamic turbulence.

Therefore, from the above discussions, streaming CRs move along the diverging magnetic field lines and undergo superdiffusion. For subAlfvénic turbulence i.e. $M_A < 1$ the superdiffusion is present perpendicular to magnetic field in the range of perpendicular scales $[l_{min}, l_{trans}]$. For super Alfvénic turbulence with $M_A > 1$, the superdiffusion of CRs streaming along magnetic field lines experience anisotropic superdiffusion which is present perpendicular to the magnetic field at the scales less than l_A".

Perpendicular Diffusion of CR with $\lambda_{\parallel} < L$ along diverging magnetic field lines :

"When the mean free path, $\lambda_{\parallel}$ of CR is less than the energy injection scale, L of MHD turbulence, the CR instead of streaming or moving ballistically diffuse or scatter more. The superdiffusion in this case is also different from the case when the $\lambda_{\parallel}$ is greater than L, due to multiple scattering.

When CR of such small $\lambda_{\parallel}$ compared to L encounters large scale eddies (scales $\gg L$), the perpendicular diffusion coefficient in the global frame of reference for subAlfvénic M_A ($M_A < 1$) is given by (Lazarian and Yan 2014; H. Yan and Lazarian 2008),

$$D_\perp \approx D_{\parallel}{M_A}^4 \tag{2.6}$$

This involves a random walk process of CR with a time step of $L^2/D_{\parallel}$. This result is also similar to the diffusion of thermal particles obtained from thermal conduction (Lazarian 2006).

When CR of such small $\lambda_{\parallel}$ compared to L encounters smaller eddies (scales less than L), the perpendicular displacement and parallel displacement with respect

to the mean magnetic field for subAlfvénic M_A is given as(Lazarian and Yan 2014) respectively,

$$l_\perp{}^2 \sim \frac{(D_\parallel \delta t)^{3/2}}{27L} M_A{}^4, \tag{2.7}$$

$$l_\parallel{}^2 \sim (D_\parallel \delta t), \tag{2.8}$$

When CR of such small $\lambda_\parallel$ compared to L encounters smaller eddies at scales less than the Alfvénic scale l_A, i.e. for scales $[l_{min}, l_A]$, the perpendicular displacement with respect to the mean magnetic field for superAlfvénic M_A is given as(Lazarian and Yan 2014) respectively,

$$l_\perp{}^2 \sim \frac{(D_\parallel \delta t)^{3/2}}{27L} M_A^3 \tag{2.9}$$

From Eqn. 2.7 and Eqn. 2.9 it is seen that the perpendicular displacement exhibit superdiffusive behaviour, even though the rate of superdiffusion is reduced compared to that of Richardson diffusion in case of $\lambda_\parallel > L$. While it is known that Richardson growth is proportional to $t^{3/2}$, it is expected that for the current situation, the diffusive propagation of CR is proportional to $t^{3/4}$".

2.3 Numerical setups

CR TEST PARTICLE SIMULATIONS AND LORENTZ FORCE

In the current study, "test particle simulations are carried out in the presence of MHD turbulence to trace the trajectories of CRs. Since the relativistic particles considered in the current study have speed much larger than the Alfvén speed, the magnetic fields are considered as stationary, and the electric fields in the turbulent plasma are neglected for the study of CR transport. The particle motion is governed by the relativistic Lorentz force equation given by,

$$m\gamma \frac{d\mathbf{v}}{dt} = q(\mathbf{v} \times \mathbf{B}) \tag{2.10}$$

where q, m and **v** represents the charge, mass and velocity of the particles, respectively. γ is the Lorentz factor and **B** is the turbulent magnetic field. The Larmor radius of the particle is,

$$r_L = mc^2\gamma/eB_0 \tag{2.11}$$

The particle trajectory tracer follows the Bulrisch Stoer method (Press et al. 1986). The periodic boundary conditions are adopted. The CR diffusion coefficients are calculated from the particle trajectory data".

Brief description of Bulirch Stoer algorithm

The Bulirsch Stoer (BS) algorithm is chosen to solve the ordinary differential equations (ODE) governing the trajectories or motion of relativistic cosmic rays. "The BS method is well suited to ODEs which contains smooth functions and have no singular points inside the interval of integration. The BS method is a very efficient method to obtain high accuracy numerical solutions to ODEs with minimal computational effort relative to other commonly used methods".

The BS method combines the ideas of numerical integration and extrapolation method. In the Bulirsch-Stoer method, the integrations are done by the modified midpoint method, and the extrapolation technique is called Richardson's extrapolation. "A single Bulirsch-Stoer step moves point x to $x+H$, where H could be a large distance and not necessarily infinitesimal. This single step is a grand leap consisting of many (e.g., dozens to hundreds) substeps of modified midpoint method, which are then extrapolated to zero stepsize."

The numerical integration is carried out using the modified midpoint method. In this method, the advancement of the vector of the dependant variable $y(x)$ from a point x to a point $x + H$ is carried out in a sequence of n substeps, each of size h. The size of the each substep is given as,

$$h = \frac{H}{n} \tag{2.12}$$

The equations governing the modified midpoint method are as follows,

$$z_0 = y(x) \tag{2.13}$$

$$z_1 = z_0 + hf(x, z_0) \tag{2.14}$$

$$z_{m+1} = z_{m-1} + 2hf(x + mh, z_m) \tag{2.15}$$

for $m = 1, 2, ..., n-1$

$$y(x+H) \approx y_n = \frac{1}{2}[z_n + z_{n-1} + hf(x+H, z_n)] \tag{2.16}$$

"The z's in the above equations are intermediate approximations which advances in steps of h whereas the final approximation to $y(x+H)$ is denoted by y_n. This method is primarily a centered difference or midpoint method, except at the first and last points which gives it the name modified midpoint method."

"The modified midpoint method is a second-order method. It has an advantage over the second order Runge-Kutta (RK2) in that it calculates only one derivative per step h instead of two required in RK2 method."

"The important consequence arising out of Eqn 2.16 which makes the modified midpoint method particularly useful for the BS technique is that the error in 2.16 contains only even powers of the stepsize h when expressed as a power series in h.

$$y_n - y(x+H) = \sum_{n=1}^{\infty} \alpha_i h^{2i} \tag{2.17}$$

where H is a constant, and h changes by varying n in Eqn 2.12. The usefulness of the even power series is that by ignoring the higher-order terms, two orders of accuracy can be gained. For example, when n is even, and $y_{n/2}$ denote the result of applying Eqn 2.12 and Eqn 2.16 with half the number of steps, $n \longrightarrow n/2$, then,

$$y(x+H) \approx \frac{4y_n - y_{n/2}}{3} \tag{2.18}$$

is fourth-order accurate. This is similar to the result obtained from fourth-order Runge-Kutta, but requires only about 1.5 derivative evaluations per step h instead of Runge-Kutta's evaluations of 4 derivatives. It is sometimes called the Gragg–Bulirsch–Stoer (GBS) algorithm because of the importance of a result about the error function of the modified midpoint method, due to William B. Gragg."

Therefore, to summarize, "the modified midpoint method by itself is a second-order method and is therefore generally inferior to fourth order methods like RK4 but as discovered by Gragg, the error of a modified midpoint step of size H, consisting of n substeps of size $h = H/n$ each, and expressed as a power series in h, contains only even powers of h which makes the modified midpoint method extremely useful to the Bulirsch–Stoer method as the accuracy increases two orders at a time. The

other important advantage of this method is that it calculates one derivative per substep compared to other methods of similar accuracy which calculates more derivatives per substep."

" Bulirch and Stoer proposed a sequence of separate attempts to advance the interval H which is made of increasing values of n, the number of substeps.

$$n = 2, 4, 6, 8, 12, 16, 24, 32, 48, 64, 96, ..., [n_j = 2n_j - 2], ... \tag{2.19}$$

For each step, it is not known in advance how far up this sequence would go. After each successive n is tried, a polynomial extrapolation is attempted which returns both the extrapolated values and the error estimates. If they are not satisfactory, the n is increased. If they are satisfactory, the next step is pursued with $n = 2$ as the beginning".

MHD TURBULENCE DATA CUBES

The MHD turbulent data cubes that have been used in the test particle simulations to study cosmic ray transport and obtain the current results in the thesis are described below. Two kinds of MHD turbulence data cubes are used in which one of them has been more solenoidally driven and the other one has been more compressibly driven. The driving force of turbulence is continuous such that the turbulence reaches a steady state with time.

Solenoidal driven turbulence(CL Code, PENCIL Code)

"3D MHD simulations are performed to generate turbulence data cubes using two types of MHD codes: the one based on (Jungyeon Cho and Lazarian 2002) (Let's call it the CL code); the other with PENCIL codes [1]. The turbulence data cubes are set with $L_{box}^3 = 512^3$ resolution, energy injection scale $L \sim 0.4L_{box}$. The 3D turbulences are driven by solenoidal forcing. Upon the full development of MHD turbulence, snapshots of turbulence are employed in the test particle simulations. The external mean magnetic field is modulated to produce MHD turbulence with different Alfvénic Mach number M_A, defined by:

$$M_A \equiv < \frac{\delta V}{V_A} > \sim \frac{\delta B}{B_0} \tag{2.20}$$

1 Please see http://pencil-code.nordita.org for details.

Here the quantity δV is the turbulent velocity field, V_A is the Alfvénic velocity, the symbol "< ... >" indicates the spatial average, δB and B_0 are turbulent and average magnetic field, respectively. The M_A values of the generated turbulence data cubes from CL and PENCIL method are listed in Table 2.1. CR transport in decomposed MHD modes is also considered. Based on the method described in (J. Cho and Lazarian 2003; Jungyeon Cho and Lazarian 2002), the 3D MHD turbulence from PENCIL is decomposed into three eigenmodes, Alfvén, slow and fast. While the CL type turbulence is not decomposed into MHD modes, the PENCIL type turbulence is decomposed into MHD modes. The energy of the magnetic fluctuations for the decomposed modes are normalized to the same amplitude as the total turbulence data cubes in this case. Hence the decomposed modes and the total turbulence have the same M_A for studying test particle simulations in MHD turbulence generated from PENCIl".

Solenoidal Driving						
M_A for simulations in whole turbulence data						
0.44	0.56	0.65	0.83	1.28	1.40	1.54
M_A for tests in decomposed turbulence data						
0.40	0.50	0.65	0.68	0.73	0.80	0.91

Table 2.1: This table lists the Alfvénic Mach numbers of turbulence data cubes employed in our simulations. The first row are whole turbulence data cubes (CL) and not decomposed. The second row are the data cubes with decomposition performed (PENCIL).

Compressible driven turbulence

"Compressible 3D MHD simulations were performed to generate turbulence data cubes using the PLUTO code (Mignone 2007). The PLUTO code solves the ideal MHD equation with no explicit resistivity or viscosity but only numerical dissipation. The equation of state considered here is isothermal. The 3D turbulences are driven by a constant forcing mechanism. Upon the full development of MHD turbulence, snapshots of turbulence are generated which in turn are employed in the test particle simulations".

"The simulation box is a cube and has length dimensions $Lx = Ly = Lz = 1$ and are set with $L_{box}^3 = 512^3$ resolution, energy injection scale $L \sim 0.4 L_{box}$. The normalization is such that the Alfven velocity v_A and the mean magnetic field B_0

are numerically same. The mean field B_0 is in the z direction, which is the global parallel direction".

"The driving of turbulence is carried out by using a readily available forcing module in PLUTO which drives turbulence by adding a force $\mathbf{F}^{turb}$ in both the momentum and energy equations. This force follows the Ornstein-Uhlenbeck(OU) process which is a stochastic differential equation governing the evolution of the force $\mathbf{F}^{turb}$ given as",

$$d\mathbf{F}^{turb}(\mathbf{k},t) = \mathbf{F}_0^{turb}(\mathbf{k})P^{\zeta}(\mathbf{k})dW(t) - \mathbf{F}^{turb}(\mathbf{k},t)\frac{dt}{T} \tag{2.21}$$

"In the above equation, $d\mathbf{F}$ is the force which is added at every time step to the existing force $\mathbf{F}^{turb}(\mathbf{k})$ at wavevector $\mathbf{k}$. The compressive and the solenoidal parts of the force are separated by the projection operator $P^{\zeta}(\mathbf{k})$.

$$P^{\zeta}(\mathbf{k}) = \zeta P^{\zeta}(\mathbf{k}) + (1-\zeta)P^{\zeta}(\mathbf{k}) = \zeta\delta_{ij} + (1-2\zeta)\frac{k_i k_j}{k^2} \tag{2.22}$$

The forcing is purely solenoidal if $\zeta = 1$ and the forcing is purely compressible when $\zeta = 0$. An intermediate value of ζ gives a mixture of solenoidal and compressive forcing. The forcing is such that $k_{min} = 1$ and $k_{max} = 3$ where the 2π factor is neglected".

"MHD turbulence with different Alfvénic Mach number M_A has been generated for compressible driving $\zeta = 0.1$. The Mach number is varied by varying the energy injected in turbulence. CR transport in decomposed MHD modes are considered. Based on the method described in (Jungyeon Cho and Lazarian 2002), the 3D MHD turbulence is decomposed into three eigenmodes, Alfvén, slow and fast. The energy of the magnetic fluctuations for the decomposed modes are normalized to the same amplitude as the total turbulence data cubes. Hence the decomposed modes and the total turbulence have the same M_A".

Compressible Driving						
M_A for tests in decomposed turbulence data						
0.24	0.5	0.6	0.7	0.75	0.81	0.86

Table 2.2: This table lists the Alfvénic Mach numbers of turbulence data cubes generated by compressible driving using PLUTO employed in our simulations. These are the data cubes with decomposition performed.

2.4 CR scattering and pitch angle diffusion

This section presents the results from the scattering experiments performed numerically using an ensemble of charged particles with a specific pitch angle as the initial conditions in MHD turbulence. The scattering experiments were carried out in different MHD modes of MHD turbulence and of various M_A. The pitch angle is defined as the angle between the particle's velocity vector and the local magnetic field vector. The pitch angle changes with time as the charged particles interacts with MHD turbulence which leads to the pitch angle scattering process. The change of the pitch-angle cosine $(\mu - \mu_0)$ is traced for a short interval of time to keep the deviation of μ small (Beresnyak et al. 2011) where μ_0 is the initial pitch angle cosine. The pitch-angle diffusion coefficient $D_{\mu\mu}$ is obtained for an averaged ensemble of charged particles using the following definition,

$$D_{\mu\mu} =< \frac{(\mu - \mu_0)^2}{2t} > \tag{2.23}$$

In the following subsections at first the study of the dependence of CR scattering or the CR pitch angle diffusion coefficient $D_{\mu\mu}$ is carried out in different MHD modes by varying the initial pitch angle (μ_0) in each simulations. Next the study of the dependence of CR scattering or the pitch angle diffusion coefficient $D_{\mu\mu}$ is carried out in different MHD modes by varying the initial gyroradius (r_L) or energy of particles in each simulations. CR scattering is expected to behave differently in different MHD modes as discussed earlier in the review section. CR scattering is also expected to behave differently as the initial pitch angle is varied in different numerical simulations. The results of these numerical tests directly confronts the theoretical predictions made by the nonlinear theory (H. Yan and Lazarian 2008). Most of the results presented next have already been published in the following paper (Maiti et al. 2022) as part of the current thesis work and hence some of the statements are quoted from this paper.

2.4.1 Pitch angle scattering vs initial pitch angle

"CR pitch angle scattering is studied here by injecting CRs into MHD modes with the same initial pitch angle μ_0 but random initial positions. The initial pitch angle cosine μ_0 is varied from 0 to 1 with an interval of 0.05. 10000 particles are used for each test run. The simulations are performed for a few particle gyro periods so that the pitch angle deviation is small (i.e., the root mean square deviation of pitch angle cosine is between 0.01 to 0.1)".

Pitch angle deviation vs initial pitch angle

The pitch angle deviation $(\mu - \mu_0)^2$ with time as CR propagates in Alfvén mode of MHD turbulence is presented in Fig 2.1 for $M_A \sim 0.9$. In this figure the pitch angle deviation is presented for different values of initial pitch angle cosines μ_0 as the initial pitch angle is varied from 0 to 90°.

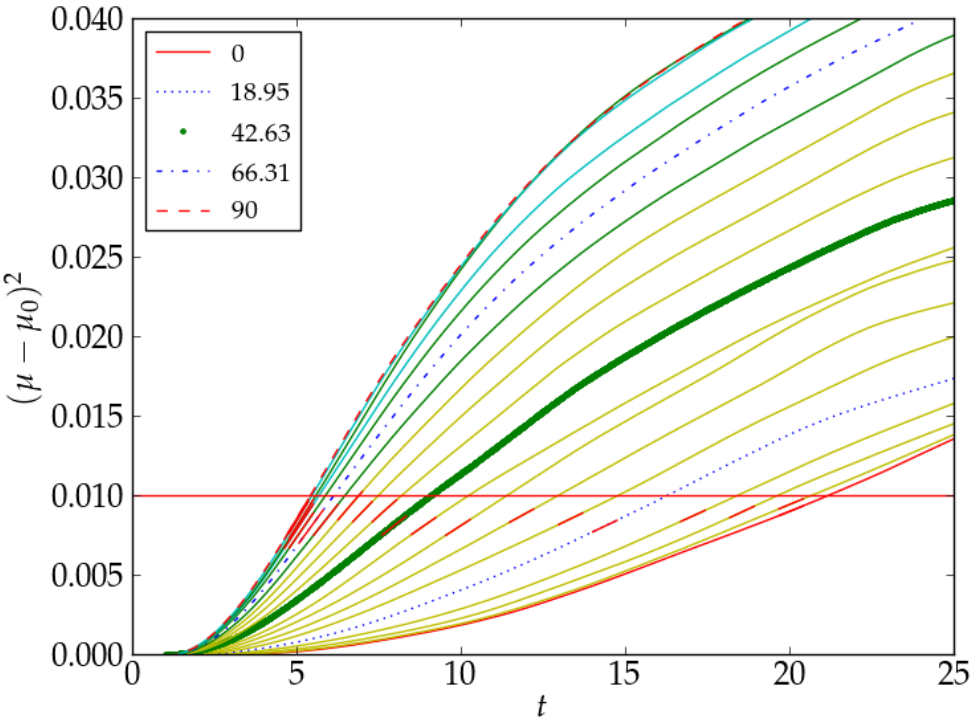

Figure 2.1: Pitch angle deviation for CRs in Alfvén mode of MHD turbulence with $M_A \sim 0.9$. The x axis represents the time, t of CR propagation. The y axis represents the pitch angle deviation, $(\mu - \mu_0)^2$. Different lines represents pitch angle deviation for different initial pitch angle labelled in degrees. The horizontal red denotes the line when the deviation of the pitch angle cosine squared is 0.01.

It is seen from Fig 2.1 that pitch angle deviation increases with time as CR propagates through MHD turbulence. The pitch angle deviation increases as the initial pitch angle is increased in each simulation. At longer times this deviation saturates and becomes constant as is seen in Fig 2.2.

Pitch angle deviation vs Mach number

The variation of pitch angle deviation $(\mu - \mu_0)^2$ with time as CR propagates in Alfvén mode of MHD turbulence is presented in Fig 2.2 for two different cases when extra artificial scattering is introduced in the CR propagation to increase pitch angle scattering and the case when there is no extra artificial scattering introduced. For the former case, the M_A of MHD turbulence is varied to see it's effect on pitch angle deviation. In all these simulations with artificial scattering mechanism introduced or not and different M_A, the results from the same initial μ_0 are compared.

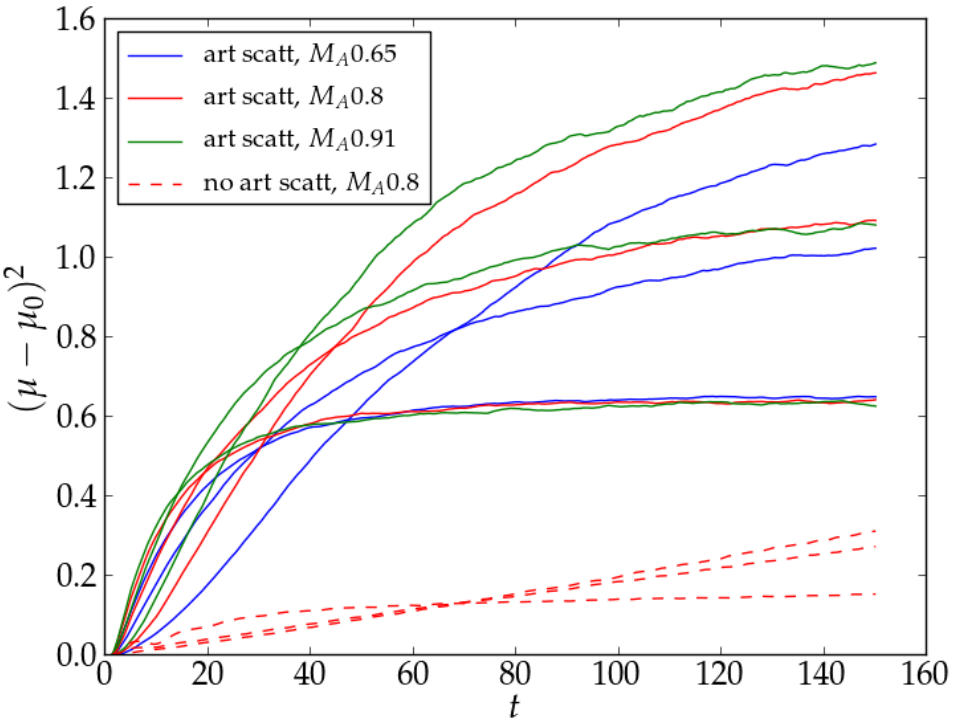

Figure 2.2: Pitch angle deviation for CRs in Alfvén mode of MHD turbulence comparing cases where extra artificial scattering is introduced (solid lines) against when there is no extra artificial scattering (broken lines). For extra artificial scattering scenario the M_A is varied and represented by different colors of solid line for different M_A. For each M_A, different curves of the same colour represent deviations for different μ_0.

It is seen from Fig 2.2 that pitch angle deviation are greater for the case where extra artificial scattering is introduced obviously compared to when there is no extra

artificial scattering introduced. For the case when artificial scattering is introduced the pitch angle deviation increases upon increasing the M_A of turbulence. For each M_A as the initial pitch angle increases the pitch angle deviation also increases.

Scattering in various MHD modes

"The pitch angle diffusion coefficients and their variation with initial pitch angle cosines is presented in Fig 2.3 for the three MHD modes: Alfvén, slow and fast". In this case, there are no artificial scattering introduced.

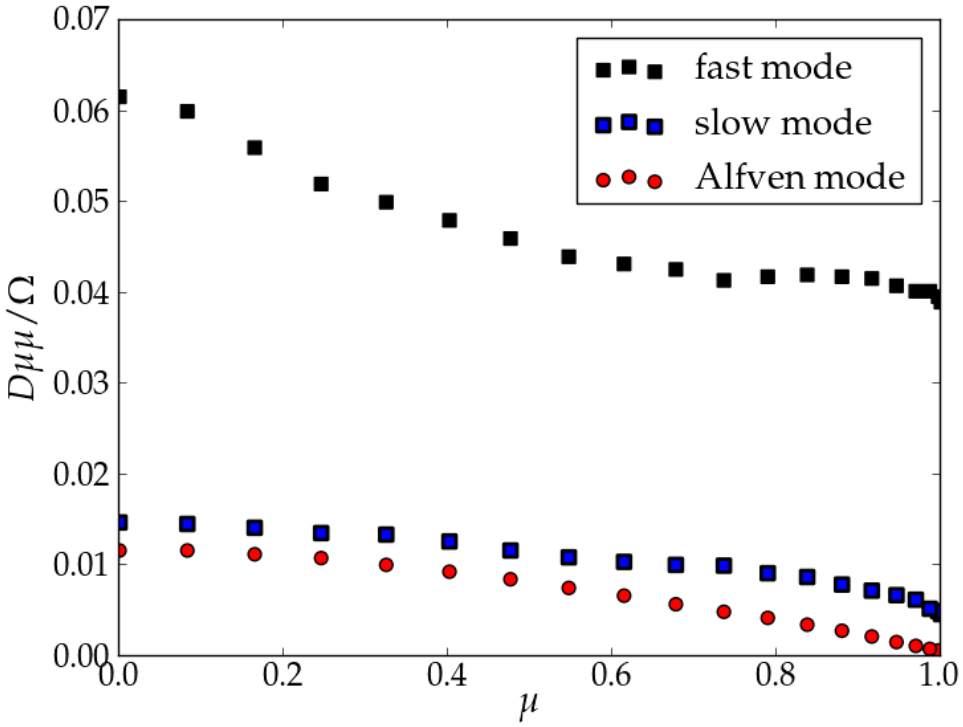

Figure 2.3: Pitch angle diffusion coefficients for CRs in different MHD modes with $M_A \sim 0.9$. The x axis represents the initial pitch angle cosine, μ. The y axis represents the pitch angle scattering coefficient normalised by the gyrofrequency, $D_{\mu\mu}/\Omega$. Different symbols represent different MHD modes: Alfvén (red), slow (blue) and fast (green).

"The result agrees well with the prediction of the nonlinear theory in Yan, Lazarian, 2008 (H. Yan and Lazarian 2008). Compressible modes contribute to particle scattering through both gyroresonance and resonant mirror (transit time damping, TTD)

interaction, the latter of which only operates with compressible modes. Alfvén modes, on the other hand, only scatter particles through gyroresonance. This is why slow modes are slightly more efficient in scattering particles despite that they have the similar anisotropy as Alfvén. In comparison to the anisotropic Alfvén and slow modes, the scattering with the isotropic fast modes are more efficient. It should be noted that the inertial range in the current MHD simulations is limited. The interstellar turbulence cascade spans more than 10 decades (Armstrong et al. 1995; Chepurnov and Lazarian 2010). CRs experience, therefore, much more anisotropic Alfvénic turbulence on the resonant scales, which are 6-7 orders of magnitude smaller than the turbulence injection scale ($\sim 100pc$) in interstellar medium. This indicates the role of fast modes in scattering CRs is even more prominent in the Galactic ISM".

Mean free path calculation

"The pitch-angle scattering determines the diffusion of CRs parallel to the magnetic field. By inserting $D_{\mu\mu}$ from our simulation into the following equation, the parallel mean free path of CR ($\lambda_{\parallel}$) can be calculated (Earl 1974)":

$$\frac{\lambda_{\parallel}}{L} = \frac{3}{4}\int_0^1 \frac{d\mu v(1-\mu^2)^2}{D_{\mu\mu}L} \tag{2.24}$$

The parallel mean free paths obtained from the pitch angle scattering coefficients for various M_A are presented in Table 2.3.

M_A	0.68	0.73	0.8	0.91
$\lambda_{\parallel}$	2.5	2.1	1.4	0.9

Table 2.3: The obtained mean free path from the pitch angle diffusion coefficients is listed in the table. It is seen that the mean free path obtained from pitch angle scattering diffusion coefficients where no extra artificial scattering is introduced has values greater than the injection length L of MHD turbulence.

"This calculation will be further cross-checked with the parallel diffusion discussed in the next section".

2.4.2 Pitch angle scattering vs particle energy

The dependence of pitch angle scattering or pitch angle diffusion coefficient on the energy or gyroradius r_L of CR as it propagates through various MHD modes in MHD turbulence with $M_A \sim 0.9$ is presented in Fig 2.4.

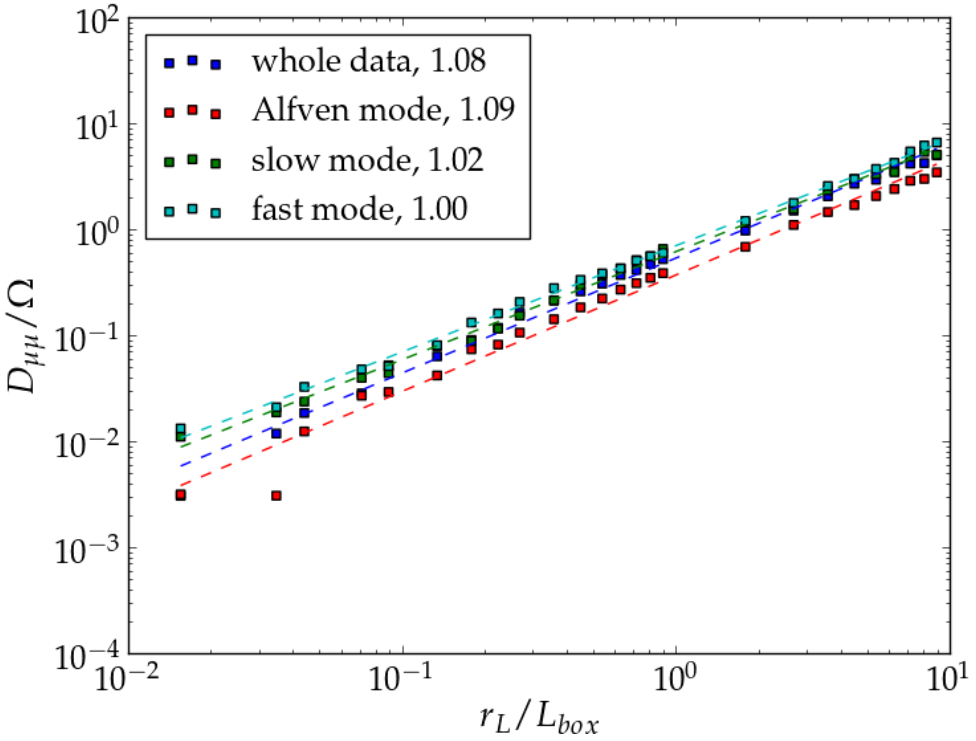

Figure 2.4: Pitch angle diffusion coefficients for CRs in different MHD modes with $M_A \sim 0.9$. The x axis represents the gyroradius r_L or the energy of the particles. The y axis represents the pitch angle scattering coefficient normalised by the gyrofrequency, $D_{\mu\mu}/\Omega$. Different symbols represent different MHD modes: Alfvén (red), slow (blue) and fast (green).

It is seen from Fig 2.4 that the scattering frequency normalized to the gyration frequency is proportional to the Larmor radius i.e. it is constant with energy as $\Omega r_L = v \approx c$. The same results have been obtained in (Beresnyak et al. 2011) earlier. However it was reported from their numerical simulations that at larger energies scattering becomes less efficient which they attributed to experiencing less mirror force at high energies. This transition occurred at at around $r_L/L \approx 0.1$. The MHD turbulence they studied were incompressible in nature. The results from the current

simulations in compressible MHD does not show such lowered scattering effects or transition around $r_L/L \approx 0.1$.

2.5 CR spatial diffusion

"Cosmic rays have varied mean free paths ($\lambda_{\parallel}$) depending on different astrophysical scenarios through which they are travelling. Ultra high energy cosmic rays (UHECR) and high energy galactic cosmic rays (GCR) in molecular clouds or interplanetary turbulent medium have mean free path greater than the energy injection scale of MHD turbulence in the medium ie $\lambda_{\parallel} > L$. On the other hand the mean free path for most galactic cosmic rays are smaller than the energy injection scale in the turbulent medium ie $\lambda_{\parallel} < L$. In this study both these scenarios are explored with mean free path of cosmic rays greater and less than the energy injection scale".

"The CR spatial diffusion is strongly dependent on the transportation scale, i.e., larger or smaller than the magnetic coherence length of the turbulence (at the injection scale L for the current simulations). Hence, the calculations will be separated for the two cases and presented in the next two subsections."

2.5.1 CR transport on large scales

The results from numerical simulations carried out to study CR transport in large scale eddies of MHD turbulence is presented here. The $\lambda_{\parallel}$ of cosmic rays is varied in the current simulations for $\lambda_{\parallel} > L$ and $\lambda_{\parallel} < L$. Whereas earlier simulation (Xu and Huirong Yan 2013) studied only $\lambda_{\parallel} > L$ case, the $\lambda_{\parallel} < L$ is presented here for the first time. Additionally, we extend the study of the earlier simulations from sub-Alfvénic to super-Alfvénic turbulence for the first time. Most importantly the numerical simulations of CR transport are carried out in different decomposed modes in MHD turbulence namely the Alfvén, slow and fast mode in addition to the total mixed mode of MHD turbulence for the first time. Earlier simulations of CR transport were carried out in the total data cube which was solenoidally driven and contained a mix of all MHD modes and were not decomposed into individual MHD modes. The diffusion coefficients are calculated for CR transport in different scenarios not only in the global frame of reference but also in the local frame of reference from where mean free path of CR can be calculated. Earlier studies used the global frame of reference only for calculation of diffusion coefficients (Xu and Huirong Yan 2013).

Description of simulation setup

"Two thousand particles are used for each of the current simulation of CR transport in MHD turbulence data cubes of varying M_A". Earlier simulations (Xu and Huirong Yan 2013) used a thousand particles for calculations of diffusion coefficients in large scale eddies. "The initial position and initial pitch angles for CRs are set as random with large scale transport. The simulations are run in total turbulence and decomposed MHD modes with different Alfvénic Mach numbers. The simulations are carried out for thousands of particle gyro periods until a normal diffusion regime is reached".

The evolution of the particle trajectories and the corresponding magnetic fields are noted down. The spatial diffusion coefficients can be calculated from this data in both directions perpendicular and parallel to the mean magnetic field. The diffusion coefficients for CR transport can be calculated in both the global and local frame of reference. In the global frame of reference the mean magnetic field direction is considered whereas in the local frame of reference the local magnetic field direction is considered. Compared to earlier studies where diffusion coefficients were calculated only in the global frame of reference, the current study extends the calculations to the local frame of reference. The calculation of mean free path from the parallel diffusion coefficients should be in the local frame of reference.

Calculation of diffusion coefficients

The diffusion coefficient calculated in the global frame of reference is presented here. The position vector is given by $\vec{R}(x, y, z)$ and the corresponding magnetic field vector is $\vec{B}(Bx, By, Bz)$. The direction vector along the magnetic field line vector $\vec{B}$ is denoted by $\vec{b}$. The distanced travelled by particles along the magnetic field direction is considered as the parallel direction and denoted by $d_{\parallel}$.

$$d_{\parallel} = \vec{R} \cdot \vec{b} \tag{2.25}$$

The distance travelled by particles across the magnetic field direction is considered as the perpendicular direction and is denoted by $d_{\perp}$.

$$d_{\perp} = \sqrt{(x^2 + y^2 + z^2) - d_{\parallel}^2} \tag{2.26}$$

The parallel diffusion coefficient ($D_{\parallel}$) is calculated as,

$$D_{\parallel} =< \frac{(d_{\parallel} - d_{\parallel 0})^2}{2t} > \tag{2.27}$$

The perpendicular diffusion coefficient ($D_{\perp}$) is calculated as,

$$D_{\perp} =< \frac{(d_{\perp} - d_{\perp 0})^2}{2t} > \tag{2.28}$$

In the local frame of reference the $\vec{b}$ is in the direction of the turbulent field lines and in the global frame of reference the $\vec{b}$ is in the direction of the mean magnetic field line which in the current simulations is in the x direction. In global frame of reference the "diffusion coefficients reduces to,

$$D_{\perp} =< \frac{(y - y_0)^2 + (z - z_0)^2}{2t} > \tag{2.29}$$

The parallel diffusion coefficient ($D_{\parallel}$) is calculated as:

$$D_{\parallel} =< \frac{(x - x_0)^2}{2t} > \tag{2.30}$$

The parallel mean free path of particles $\lambda_{\parallel}$ is related to $D_{\parallel}$ by,

$$\lambda_{\parallel} = 3D_{\parallel}/v \tag{2.31}$$

The $\lambda_{\parallel}$ calculated this way is comparable to those obtained from $D_{\mu\mu}$ in Eq. 2.24. The mean free path in the simulations is large, $\lambda_{\parallel} > L$, due to the limited numerical resolution and therefore limited inertial range. The regime $\lambda_{\parallel} > L$ corresponds to the transport of ultra high energy CRs and high energy Galactic CRs in molecular clouds. On the other hand, the mean free path for most Galactic CRs is smaller than the energy injection scale ($\lambda_{\parallel} < L$). In order to study this regime, more scatterings are artificially introduced in the test particle simulations. In each time step of particle motion, the pitch angle scattering is artificially boosted by a constant factor to bring the mean free path below the injection length of turbulence. The higher the boosting factor is, the less is the mean free path obtained for the particles".

Diffusion on global scales for $\lambda_{\parallel} > L$

"In this section, the calculations for the diffusion of CRs on large scales beyond the inertial range are presented. As demonstrated by the simulation, the ensemble-

averaged square distance of the particles should exhibit linear growth over time, i.e., normal diffusion. Fig 2.5 demonstrates the parallel and perpendicular distance for CR propagation in sub-/super-Alfvénic turbulence. The particle running is in the regime where the mean free path is greater than the energy injection scale".

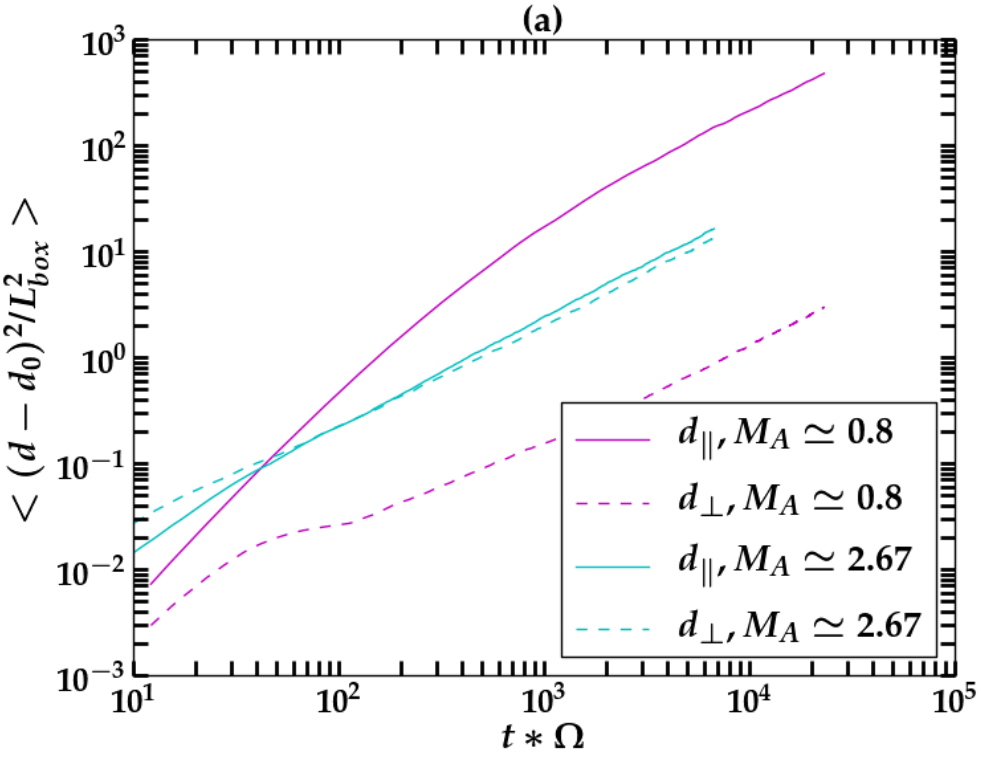

Figure 2.5: Mean square distance traveled by the particles vs. time. Both sub-Alfvénic ($M_A = 0.8$, magenta) and super-Alfvénic ($M_A = 2.67$, cyan) turbulence are presented. The y axis represents the mean square distance $< (d - d_0) >^2$ of CR transport normalised by the box length, L_{box}^2. The particle running is in the $\lambda_{\parallel} > L$ regime. The x axis represents the gyro periods $t * \Omega$. The parallel and perpendicular distances obtained from numerical simulations are represented by bold and dashed line, respectively. The particles have shown normal-diffusion. The diffusion becomes isotropic in the super-Alfvénic turbulence.

"It is noted that in Fig 2.5, the parallel diffusion is much larger than the perpendicular diffusion for $M_A = 0.8$ but they are equal to each other for $M_A = 2.67$. This difference demonstrates the anisotropy presented in sub-Alfvénic turbulence but the super-Alfvénic turbulence is almost isotropic".

Diffusion on global scales for $\lambda_{\parallel} > L$ and M_A dependence

"The dependence of the perpendicular diffusion coefficient on Mach number is presented in Fig. 2.6 for both total turbulence data cubes and the Alfvén modes".

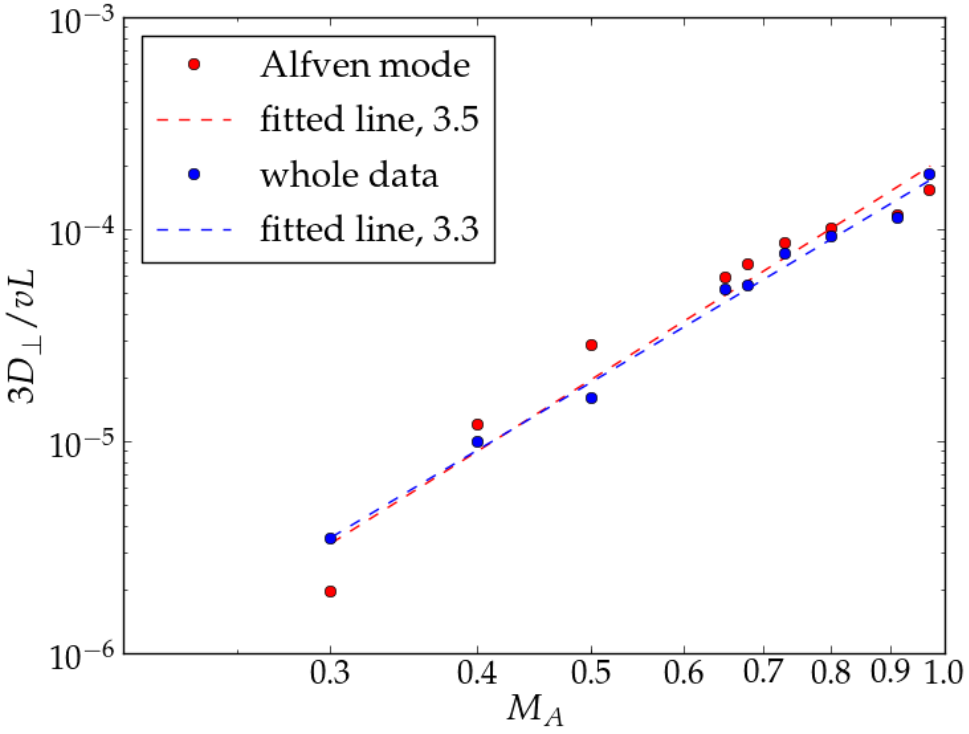

Figure 2.6: The perpendicular diffusion coefficient with $\lambda_{\parallel} > L$ in MHD turbulence of various M_A. The results are obtained for the Alfvén and the whole turbulence data cubes.

"The relation between the diffusion coefficients and Alfvénic Mach numbers is fitted by a power-law:$D_\perp \propto M_A^\zeta$. By taking into account the anisotropy of the Alfvénic turbulence, (H. Yan and Lazarian 2008) demonstrated that the relation between perpendicular diffusion $D_\perp$ and M_A should have the power-law index $\zeta = 4$ instead of the $\alpha = 2$ scaling calculated by (Kóta and Jokipii 2000). As is demonstrated by Fig 2.6, the index ζ is 3.5 for Alfvén modes and 3.3 for total turbulence data, respectively. Both results are more in favor of the YL08 calculation".

Diffusion on global scales for $\lambda_{\parallel} < L$

"CR propagation with mean free path smaller than the injection scale, is further considered which is the case for all Galactic CRs. Simulations are executed with the artificial scattering included as aforementioned".

"Fig 2.7 compares the ensemble-averaged square distance of the particles when the mean free path is greater or smaller than the injection scale. In this regime, all the current simulations have made sure that the running time is sufficient and normal diffusion is observed. The ensemble-averaged square distance of the particles should exhibit linear growth over time, i.e., normal diffusion".

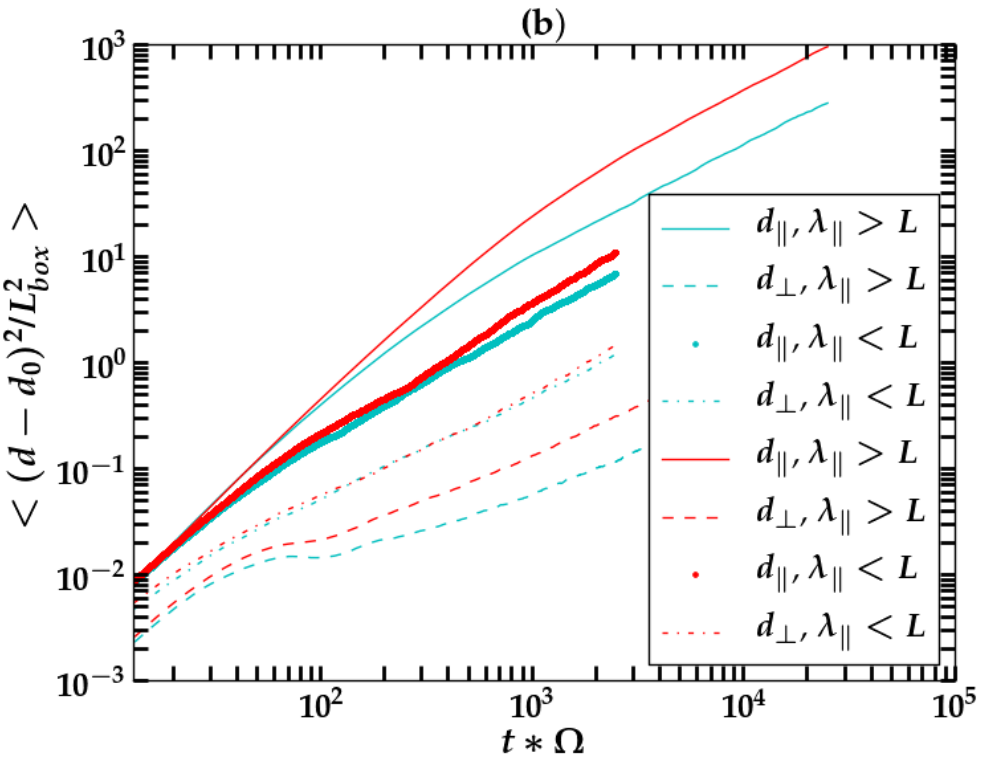

Figure 2.7: The same as Fig. 2.5 but for both CRs with $\lambda_{\parallel} > L$ and with $\lambda_{\parallel} < L$ in total turbulence data and Alfvén modes with M_A =0.73. After introducing artificial scattering, the transport becomes more isotropic compared to no artificial scattering.

"To perform parallel and perpendicular diffusion coefficients, the range when the linear growth is observed in the time evolution figure is considered. In this regime,

it is expected that the ratio between perpendicular and parallel diffusion coefficients ($D_\perp/D_\parallel$) will follow an M_A^4 dependence (H. Yan and Lazarian 2008). The dependency of the diffusion coefficients on Mach numbers is presented in Fig 2.8 for $\lambda_\parallel < L$. The diffusion coefficients are compared for both the Alfvén modes and the total turbulence".

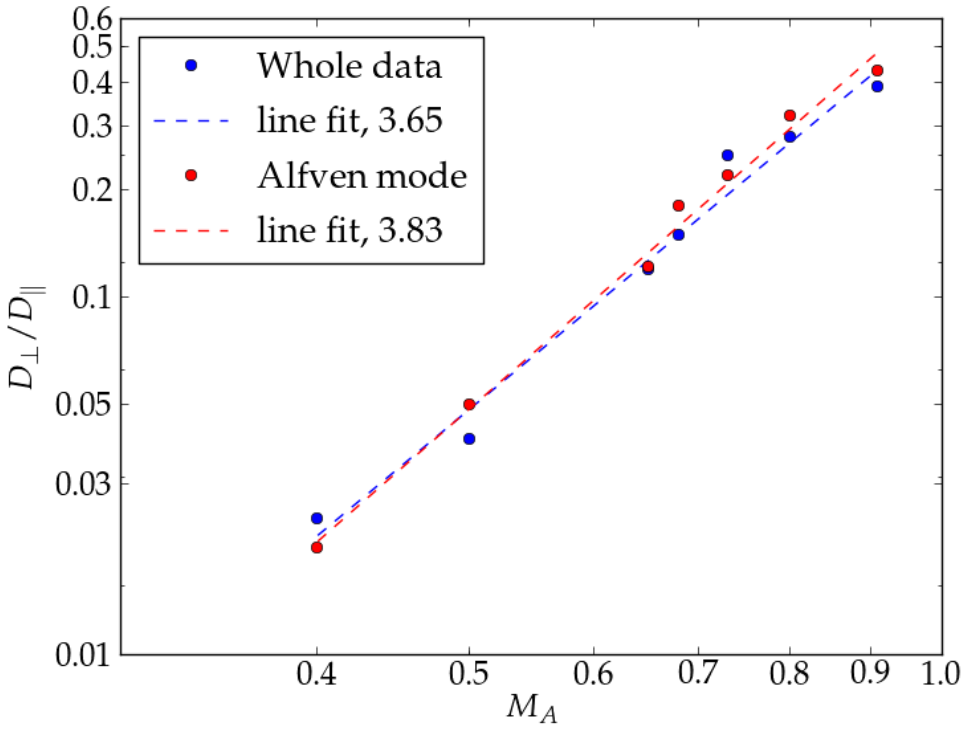

Figure 2.8: The ratio between perpendicular and parallel diffusion ($D_\perp/D_\parallel$) when $\lambda_\parallel < L$. Transport of particles in both the whole turbulence (blue) and Alfv́en modes (red) are presented. The fitting lines and power-law indices are marked in the legend.

"As demonstrated in Fig 2.8, the fitting index is 3.65 for the total turbulence data cubes and 3.83 for Alfvén modes".

"For both regimes where the CR mean free path is larger and smaller than the injection scale, the results from Alfvén modes are closer to the expected index $\zeta = 4$ (YL08) than those from total turbulence data cubes. This is due to the contributions from the magnetosonic modes in the total turbulence data cubes. The current calculations show that the CR perpendicular diffusion on large scale is

strongly dependent on the Alfvénic Mach number, and it is essential to consider the anisotropy of MHD turbulence when modelling CR propagation".

Diffusion coefficient for CR transport on local scales and mean free path calculation

In this section, the calculations for the diffusion of CRs on large scales in the local frame of reference are presented. As demonstrated by the simulation, the ensemble-averaged square distance of the particles should exhibit linear growth over time, i.e., normal diffusion. Fig 2.9 demonstrates and compares the parallel and perpendicular distance for CR propagation in both the global and local frame of reference for $M_A = 0.8$.

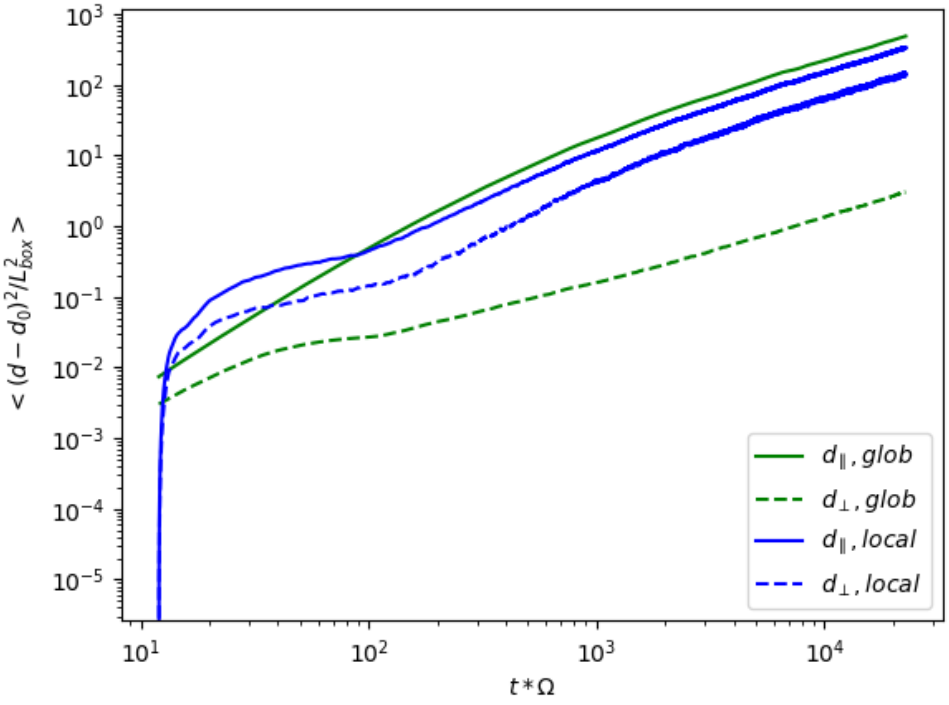

Figure 2.9: Mean square distance traveled by the particles vs. time in sub-Alfvénic ($M_A = 0.8$) turbulence in both global and local reference frame are presented. The particle running is in the $\lambda_{\parallel} > L$ regime. The parallel and perpendicular distances obtained from numerical simulations are represented by bold and dashed line respectively.

The anisotropy in diffusion reduces when calculations are made in the local frame of reference. In this frame the parallel diffusion reduces a bit and perpendicular diffusion increases.

The parallel mean free path of particles $\lambda_{\parallel}$ is related to $D_{\parallel}$ by $\lambda_{\parallel} = 3D_{\parallel}/v$. The parallel mean free path is obtained from both the global and local frame of reference and compared with the mean free paths obtained from the pitch angle scattering coefficients and presented in Table2.4.

M_A	0.68	0.73	0.8	0.91
Global, (from $D_{\parallel}$)	5.4	3.5	1.9	1.2
Local, (from $D_{\parallel}$)	4	2.6	1.5	0.8
Local, (from $D_{\mu\mu}$)	2.5	2.1	1.4	0.9

Table 2.4: The obtained mean free path from the diffusion coefficients is listed in the table. The mean free path obtained from the spatial diffusion coefficients are calculated and compared in both the global and local frames of reference. The mean free path is also calculated from pitch angle diffusion coefficient and compared with the above. It is seen that the mean free path obtained from pitch angle scattering coefficient is closer to mean free path obtained from spatial diffusion coefficient in the local frame of reference.

It is found out that the mean free path calculated from parallel spatial diffusion coefficient, $D_{\parallel}$ in the local frame of reference is closer to the mean free path calculated from the pitch angle diffusion coefficient, $D_{\mu\mu}$ which is in the local frame of reference.

2.5.2 Perpendicular Transport on small scales

"In this section, the particle transport on small scales is discussed within the inertial range. The time evolution for the perpendicular transport can be fitted by a power-law:

$$d_{\perp} \equiv < (y - y_0)^2 + (z - z_0)^2 >^{1/2} \propto t^{\alpha} \tag{2.32}$$

Richardson diffusion

The Richardson diffusion describes the explosive growth of the separation of particles in turbulence medium, as inferred from fluids experiments many decades ago (Richardson 1926). Richardson law is equivalent to the Kolmogorov spectrum. Therefore Richardson diffusion is also expected in MHD turbulence since the perpendicular spectrum of Alfvénic turbulence has a Kolmogorov scaling (P. Goldreich and Sridhar 1995). The Richardson diffusion in MHD turbulence was confirmed with high resolution numerical simulations by (Eyink et al. 2013). Following the Richardson diffusion of magnetic field lines, CRs also undergo superdiffusion on the scales below the injection scale with the index over time $\alpha = 3/2$ (Lazarian and Yan 2014; H. Yan and Lazarian 2008)".

Description of Simulation setup for CR perpendicular diffusion calculation

" For the study of CR transport on small scales, test particle simulations are performed in MHD turbulence data cubes with CRs being initially grouped together into beams. The simulation box has 512^3 cells. This box is divided into 64 equally sized cubes of size 128^3 cells. From the center of each of these cubes, a beam is launched parallel to the local magnetic field. The starting points of the beam particles are uniformly distributed around the center of each cube with a separation of 1 cell unit among them. The CRs in each beam are very closely spaced and their initial pitch angles are set at zero so that it could be analyzed how the particle separation diverges with time. For a particular Mach number, the test particle simulations are done in different MHD modes as well as the total turbulence data cubes. There are two reference frames in the current simulations: the global reference frame, defined by the mean magnetic field of the turbulence data cube, and the local reference frame, defined by the mean magnetic field along the particle trajectory. The evolution of perpendicular CR transport in this work is calculated in both the global and the local frames of reference. The particle position, velocity and the magnetic field at the corresponding position are recorded at each time instance from test particle simulations. The values of the perpendicular distance is obtained by averaging over all combinations of pairs of particles within individual beams and then over all the beams." The calculations of the perpendicular distance in the local reference frame is carried out in two different ways by considering the local magnetic field in two different ways that is explained below.

Description of calculation of perpendicular distance

Let us consider a pair of particles within a beam. Let particle 1 has position vector $\vec{R_1}(x, y, z)$ and corresponding magnetic field $\vec{B_1}(x, y, z)$ and particle 2 has position vector $\vec{R_2}(x, y, z)$ and corresponding magnetic field $\vec{B_2}(x, y, z)$. The direction vector along the magnetic field line vector $\vec{B_1}$ is denoted by $\vec{b_1}$ and along the magnetic field line vector $\vec{B_2}$ is denoted by $\vec{b_2}$. The average local magnetic field direction of the two particles is given by,

$$\vec{b} = \frac{(\vec{b_1} + \vec{b_2})}{2} \tag{2.33}$$

The average local magnetic field direction can also be considered for all the particles in a beam where n denotes the number of particles in a beam.

$$\vec{b} = \frac{(\vec{b_1} + \vec{b_2} + \vec{b_3} + ... + \vec{b_n})}{n} \tag{2.34}$$

The separation distance vector $\vec{dr}$ between the pair of particle is given by,

$$\vec{dr} = \vec{R_1} - \vec{R_2} \tag{2.35}$$

The parallel separation distance between a pair of particle is given by,

$$d_{\parallel} = \vec{dr} \cdot \vec{b} \tag{2.36}$$

The parallel separation vector can be calculated in the global frame of reference where the magnetic field direction is considered as the mean magnetic field direction. The parallel separation vector can be calculated in the local frame of reference where the magnetic field direction is considered as the local fluctuating magnetic field direction. As mentioned above, the particle separation is recorded for all combinations of pairs of particles within a beam. Eqn 2.36 can be calculated for each pair of particle considering average of the local magnetic field of the pair of particles using Eqn 2.33. Eqn 2.36 can also be calculated for each pair of particle considering average of the local magnetic field of all the particles in a beam using Eqn 2.34.

The perpendicular separation distance between the pair of particle is given by,

$$d_{\perp} = \sqrt{dr^2 - d_{\parallel}^2} \tag{2.37}$$

These distances for all combinations of particles in a beam is averaged. Finally the separation distance is averaged for all beams considered in the simulation.

Comparison of different methods for perpendicular distance calculation

The perpendicular distance $d_\perp$ is plotted against the propagation time of the CRs in Fig. 2.10 from both the methods described above.

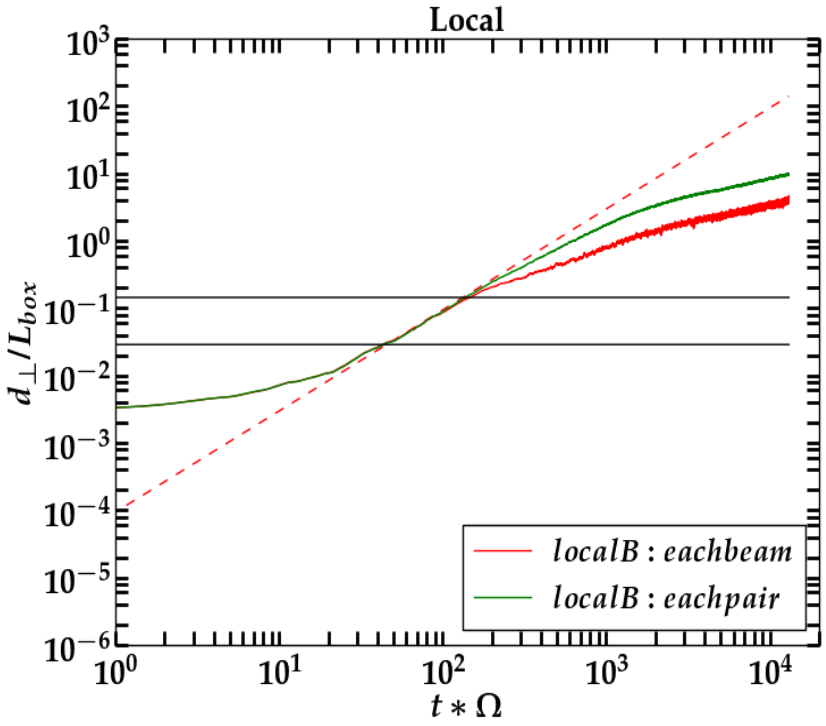

Figure 2.10: Perpendicular transport of CRs on small scales. The y axis represents the perpendicular distances normalised by the box length ($d_\perp/L_{box}$) and the x axis represents the CR gyro periods ($t * \Omega$). The perpendicular distances obtained from numerical simulations in local reference frame are represented via method 1 (green lines) and method 2 (red lines). The horizontal lines in the plots represents the inertial range of turbulence. The red dashed lines represents the reference line for super diffusion with a slope of 1.5.

It is seen from Fig 2.10 that following both the above methods of calculating perpendicular separation in the local frame of reference, the results are indistinguishable in the inertial range. So the first method is adopted in the analysis of perpendicular transport that is present henceforth.

CR superdiffusion in CL turbulence

"The perpendicular distance $d_\perp$ is plotted against the propagation time of the CRs in Fig. 2.11 for sub-Alfvénic and super-Alfvénic total turbulence data".

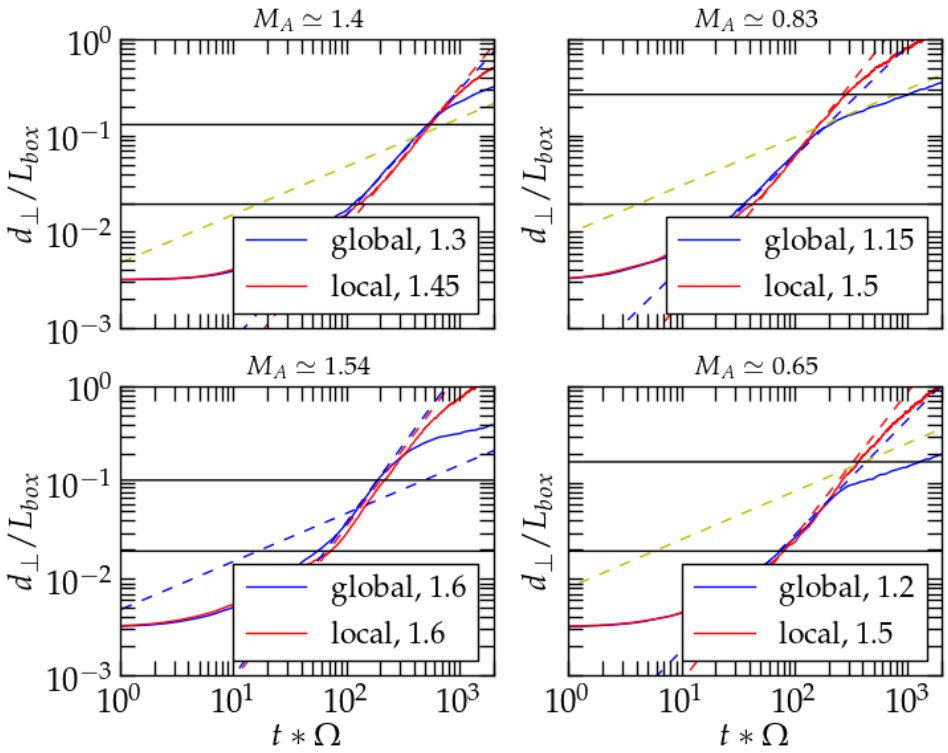

Figure 2.11: Perpendicular transport of CRs on small scales. The y axis represents the perpendicular distances normalised by the box length ($d_\perp / L_{box}$) and the x axis represents the CR gyro periods ($t * \Omega$). The perpendicular distances obtained from numerical simulations are represented in the global (blue lines) and the local (red lines) reference frame. The horizontal lines in the plots represents the inertial range of turbulence. The yellow lines represents the reference line for normal diffusion with a slope of 0.5.

"The results are fitted with Eq. (2.32). Fig 2.11 demonstrates the CR transport in the two reference frames: all cases can be fitted with the index close to $\alpha \sim 1.5$ in the *local* reference frame; whereas for global reference frame, α is only close to 1.5 at super-Alfvénic cases, decreasing substantially and close to 1 for sub-Alfvénic cases".

"In Table 2.5, the comprehensive fitting indices are listed for the CR superdiffusion in total MHD turbulence data cubes with the Alfvénic Mach number ranging from

0.44 to 1.54. The fitting index is close to Richardson-diffusion $\alpha \sim 1.5$ for all data measured in the *local* reference frame, which is in line with the theoretical expectations since the global magnetic field generally differs from local magnetic fields in turbulent medium".

M_A	0.44	0.56	0.65	0.83	1.28	1.4	1.54
Global	0.95	1.1	1.2	1.15	1.25	1.3	1.6
Local	1.3	1.45	1.5	1.5	1.35	1.45	1.7

Table 2.5: The obtained super-diffusion index α is listed in the table. The diffusion coefficients are calculated and compared in both the global and local frames of reference. CR undergo super-diffusion and the slope obtained is closer to 1.5 in the *local* reference frame.

CR superdiffusion in PENCIL turbulence

"The perpendicular transport on small scales from decomposed MHD modes is further studied. As an example, Fig. 2.12 demonstrates how the fitting index for the time evolution of the perpendicular transport in different MHD modes is obtained. Both local and global reference frames are used in the current calculations".

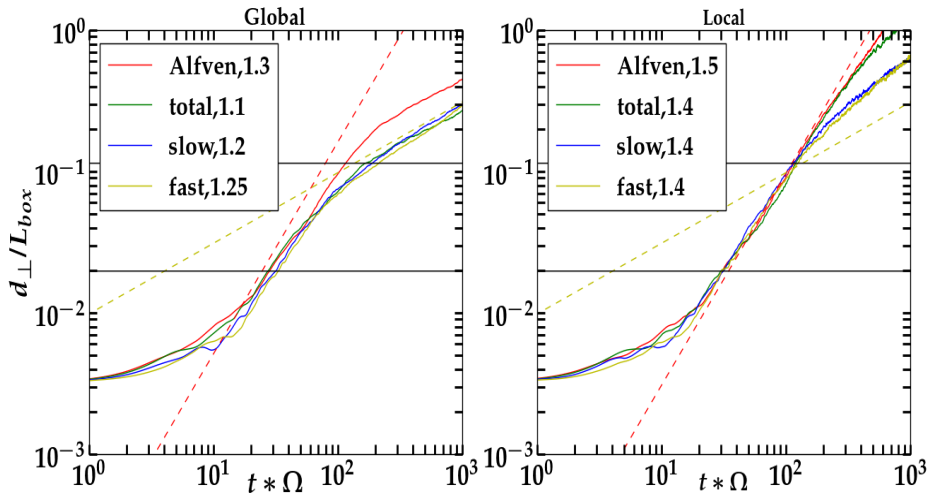

Figure 2.12: The same as Fig. 2.11, but with $M_A \sim 0.73$ and results in decomposed modes included for comparison.

"Turbulence data cubes with Alfvénic Mach numbers ranging from 0.4 to 1.0 are considered and the fitting power-law index α are presented for total and decom-

posed modes in Table 2.6. Superdiffusion is generally observed in all the current tests. From Table 2.6, it is observed that the particles in decomposed Alfvénic modes are the closest to the Richardson diffusion (index $\alpha = 1.5$) in the *local* reference frame compared to the other modes. In global magnetic reference frame, the indices deviate further from the Richardson diffusion as expected. It implies that the observed superdiffusion index can vary determined by the modes composition as well as the Alfvénic Mach number of the local turbulence".

M_A	0.4	0.5	0.65	0.68	0.73	0.8	0.91	0.97
Global MM	0.8	1.0	1.1	1.1	1.1	1.2	1.15	1.15
Global AM	1.1	1.65	1.3	1.3	1.3	1.35	1.3	1.4
Global SM	0.95	1.3	1.3	1.1	1.2	1.3	1.2	1.3
Global FM	1.1	1.2	1.1	0.9	1.25	1.25	1.6	1.4
Local MM	1.2	1.5	1.6	1.4	1.4	1.5	1.4	1.4
Local AM	1.5	1.5	1.5	1.5	1.5	1.5	1.5	1.6
Local SM	1.6	1.4	1.3	1.3	1.4	1.4	1.3	1.3
Local FM	1.55	1.7	1.1	1.3	1.4	1.4	1.7	1.4

Table 2.6: The same as Table 2.5 but the comparison extends to decomposed MHD modes. AM represents Alfvén mode, SM represents slow modes, FM represents fast mode and MM represents the total data cube. “Global” and “Local” represent the magnetic reference frame in the calculation. CR undergoes super-diffusion in decomposed Alfvénic modes and are the closest to the Richardson diffusion (index $\alpha = 1.5$) in the local reference frame compared to the other modes.

CR super-diffusion in sub-Alfvénic turbulence at higher resolution

"The perpendicular transport on small scales from decomposed MHD modes in higher resolution data cube is also presented here. The resolution of the data cube used here is 1024 compared to 512 used in our earlier simulations. The MHD turbulence data cubes used here are generated from PLUTO and compressibly driven".

Fig 2.13 demonstrates how the fitting index is obtained for the time evolution of the perpendicular transport in different MHD modes. The local reference frames are used in this calculation.

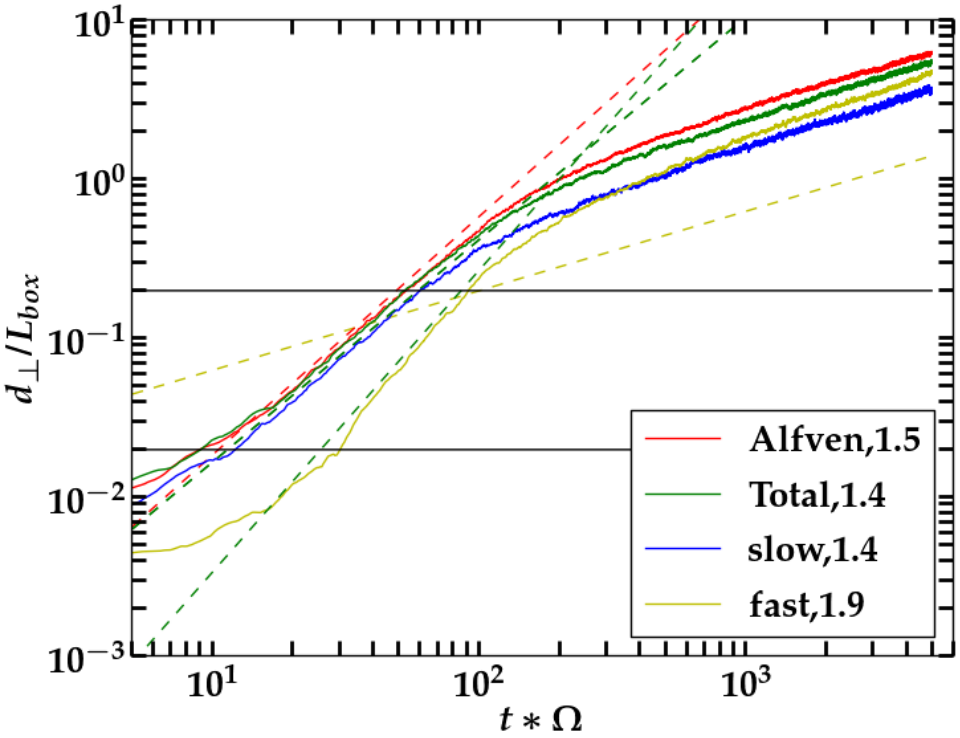

Figure 2.13: Perpendicular transport of CRs at small scales in a high resolution MHD data cube (1024). The MHD cubes are obtained from PLUTO upon being driven more compressibly and are decomposed. The turbulence has $M_A \simeq 0.86$. The y axis represents the perpendicular distances normalised by the box length $d_\perp/L_{box}$ and the x axis represents the CR gyro periods ($t * \Omega$). The perpendicular distances obtained from numerical simulations are represented in the local reference frame for the various MHD modes. The horizontal lines in the plots represents the inertial range of turbulence. The yellow lines represents the reference line for normal diffusion with a slope of 0.5.

In Fig 2.13 superdiffusion is observed in all the modes. The particles in decomposed Alfvénic modes are the closest to the Richardson diffusion (index $\alpha = 1.5$) in the *local* reference frame compared to the other modes. The fast modes has a higher index probably due formation of shocks in fast modes.

Comparison of PSD of turbulence and PDF of test particles

"Figure 2.14 shows the power spectral density (PSD) of the turbulence data and the probability density functions (PDFs) of the test particles launched in the same turbulence data cube versus the distance r between them at different time snapshots".

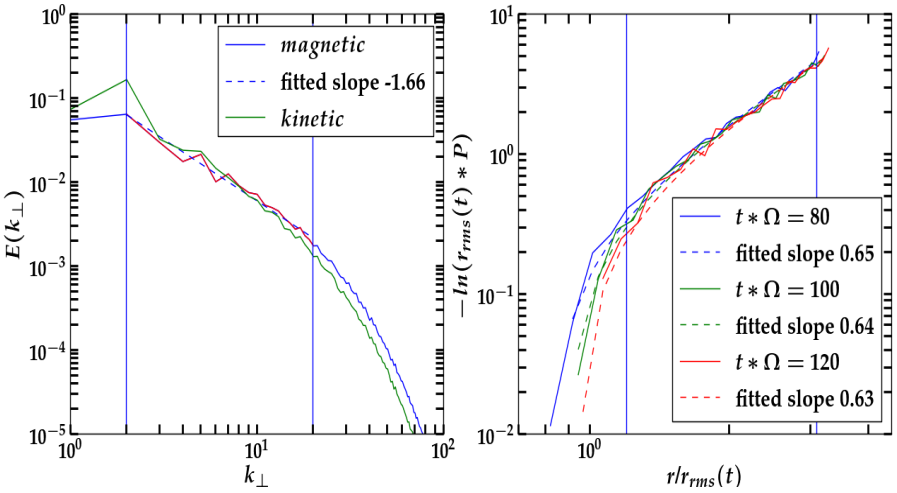

Figure 2.14: *Left) The power spectrum density of turbulence data* Right)*: The Probability distribution of test particles launched from the same turbulence data cube vs. the distance r at given time snapshots. The fitting is consistent with Kolmogorov spectrum index h=1/3.*

"The distribution fits well to an exponential form, i.e., $P \propto exp(-Cr^{(1-h)})$; the index h = 1/3 is the Kolmogorov scaling, consistent with the Richardson diffusion (Hentschel and Procaccia 1984)(Eyink et al. 2013)".

"The calculation for the M_A dependence of the super diffusion ${d_\perp}^2/t^3$ of particles on the scales smaller than the turbulence injection scale is studied next. It is expected that for sub Alfvénic turbulence the dependence is M_A^4 and for super-Alfvénic turbulence the dependence is M_A^3 (H. Yan and Lazarian 2008)(Lazarian and Yan 2014)".

CR super-diffusion in sub-Alfvénic turbulence with varied M_A

Fig. 2.15 demonstrates the CR perpendicular diffusion in Alfvén modes in sub-Alfvénic regime. The diffusion coefficients are calculated in both the local and global reference frames.

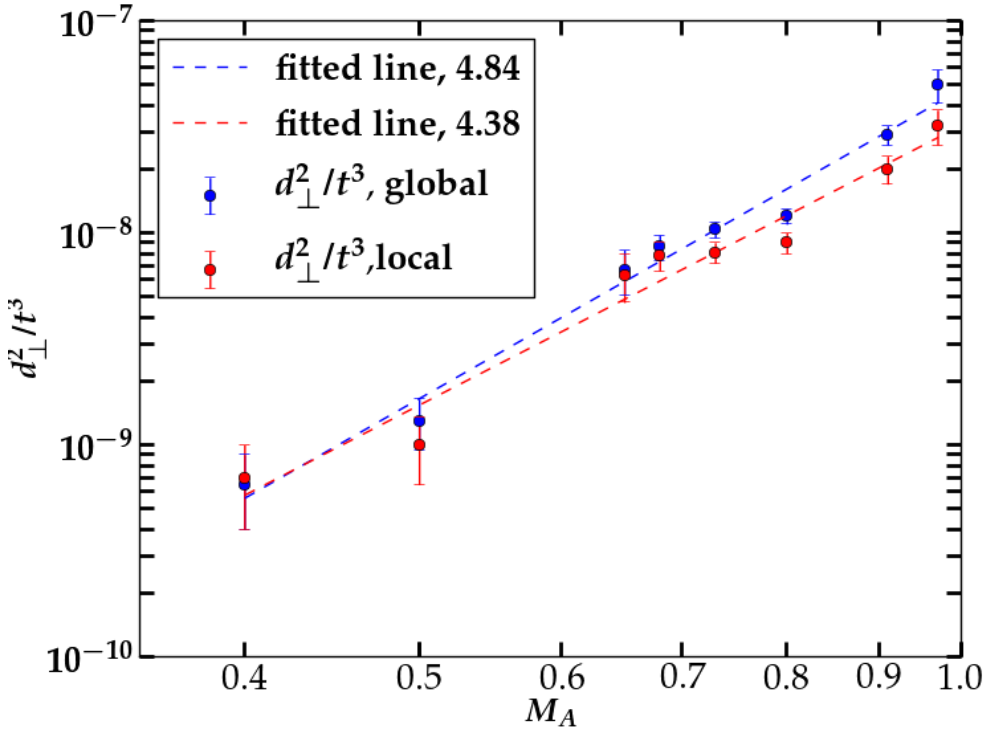

Figure 2.15: Superdiffusion of particles with $\lambda_{||} > L$ in Alfvén modes. The blue line is the fit in the global reference frame. The red line shows the fit for the data points obtained in the local reference frame.

"The fitting power-law index in the *local* reference frame (4.34) is closer to the theoretical expectation M_A^4 than that in the global frame (4.84)".

CR super-diffusion in super-Alfvénic turbulence

Fig 2.16 shows the perpendicular diffusion, $d_\perp$ evolution with time in super Alfvénic turbulence for the total data cube and decomposed MHD modes. The M_A of the turbulent data cube is 2.11. The inertial range of MHD turbulence starts from LM_A^{-3}. The MHD mode decomposition is only performed within the inertial range.

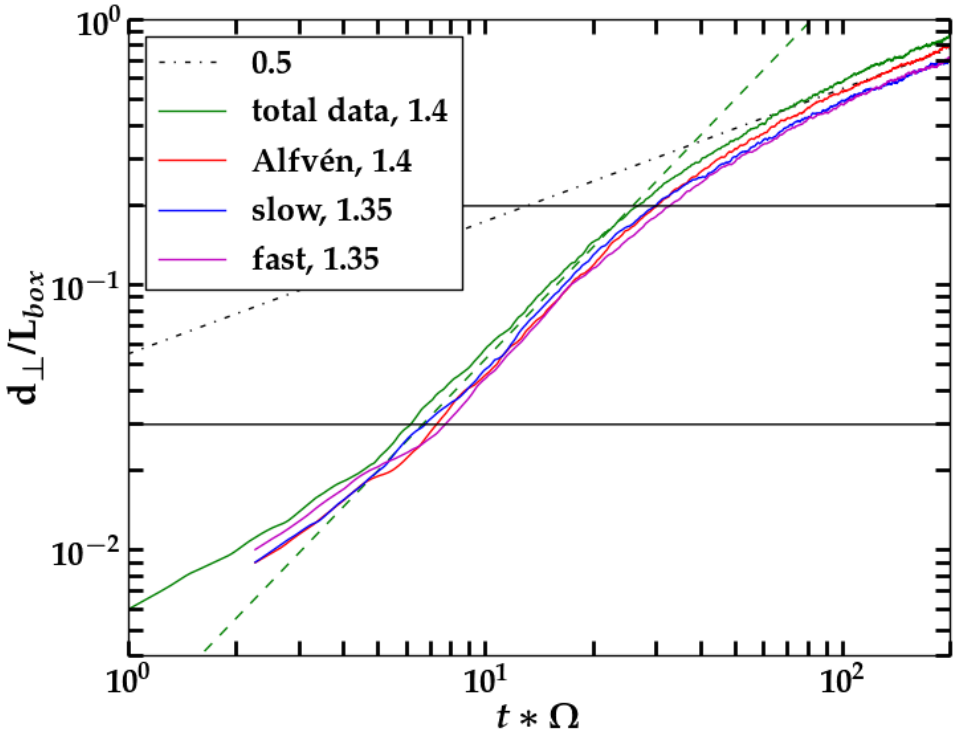

Figure 2.16: The perpendicular transport of CR in super-Alfvénic turbulence $M_A = 2.11$ and at small scales calculated in local reference frame. The turbulent data cubes used here are from PENCIL. Super-diffusion is observed in Alfvén modes with power-law index close to 1.5 within the inertial range represented by horizontal lines. The green dashed line represents the superdiffusion slope whereas the black dashed dotted line represents the normal diffusion slope.

The time evolution of perpendicular transport is fitted with Eq (2.32) when the particles are within the inertial range (indicated by black lines). The CRs in the decomposed Alfvén modes have shown the super-diffusion with power-law index 1.5. The contributions from magnetosonic modes result in the slightly different

power-law index obtained in the total turbulence data (1.4).

CR super-diffusion in super-Alfvénic turbulence with varied M_A

Fig 2.17 represents M_A dependence of the perpendicular diffusion at the *local* reference frame in different super Alfvénic turbulence.

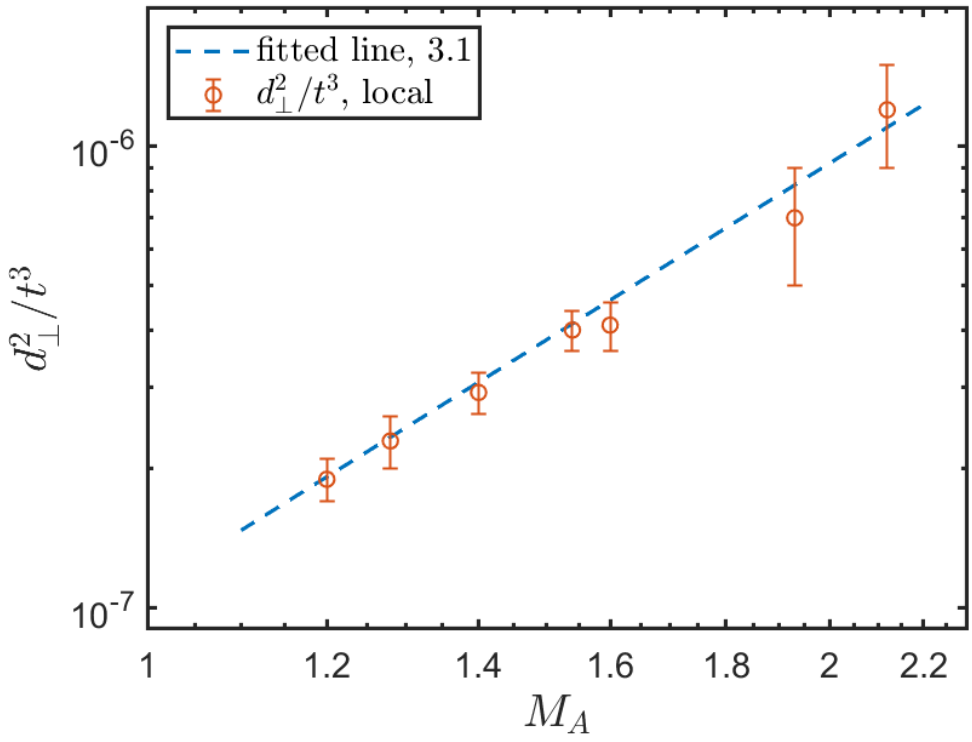

Figure 2.17: The same as Fig. 2.15, but with super-Alfvénic turbulence. The turbulent data cubes used here are from PENCIL. The calculation is done in local reference frame. The orange dots represents the values of diffusion from numerical simulations. The blue line shows the fit for the data points obtained in the local reference frame.

"The super-diffusion on small scales ${d_\perp}^2/t^3$ in the *local* reference frame show a dependence of $M_A^{3.1}$ in the current calculations, close to the M_A^3 theoretical relation".

Perpendicular diffusion of CR for $\lambda_{\parallel} < L$ and $\lambda_{\parallel} > L$

"The results from the study of the dependence of the super-diffusion on the mean free path $\lambda_{\parallel}$ of the particles is presented next." The MHD turbulence cubes used here are from PENCIL.

Fig 2.18 compares the super-diffusion of CRs with mean free path $\lambda_{\parallel}$ larger or smaller than the turbulence injection scale L, respectively.

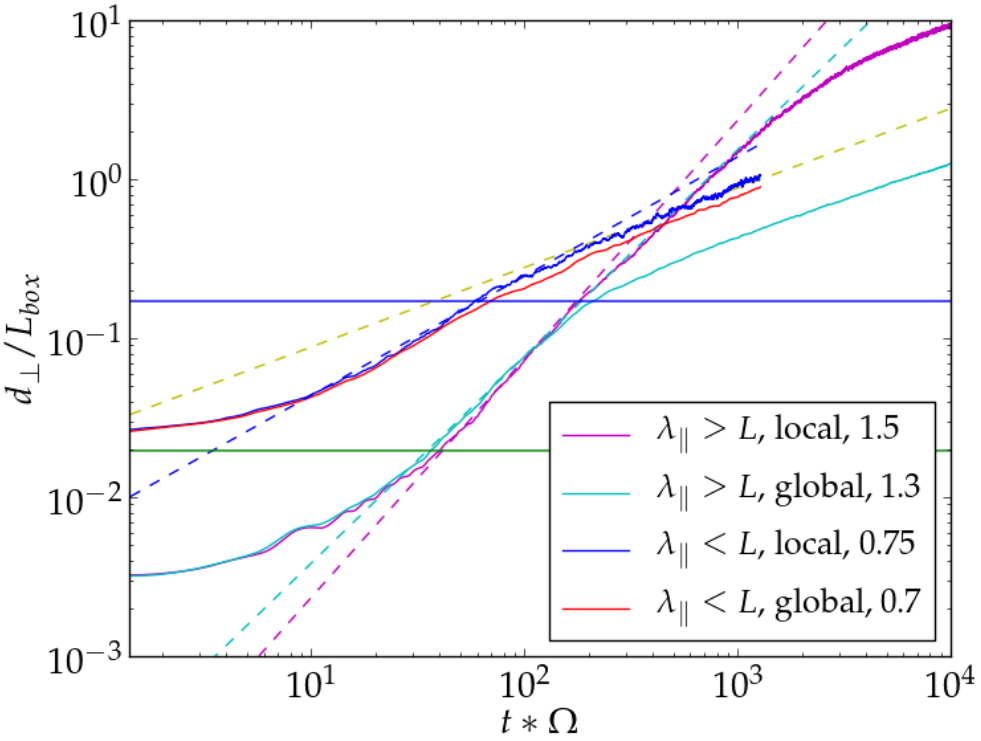

Figure 2.18: The same as Fig 2.12, but including CRs with $\lambda_{\parallel} > L$ and $\lambda_{\parallel} < L$ propagating in Alfvén modes. The fitting index is 1.5 for $\lambda_{\parallel} > L$ and 0.75 for $\lambda_{\parallel} < L$ in the *local* reference frame.

"The CR transport shows Richardson diffusion in the *local* reference frame, i.e., with an power-law index of 1.5 when $\lambda_{\parallel} > L$ and reduced to 0.75 when $\lambda_{\parallel} < L$, in line with the theoretical expectation. The mean free path is reduced by introducing more artificial scattering in simulations and the super-diffusion index reduces

tending towards normal diffusion as artificial scattering is increased more."

Particle trajectories of CR for $\lambda_{\parallel} < L$ and $\lambda_{\parallel} > L$

"The 3D trajectories of the particles in the MHD turbulence data are presented in Fig 2.19."

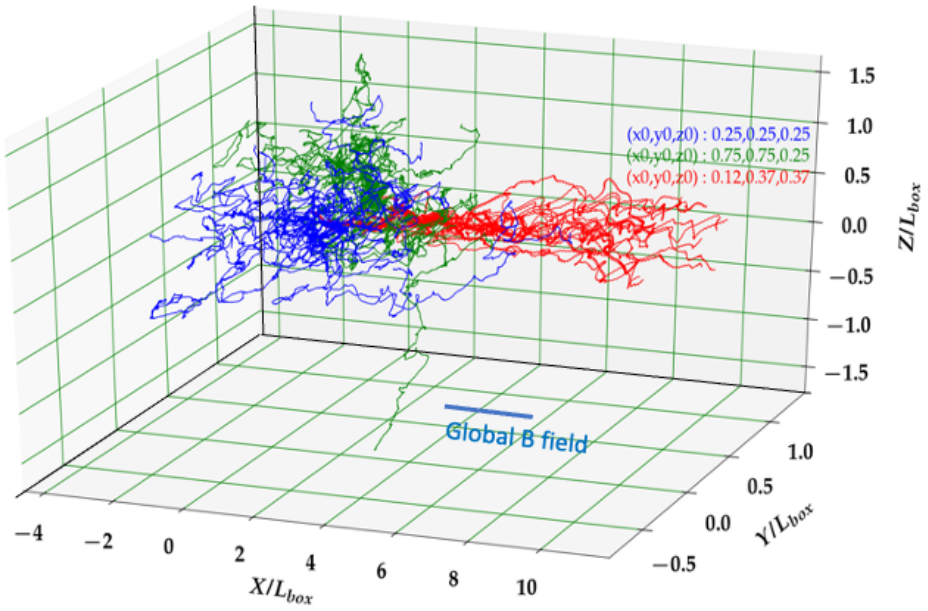

Figure 2.19: 3D trajectories of particles launched from a beam. They experience superdiffusion because of Richardson diffusion of magnetic fields in turbulence. The rate of superdiffusivity, the α index, depends on the ratio of mean free path to the injection scale. See also Fig 2.20.

"Three beams are launched from three randomly selected positions. The (red) beam with larger mean free path ($\lambda_{\parallel} \simeq 15L$) exhibits superdiffusion guided by magnetic field lines. In contrast to hydrodynamic system, the spread is substantially smaller, consistent with earlier study (Eyink et al. 2013). On the other hand, the (green) beam launched with mean free path ($\lambda_{\parallel} \simeq 0.9L$) displays more stochasticity, in line with diffusion/random walk process. The blue beam has an intermediate mean free

path ($\lambda_{||} \simeq 1.5L$) and shows a characteristics in between."

Diffusion index variation with varying $\lambda_{||}$

"Fig 2.20 displays the diffusion index α of CRs as a function of mean free path $\lambda_{||}$ in the *local* reference frame."

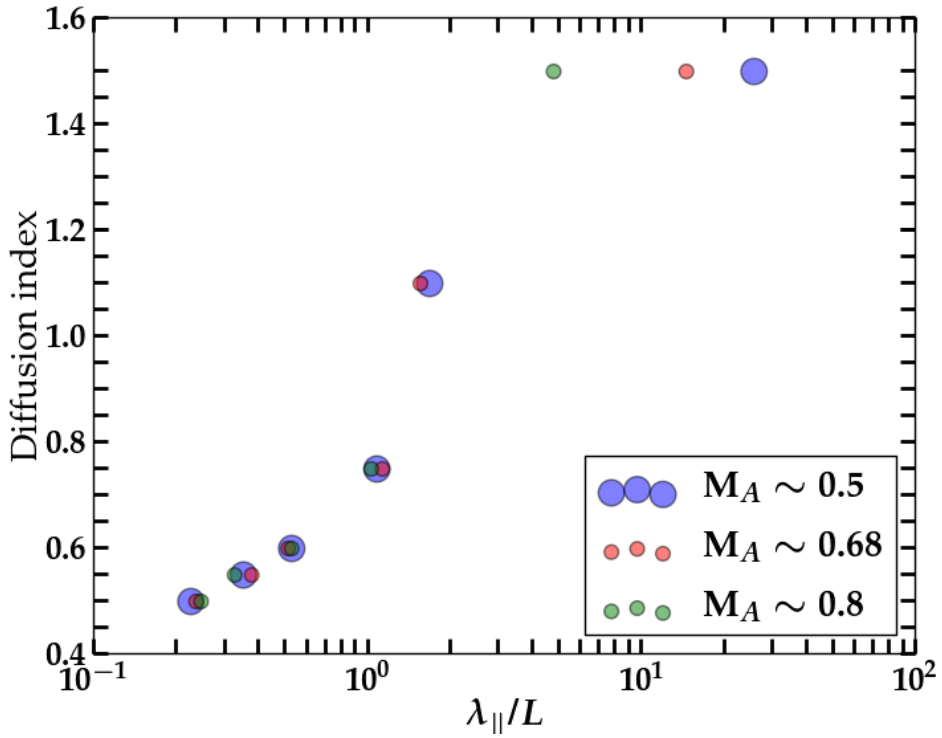

Figure 2.20: The diffusion index α vs. $\lambda_{||}$ in the *local* reference frame. The diffusion index changes smoothly from 0.5 corresponding to the normal diffusion regime in the case of $\lambda_{||}/L \ll 1$ to 1.5 when $\lambda_{||}/L \gg 1$ in correspondence to Richardson diffusion.

From Fig 2.20 it is seen that the diffusion index is dictated by the ratio of $\lambda_{||}$ to the injection scale L. It changes smoothly from 0.5 corresponding to the normal diffusion regime in the case of $\lambda_{||}/L \ll 1$ to 1.5 when $\lambda_{||}/L \gg 1$ in correspondence to Richardson diffusion. For $\lambda_{||}/L \gg 1$, CRs undergo a streaming motion along magnetic fields and their diffusion perpendicular to mean magnetic field is determined by the divergence of magnetic field lines. The cosmic ray trajectories trace magnetic field lines and therefore the divergence of CR trajectories is identical to that of

magnetic field. Richardson diffusion of CR is obtained in small scale sub-Alfvénic turbulence. With reduced mean free path, CR undergo reduced super-diffusion until a normal diffusion regime is reached. Particularly the super-diffusion becomes 0.75 when $\lambda_{||} \sim L$.

PDF of particles with varying $\lambda_{||}$

Fig 2.21 compares the probability density functions (PDFs) of the test particles versus the distance r between them at different time snapshots as shown in Fig 2.14 for both the case where mfp is greater than and less than L.

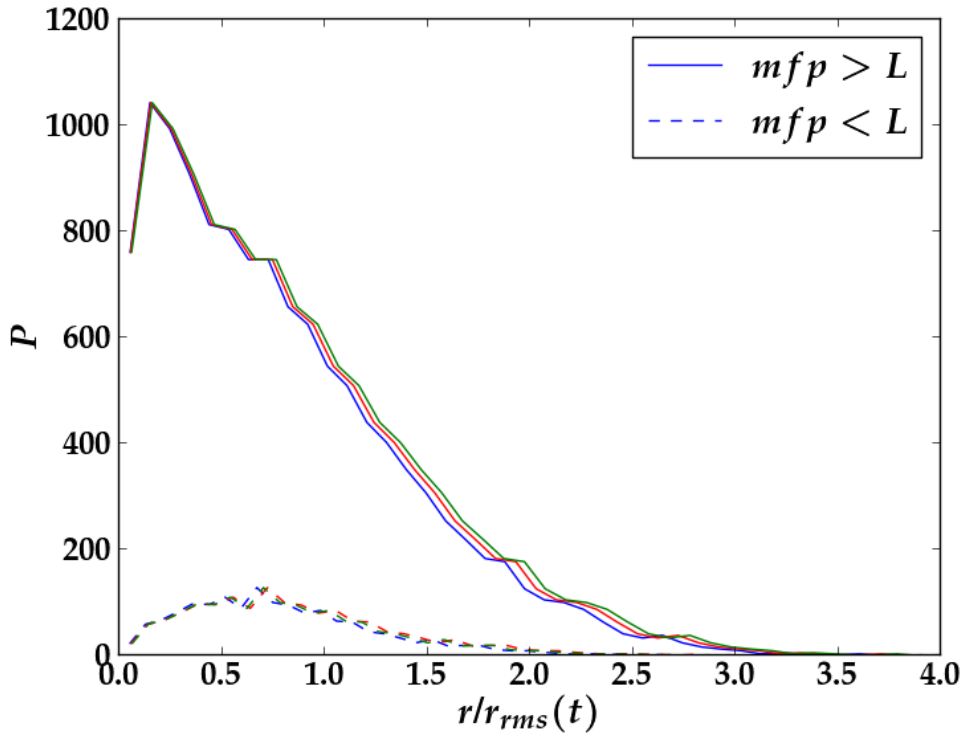

Figure 2.21: The probability distribution of test particles vs. the distance r at given time snapshots for $mfp > L$ and $mfp < L$. While for $mfp > L$ the pdf is exponential for $mfp < L$ the pdf is normal distribution.

For mean free path,$\lambda_{||}$ less than the injection length,L the distribution fits the normal Gaussian form when compared to the exponential form for mean free path,$\lambda_{||}$ greater than the injection length,L.

2.6 Conclusion

In this chapter, "test particle simulations have been carried out to study the diffusion of CRs in different MHD turbulence. The particles are considered with mean free path $\lambda_{\parallel}$ both larger and smaller than the injection scale L. The MHD turbulence data cubes range from sub-Alfvénic to super-Alfvénic regimes. The test particle simulations are also performed in the three MHD modes (Alfvén, slow and fast), decomposed from the MHD turbulence data cubes. The CRs propagating within and beyond the inertial range are investigated. The test particle results are examined in both the local and global reference frames. The main results from the current study are summarised below."

1. "The pitch angle scattering test of CRs for different MHD modes shows that: while the pitch angle scattering in Alfvén and slow modes show similar diffusion coefficients, the fast modes differ and are much more efficient in CR scattering. The pitch angle scattering in compressible modes is both due to gyroresonance and transit time damping (TTD). For fast modes, the transit time damping works at higher pitch angles only whereas gyroresonance whose contribution is much less than TTD works at lower initial pitch angle. For Alfvén modes, only gyroresonance occurs. The scattering frequency normalised by the gyration frequency is proportional to the Larmor radius."

2. "Cross field transport of particles is normal diffusion on large scales. The ratio between perpendicular and parallel diffusion coefficients is close to the M_A^4 dependence. The mean free path of particles could be calculated in the local frame of reference from the parallel spatial diffusion coefficients and is similar in value to that calculated from the pitch angle diffusion coefficients".

3. "Particles undergo superdiffusion on scales smaller than injection scale of turbulence. The super-diffusion rate $d_{\perp}^2/t^3$ has shown a strong dependence on the Alfvénic Mach number".

4. "Richardson super-diffusion is well recovered (1.5 for $\lambda_{\parallel} > L$) and reduces with the decrease of $\lambda_{\parallel}$. In particular, the super-diffusion index becomes 0.75 for $\lambda_{\parallel} \sim L$ and normal diffusion is recovered when $\lambda_{\parallel} \ll L$ in the *local* magnetic reference frame with Alfvén modes decomposed from simulated turbulence data. The actual observed superdiffusion index also varies depending on the modes composition and Alfvénic Mach number of local turbulence".

Bibliography

Alfvén, H. (Oct. 1942). **Existence of Electromagnetic-Hydrodynamic Waves**. 150:3805, 405–406. DOI: 10.1038/150405d0 (see page 3).

Armstrong, J. W., B. J. Rickett, and S. R. Spangler (Apr. 1995). **Electron Density Power Spectrum in the Local Interstellar Medium**. 443, 209. DOI: 10.1086/175515 (see pages 3, 5, 53).

Arthur, S. J., S. -N. X. Medina, and W. J. Henney (Dec. 2016). **Turbulence in the ionized gas of the Orion nebula**. 463:3, 2864–2884. DOI: 10.1093/mnras/stw2165. arXiv: 1608.07012 [astro-ph.GA] (see page 6).

Belcher, J. W. and Jr. Davis Leverett (Jan. 1971). **Large-amplitude Alfvén waves in the interplanetary medium, 2**. 76:16, 3534. DOI: 10.1029/JA076i016p03534 (see page 5).

Beresnyak, A., H. Yan, and A. Lazarian (Feb. 2011). **Numerical Study of Cosmic Ray Diffusion in Magnetohydrodynamic Turbulence**. *Astrophys. J.* 72860, 60. DOI: 10.1088/0004-637X/728/1/60. arXiv: 1002.2646 [astro-ph.GA] (see pages 36, 37, 49, 54).

Bieber, John W., Charles W. Smith, and William H. Matthaeus (Nov. 1988). **Cosmic-Ray Pitch-Angle Scattering in Isotropic Turbulence**. 334, 470. DOI: 10.1086/166851 (see page 35).

Bruno, Roberto and Vincenzo Carbone (May 2013). **The Solar Wind as a Turbulence Laboratory**. *Living Reviews in Solar Physics* 10:1, 2, 2. DOI: 10.12942/lrsp-2013-2 (see page 3).

Cesarsky, C. J. (Jan. 1980). **Cosmic-ray confinement in the galaxy**. 18, 289–319. DOI: 10.1146/annurev.aa.18.090180.001445 (see page 34).

Chandran, Benjamin D. G. (Nov. 2000). **Scattering of Energetic Particles by Anisotropic Magnetohydrodynamic Turbulence with a Goldreich-Sridhar Power Spectrum**. *Phys. Rev. Lett.* 85 (22), 4656–4659. DOI: 10.1103/PhysRevLett.85.4656. URL: https://link.aps.org/doi/10.1103/PhysRevLett.85.4656 (see pages 36, 38).

Chepurnov, A. and A. Lazarian (Feb. 2010). **Extending the Big Power Law in the Sky with Turbulence Spectra from Wisconsin Hα Mapper Data**. *Astrophys. J.* 710, 853–858. DOI: 10.1088/0004-637X/710/1/853. arXiv: 0905.4413 [astro-ph.GA] (see page 53).

Chepurnov, A., A. Lazarian, S. Stanimirović, Carl Heiles, and J. E. G. Peek (May 2010). **Velocity Spectrum for H I at High Latitudes**. 714:2, 1398–1406. DOI: 10.1088/0004-637X/714/2/1398. arXiv: astro-ph/0611462 [astro-ph] (see page 3).

Cho, J. and A. Lazarian (Oct. 2003). **Compressible magnetohydrodynamic turbulence: mode coupling, scaling relations, anisotropy, viscosity-damped regime and as-**

trophysical implications. *Mon. Not. R. Astron. Soc.* 345, 325–339. DOI: 10.1046/j.1365-8711.2003.06941.x. eprint: arXiv:astro-ph/0301062 (see pages 5, 6, 36, 47).

Cho, J., A. Lazarian, and E. T. Vishniac (Jan. 2002). **Simulations of Magnetohydrodynamic Turbulence in a Strongly Magnetized Medium**. *Astrophys. J.* 564, 291–301. DOI: 10.1086/324186. eprint: arXiv:astro-ph/0105235 (see pages 5, 36).

Cho, Jungyeon and A. Lazarian (June 2002). **Compressible Sub-Alfvénic MHD Turbulence in Low- β Plasmas**. *Phys. Rev. Lett.* 88:24, 245001, 245001. DOI: 10.1103/PhysRevLett.88.245001. arXiv: astro-ph/0205282 [astro-ph] (see pages 5, 7, 36, 46–48).

Cho, Jungyeon and Ethan T. Vishniac (Aug. 2000). **The Anisotropy of Magnetohydrodynamic Alfvénic Turbulence**. 539:1, 273–282. DOI: 10.1086/309213. arXiv: astro-ph/0003403 [astro-ph] (see pages 5, 36).

Dupree, T. H. (Sept. 1966). **A Perturbation Theory for Strong Plasma Turbulence**. *Physics of Fluids* 9:9, 1773–1782. DOI: 10.1063/1.1761932 (see page 35).

Earl, J. A. (Oct. 1974). **The diffusive idealization of charged-particle transport in random magnetic fields.** 193, 231–242. DOI: 10.1086/153152 (see page 53).

Eyink, Gregory, Ethan Vishniac, Cristian Lalescu, Hussein Aluie, Kalin Kanov, Kai Bürger, Randal Burns, Charles Meneveau, and Alexander Szalay (May 2013). **Flux-freezing breakdown in high-conductivity magnetohydrodynamic turbulence**. 497:7450, 466–469. DOI: 10.1038/nature12128 (see pages 64, 71, 76).

Federrath, Christoph (June 2018). **The turbulent formation of stars**. *Physics Today* 71:6, 38–42. DOI: 10.1063/PT.3.3947. arXiv: 1806.05312 [astro-ph.SR] (see page 3).

Felice, G. M. and R. M. Kulsrud (May 2001). **Cosmic-Ray Pitch-Angle Scattering through 90°**. 553:1, 198–210. DOI: 10.1086/320651 (see page 38).

Getmantsev, G. G. (Feb. 1963). **On the Isotropy of Primary Cosmic Rays**. 6, 477 (see page 40).

Giacalone, J. and J. R. Jokipii (July 1999). **The Transport of Cosmic Rays across a Turbulent Magnetic Field**. 520:1, 204–214. DOI: 10.1086/307452 (see page 35).

Goldreich, P. and S. Sridhar (Jan. 1995). **Toward a theory of interstellar turbulence. 2: Strong alfvenic turbulence**. *Astrophys. J.* 438, 763–775. DOI: 10.1086/175121 (see pages 4, 35, 64).

Goldstein, M. L. (Mar. 1976). **A nonlinear theory of cosmic-ray pitch-angle diffusion in homogeneous magnetostatic turbulence.** 204, 900–919. DOI: 10.1086/154239 (see pages 35, 38).

Hentschel, H. G. E. and I. Procaccia (Mar. 1984). **Relative diffusion in turbulent media: The fractal dimension of clouds**. 29:3, 1461–1470. DOI: 10.1103/PhysRevA.29.1461 (see page 71).

Higdon, J. C. (Oct. 1984). **Density fluctuations in the interstellar medium: Evidence for anisotropic magnetogasdynamic turbulence. I - Model and astrophysical sites.** 285, 109–123. DOI: 10.1086/162481 (see page 4).

Iroshnikov, P. S. (Jan. 1963). **Turbulence of a Conducting Fluid in a Strong Magnetic Field**. 40, 742 (see page 3).

Jokipii, J. R. (Nov. 1966). **Cosmic-Ray Propagation. I. Charged Particles in a Random Magnetic Field**. 146, 480. DOI: 10.1086/148912 (see pages 3, 35).

Jokipii, J. R. and E. N. Parker (Mar. 1969). **Stochastic Aspects of Magnetic Lines of Force with Application to Cosmic-Ray Propagation**. 155, 777. DOI: 10.1086/149909 (see page 41).

Jones, Frank C., Thomas J. Birmingham, and Thomas B. Kaiser (Mar. 1973). **Investigation of Resonance Integrals Occurring in Cosmic-Ray Diffusion Theory**. 180, L139. DOI: 10.1086/181170 (see pages 35, 38).

Kaiser, T. B., T. J. Birmingham, and F. C. Jones (Mar. 1978). **Computer simulation of the velocity diffusion of cosmic rays**. *Physics of Fluids* 21, 361–373. DOI: 10.1063/1.862234 (see page 35).

Kolmogorov, A. N. (July 1991). **The Local Structure of Turbulence in Incompressible Viscous Fluid for Very Large Reynolds Numbers**. *Proceedings of the Royal Society of London Series A* 434:1890, 9–13. DOI: 10.1098/rspa.1991.0075 (see page 2).

Kóta, J. and J. R. Jokipii (Mar. 2000). **Velocity Correlation and the Spatial Diffusion Coefficients of Cosmic Rays: Compound Diffusion**. 531:2, 1067–1070. DOI: 10.1086/308492 (see pages 35, 39, 40, 59).

Kowal, G., A. Lazarian, and A. Beresnyak (Mar. 2007). **Density Fluctuations in MHD Turbulence: Spectra, Intermittency, and Topology**. 658:1, 423–445. DOI: 10.1086/511515. arXiv: astro-ph/0608051 [astro-ph] (see page 6).

Kraichnan, Robert H. (July 1965). **Inertial-Range Spectrum of Hydromagnetic Turbulence**. *Physics of Fluids* 8:7, 1385–1387. DOI: 10.1063/1.1761412 (see page 3).

Krasnopolsky, Ruben, Zhi-Yun Li, Hsien Shang, and Bo Zhao (Sept. 2012). **Protostellar Accretion Flows Destabilized by Magnetic Flux Redistribution**. 757:1, 77, 77. DOI: 10.1088/0004-637X/757/1/77. arXiv: 1205.4083 [astro-ph.SR] (see page 3).

Kulsrud, Russell and William P. Pearce (May 1969). **The Effect of Wave-Particle Interactions on the Propagation of Cosmic Rays**. 156, 445. DOI: 10.1086/149981 (see page 37).

Lazarian, A. (July 2006). **Enhancement and Suppression of Heat Transfer by MHD Turbulence**. 645:1, L25–L28. DOI: 10.1086/505796. arXiv: astro-ph/0608045 [astro-ph] (see pages 40, 42).

Lazarian, A. and Ethan T. Vishniac (June 1999). **Reconnection in a Weakly Stochastic Field**. 517:2, 700–718. DOI: 10.1086/307233. arXiv: astro-ph/9811037 [astro-ph] (see page 40).

Lazarian, A. and H Yan (Mar. 2014). **Superdiffusion of Cosmic Rays: Implications for Cosmic Ray Acceleration**. 784:1, 38, 38. DOI: 10.1088/0004-637X/784/1/38. arXiv: 1308.3244 [astro-ph.HE] (see pages 3, 36–38, 40–43, 64, 71).

Le Roux, J. A. and G. M. Webb (Aug. 2007). **A BGK-Boltzmann Approach to Nonlinear Cosmic Ray Transport in 2D and Slab Turbulence**. In: *Turbulence and Nonlinear Processes in Astrophysical Plasmas*. Ed. by Dastgeer Shaikh and Gary P. Zank. Vol. 932.

American Institute of Physics Conference Series, 258–263. DOI: 10.1063/1.2778972 (see page 35).
Lerche, I. and R. Schlickeiser (Oct. 2001). **Cosmic ray transport in anisotropic magnetohydrodynamic turbulence. I. Fast magnetosonic waves**. 378, 279–294. DOI: 10.1051/0004-6361:20011080 (see page 36).
Longair, M. S. (1997). **High energy astrophysics. Volume 2: Stars, the galaxy and the interstellar medium**. Cambridge U Press, 1994 (see page 34).
Mac Low, Mordecai-Mark and Ralf S. Klessen (Jan. 2004). **Control of star formation by supersonic turbulence**. *Reviews of Modern Physics* 76:1, 125–194. DOI: 10.1103/RevModPhys.76.125. arXiv: astro-ph/0301093 [astro-ph] (see page 3).
Mace, R. L., William H. Matthaeus, and John W. Bieber (July 2000). **Numerical Investigation of Perpendicular Diffusion of Charged Test Particles in Weak Magnetostatic Slab Turbulence**. 538:1, 192–202. DOI: 10.1086/309093 (see page 40).
Maclennan, C. G., L. J. Lanzerotti, and S. E. Hawkins (Aug. 2001). **Populating the inner heliosphere (<5 AU) with heavy ions**. In: *International Cosmic Ray Conference*. Vol. 8. International Cosmic Ray Conference, 3265 (see page 40).
Maiti, Snehanshu, Kirit Makwana, Heshou Zhang, and Huirong Yan (Feb. 2022). **Cosmic-ray Transport in Magnetohydrodynamic Turbulence**. *The Astrophysical Journal* 926:1, 94. DOI: 10.3847/1538-4357/ac46c8. URL: https://doi.org/10.3847/1538-4357/ac46c8 (see page 49).
Makwana, K. D. and Huirong Yan (July 2020). **Properties of Magnetohydrodynamic Modes in Compressively Driven Plasma Turbulence**. *Physical Review X* 10:3, 031021, 031021. DOI: 10.1103/PhysRevX.10.031021. arXiv: 1907.01853 [physics.plasm-ph] (see page 6).
Maron, Jason and Peter Goldreich (June 2001). **Simulations of Incompressible Magnetohydrodynamic Turbulence**. 554:2, 1175–1196. DOI: 10.1086/321413. arXiv: astro-ph/0012491 [astro-ph] (see pages 5, 36).
Matthaeus, W. H., G. Qin, J. W. Bieber, and G. P. Zank (June 2003). **Nonlinear Collisionless Perpendicular Diffusion of Charged Particles**. 590:1, L53–L56. DOI: 10.1086/376613 (see pages 35, 39).
Matthaeus, William H., Melvyn L. Goldstein, and David C. Montgomery (Oct. 1983). **Turbulent Generation of Outward-Traveling Interplanetary Alfvénic Fluctuations**. *Phys. Rev. Lett.* 51 (16), 1484–1487. DOI: 10.1103/PhysRevLett.51.1484. URL: https://link.aps.org/doi/10.1103/PhysRevLett.51.1484 (see page 4).
Mignone, A. (Aug. 2007). **A simple and accurate Riemann solver for isothermal MHD**. *Journal of Computational Physics* 225:2, 1427–1441. DOI: 10.1016/j.jcp.2007.01.033. arXiv: astro-ph/0701798 [astro-ph] (see pages 8, 47).
Mignone, A., G. Bodo, S. Massaglia, T. Matsakos, O. Tesileanu, C. Zanni, and A. Ferrari (May 2007). **PLUTO: A Numerical Code for Computational Astrophysics**. *Astrophys. J. S.* 170:1, 228–242. DOI: 10.1086/513316. arXiv: astro-ph/0701854 [astro-ph] (see page 8).

Montgomery, D. and L. Turner (May 1981). **Anisotropic magnetohydrodynamic turbulence in a strong external magnetic field**. *Physics of Fluids* 24:5, 825–831. DOI: 10.1063/1.863455 (see page 4).

Müller, Wolf-Christian and Dieter Biskamp (Jan. 2000). **Scaling Properties of Three-Dimensional Magnetohydrodynamic Turbulence**. 84:3, 475–478. DOI: 10.1103/PhysRevLett.84.475. arXiv: physics/9906003 [physics.flu-dyn] (see page 36).

Narayan, Ramesh and Mikhail V. Medvedev (Dec. 2001). **Thermal Conduction in Clusters of Galaxies**. 562:2, L129–L132. DOI: 10.1086/338325. arXiv: astro-ph/0110567 [astro-ph] (see page 40).

Ogorzalek, A., I. Zhuravleva, S. W. Allen, C. Pinto, N. Werner, A. B. Mantz, R. E. A. Canning, A. C. Fabian, J. S. Kaastra, and J. de Plaa (Dec. 2017). **Improved measurements of turbulence in the hot gaseous atmospheres of nearby giant elliptical galaxies**. 472:2, 1659–1676. DOI: 10.1093/mnras/stx2030. arXiv: 1702.04364 [astro-ph.HE] (see page 6).

Owens, A. J. (July 1974). **The Effects of Nonlinear Terms in Cosmic-Ray Diffusion Theory**. 191, 235–244. DOI: 10.1086/152960 (see page 38).

Perri, Silvia and Gaetano Zimbardo (Mar. 2009). **Ion Superdiffusion at the Solar Wind Termination Shock**. 693:2, L118–L121. DOI: 10.1088/0004-637X/693/2/L118 (see page 40).

Press, William H., Brian P. Flannery, and Saul A. Teukolsky (1986). **Numerical recipes. The art of scientific computing** (see page 44).

Pryadko, Julia M. and Vahe Petrosian (Apr. 1999). **Stochastic Acceleration of Electrons by Plasma Waves. III. Waves Propagating Perpendicular to the Magnetic Field**. *The Astrophysical Journal* 515:2, 873–881. DOI: 10.1086/307056. URL: https://doi.org/10.1086/307056 (see page 35).

Qin, G. (Feb. 2007). **Nonlinear Parallel Diffusion of Charged Particles: Extension to the Nonlinear Guiding Center Theory**. 656:1, 217–221. DOI: 10.1086/510510 (see page 35).

Qin, G., W. H. Matthaeus, and J. W. Bieber (Oct. 2002). **Perpendicular Transport of Charged Particles in Composite Model Turbulence: Recovery of Diffusion**. 578:2, L117–L120. DOI: 10.1086/344687 (see pages 35, 40).

Richardson, Lewis F. (Apr. 1926). **Atmospheric Diffusion Shown on a Distance-Neighbour Graph**. *Proceedings of the Royal Society of London Series A* 110:756, 709–737. DOI: 10.1098/rspa.1926.0043 (see page 64).

Schlickeiser, R. (2002). **Cosmic Ray Astrophysics**. Ed. by R. Schlickeiser (see page 3).

Shalchi, A. (May 2005). **Second-order quasilinear theory of cosmic ray transport**. *Physics of Plasmas* 12:5, 052905–052905. DOI: 10.1063/1.1895805 (see page 35).

– (July 2006). **Extended nonlinear guiding center theory of perpendicular diffusion**. 453:3, L43–L46. DOI: 10.1051/0004-6361:20065465 (see page 35).

Shalchi, A., J. W. Bieber, W. H. Matthaeus, and G. Qin (Nov. 2004). **Nonlinear Parallel and Perpendicular Diffusion of Charged Cosmic Rays in Weak Turbulence**. 616:1, 617–629. DOI: 10.1086/424839 (see page 35).

Shebalin, J. V., W. H. Matthaeus, and D. Montgomery (June 1983). **Anisotropy in MHD turbulence due to a mean magnetic field**. *Journal of Plasma Physics* 29:3, 525–547. DOI: 10.1017/S0022377800000933 (see pages 4, 5).

Sokolov, Vlas, Ke Wang, Jaime E. Pineda, Paola Caselli, Jonathan D. Henshaw, Ashley T. Barnes, Jonathan C. Tan, Francesco Fontani, Izaskun Jiménez-Serra, and Qizhou Zhang (Mar. 2018). **Subsonic islands within a high-mass star-forming infrared dark cloud**. 611L3, L3. DOI: 10.1051/0004-6361/201832746. arXiv: 1802.07043 [astro-ph.GA] (see page 6).

Suzuki, T. K., A. Lazarian, and A. Beresnyak (June 2007). **Cascading of Fast-Mode Balanced and Imbalanced Turbulence**. 662:2, 1033–1042. DOI: 10.1086/513864. arXiv: astro-ph/0608307 [astro-ph] (see pages 7, 8, 29).

Swanson, D. G. (1989). **Plasma waves.** (see page 3).

Vestuto, Jason G., Eve C. Ostriker, and James M. Stone (June 2003). **Spectral Properties of Compressible Magnetohydrodynamic Turbulence from Numerical Simulations**. 590:2, 858–873. DOI: 10.1086/375021. arXiv: astro-ph/0303103 [astro-ph] (see page 6).

Voelk, H. J. (Aug. 1975). **Cosmic ray propagation in interplanetary space.** *Reviews of Geophysics and Space Physics* 13, 547–566. DOI: 10.1029/RG013i004p00547 (see pages 35, 38).

Völk, Heinrich J. (Dec. 1973). **Nonlinear Perturbation Theory for Cosmic Ray Propagation in Random Magnetic Fields**. 25:2, 471–490. DOI: 10.1007/BF00649186 (see pages 35, 38).

Webb, G. M., G. P. Zank, E. Kh. Kaghashvili, and J. A. le Roux (Nov. 2006). **Compound and Perpendicular Diffusion of Cosmic Rays and Random Walk of the Field Lines. I. Parallel Particle Transport Models**. 651:1, 211–236. DOI: 10.1086/507415 (see pages 35, 40).

Xu, Siyao and Huirong Yan (Dec. 2013). **Cosmic-Ray Parallel and Perpendicular Transport in Turbulent Magnetic Fields**. 779:2, 140, 140. DOI: 10.1088/0004-637X/779/2/140. arXiv: 1307.1346 [astro-ph.HE] (see pages 37, 41, 55, 56).

Yamaleev, Nail K. and Mark H. Carpenter (May 2009). **Third-order Energy Stable WENO scheme**. *Journal of Computational Physics* 228:8, 3025–3047. DOI: 10.1016/j.jcp.2009.01.011 (see page 8).

Yan, H and A. Lazarian (Dec. 2002). **Scattering of Cosmic Rays by Magnetohydrodynamic Interstellar Turbulence**. *Phys. Rev. Lett.* 89281102, 281102. DOI: 10.1103/PhysRevLett.89.281102. eprint: astro-ph/0205285 (see pages 5, 7, 36, 38).

– (Oct. 2004). **Cosmic-Ray Scattering and Streaming in Compressible Magnetohydrodynamic Turbulence**. *Astrophys. J.* 614, 757–769. DOI: 10.1086/423733. eprint: astro-ph/0408172 (see pages 3, 5, 7, 36, 38).

Yan, H, A. Lazarian, and V. Petrosian (Sept. 2008). **Particle Acceleration by Fast Modes in Solar Flares**. *Astrophys. J.* 684:2, 1461–1468. DOI: 10.1086/589962. arXiv: 0801.3786 [astro-ph] (see page 3).

Yan, H. and A. Lazarian (Feb. 2008). **Cosmic-Ray Propagation: Nonlinear Diffusion Parallel and Perpendicular to Mean Magnetic Field**. *Astrophys. J.* 673942-953, 942–953. DOI: 10.1086/524771. arXiv: 0710.2617 (see pages 3, 5, 36–38, 40, 42, 49, 52, 59, 61, 64, 71).

Yan, Huirong and A. Lazarian (Apr. 2011). **Cosmic Ray Transport Through Gyroresonance Instability in Compressible Turbulence**. 731:1, 35, 35. DOI: 10.1088/0004-637X/731/1/35. arXiv: 1009.5572 [astro-ph.HE] (see page 37).

Yang, Liping, Lei Zhang, Jiansen He, Chuanyi Tu, Shengtai Li, Xin Wang, and Linghua Wang (Oct. 2018). **Coexistence of Slow-mode and Alfvén-mode Waves and Structures in 3D Compressive MHD Turbulence**. 866:1, 41, 41. DOI: 10.3847/1538-4357/aadadf (see page 6).

List of Publications

Articles in Refereed Journals

[1] **Cosmic-ray Transport in Magnetohydrodynamic Turbulence**. *The Astrophysical Journal* 926:1, 94. DOI: 10.3847/1538-4357/ac46c8. URL: https://doi.org/10.3847/1538-4357/ac46c8. Joint work with Maiti, Snehanshu, Kirit Makwana, Heshou Zhang, and Huirong Yan.